

INTERIM REPORT

Accession No. _____
EGG-LOFT-5075

Contract Program or Project Title: LOFT PROGRAM

Subject of this Document: (Title) "Posttest Analysis of LOFT Loss-of-Coolant Experiment
L2-3"

Type of Document: Analysis

Author(s): J. C. Lin

Date of Document: March 1980

Responsible NRC Individual and NRC Office or Division G. D. McPherson

This document was prepared primarily for preliminary or internal use. It has not received full review and approval. Since there may be substantive changes, this document should not be considered final.

Prepared for
U.S. Nuclear Regulatory Commission
Washington, D.C. 20555

INTERIM REPORT

NRC Research and Technical
Assistance Report

8005300545

EGG-LOFT-5075
Project No. P 394

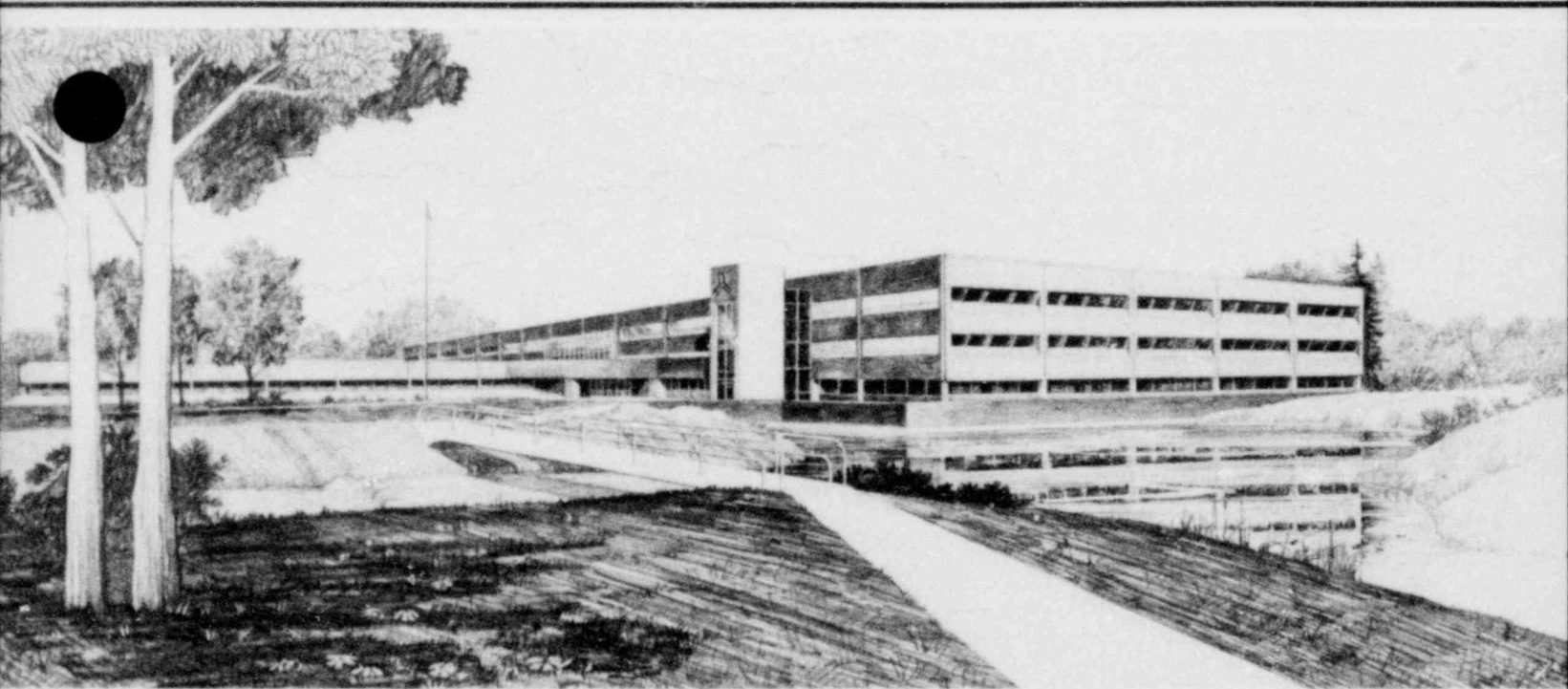
March 1980

POSTTEST ANALYSIS OF LOFT LOSS-OF-COOLANT
EXPERIMENT L2-3

Ju-Chuan Lin

U.S. Department of Energy

Idaho Operations Office • Idaho National Engineering Laboratory



This is an informal report intended for use as a preliminary or working document

Prepared for the
U.S. Nuclear Regulatory Commission
Under DOE Contract No. DE-AC07-76ID01570
FIN No. A604G

NRC Research and Technical
Assistance Report

POOR ORIGINAL



INTERIM REPORT

Accession No. _____

Report No. EGG-LOFT-5075

Contract Program or Project Title:

LOFT Experimental Program Division

Subject of this Document:

Posttest Analysis of LOFT Loss-of-Coolant Experiment L2-3

Type of Document:

Posttest Analysis Report

Author(s):

Ju-Chuan Lin

Date of Document:

March 1980

Responsible NRC Individual and NRC Office or Division:

G. D. McPherson, Acting Chief, LOFT Research Branch,
Division of Reactor Safety Research, USNRC

This document was prepared primarily for preliminary or internal use. It has not received full review and approval. Since there may be substantive changes, this document should not be considered final.

EG&G Idaho, Inc.
Idaho Falls, Idaho 83415

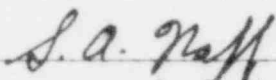
Prepared for the
U.S. Nuclear Regulatory Commission
Washington, D.C.
Under DOE Contract No. DE-AC07-76ID01570
NRC FIN No. A6048

INTERIM REPORT

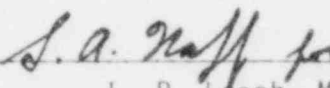
NRC Research and Technical
Assistance Report

POSTTEST ANALYSIS OF LOFT LOSS-OF-COOLANT
EXPERIMENT L2-3

Approved:



S. A. Naff, Manager
Program Planning and Test Evaluation Branch



L. P. Leach, Manager
LOFT Experimental Program Division

ABSTRACT

Results from Loss-of-Coolant Experiment L2-3, which is the second experiment in the Loss-of-Fluid Test (LOFT) Power Ascension Test Series L2, show that a core-wide rewet occurred early in the blowdown transient which was not calculated in the experiment prediction analyses. This posttest analysis determines the cause of the disparity between the predicted and measured data and provides calculated fuel rod temperature data that follow the trend of the measured data much closer than did the calculated data from the prediction analyses.

NRC FIN No. A6048 - LOFT Experimental Program

CONTENTS

ABSTRACT	iii
SUMMARY	xiii
1. INTRODUCTION	1
2. ANALYSIS OF SYSTEM HYDRAULICS RESPONSE	4
3. ANALYSIS OF FUEL ROD TEMPERATURE RESPONSE	10
3.1 Discussion of the Disparity Between Calculated and Measured Fuel Rod Surface Temperatures	10
3.1.1 Fuel Rod Stored Energy	12
3.1.2 Calculation of System Hydraulic Response	12
3.1.3 RELAP4/MOD6 Core Heat Transfer	12
3.2 Comparison of the Fuel Rod Cladding Surface Temperature Response Between Posttest Analysis and Experimental Data	17
4. CONCLUSIONS	28
5. REFERENCES	30
APPENDIX A--COMPARISON OF CALCULATED AND MEASURED SYSTEM HYDRAULICS DATA FOR LOCE L2-3	33
APPENDIX B--RELAP4/MOD6 HEAT TRANSFER SURFACE	79

FIGURES

1. Axonometric projection of LOFT system	2
2. LOFT core map showing position designations	3
3. Comparison of pressure in upper end box for prediction, posttest, and experimental data	5
4. Comparison of mass flow in broken loop cold leg for prediction, posttest, and experimental data	5
5. Comparison of mass flow in intact loop cold leg for prediction, posttest, and experimental data	6
6. Comparison of mass flow in broken loop hot leg for prediction, posttest, and experimental data	6

7.	Comparison of average coolant temperature in broken loop cold leg for prediction, posttest, and experimental data	8
8.	Comparison of posttest calculated and measured mass flow in broken and intact loop cold legs	8
9.	SPND output versus cladding temperatures	9
10.	Comparison of net mass flow in intact and broken loop cold legs for posttest and experimental data	11
11.	Initial fuel rod cladding temperature slope as a function of fuel rod stored energy	13
12.	RELAP4/MOD6 calculated minimum film boiling temperature compared with experimental data	15
13.	RELAP4/MOD6-Biasi calculated minimum film boiling temperature compared with experimental data	16
14.	Comparison of cladding temperature on fuel Rod 5F4 at 0.381 m above bottom of core for prediction, posttest, and experimental data	18
15.	Comparison of cladding temperature on fuel Rod 5J4 at 0.381 m above bottom of core for prediction, posttest, and experimental data	18
16.	Comparison of cladding temperature on fuel Rod 5F4 at 0.533 m above bottom of core for prediction, posttest, and experimental data	19
17.	Comparison of cladding temperature on fuel Rod 5J4 at 0.533 m above bottom of core for prediction, posttest, and experimental data	19
18.	Comparison of cladding temperature on fuel Rod 5F4 at 0.660 m above bottom of core for prediction, posttest, and experimental data	20
19.	Comparison of cladding temperature on fuel Rod 5J4 at 0.660 m above bottom of core for prediction, posttest, and experimental data	20
20.	Comparison of cladding temperature on fuel Rod 5D6 at 0.762 m above bottom of core for prediction, posttest, and experimental data	21
21.	Comparison of cladding temperature on fuel Rod 5F4 at 0.762 m above bottom of core for prediction, posttest, and experimental data	21

22.	Comparison of cladding temperature on fuel Rod 5J4 at 0.762 m above bottom of core for prediction, posttest, and experimental data	22
23.	Comparison of cladding temperature on fuel Rod 5L6 at 0.762 m above bottom of core for prediction, posttest, and experimental data	22
24.	Comparison of cladding temperature on fuel Rod 5D6 at 0.813 m above bottom of core for prediction, posttest, and experimental data	23
25.	Comparison of cladding temperature on fuel Rod 5L6 at 0.813 m above bottom of core for prediction, posttest, and experimental data	23
26.	Comparison of cladding temperature on fuel Rod 5D6 at 0.940 m above bottom of core for prediction, posttest, and experimental data	24
27.	Comparison of cladding temperature on fuel Rod 5L6 at 0.940 m above bottom of core for prediction, posttest, and experimental data	24
28.	Comparison of cladding temperature on fuel Rod 5D6 at 0.991 m above bottom of core for prediction, posttest, and experimental data	25
29.	Comparison of cladding temperature on fuel Rod 5L6 at 0.991 m above bottom of core for prediction, posttest, and experimental data	25
30.	Comparison of cladding temperature on fuel Rod 5I8 at 0.660 m above bottom of core for FRAP-T4 prediction and experimental data	26
A-1.	Comparison of measured average density in broken loop cold leg for prediction, posttest, and experimental data	36
A-2.	Comparison of average density in broken loop hot leg for prediction, posttest, and experimental data	36
A-3.	Comparison of average density in intact loop cold leg for prediction, posttest, and experimental data	37
A-4.	Comparison of average density in intact loop hot leg for prediction, posttest, and experimental data	37
A-5.	Comparison of differential pressure across 14- to 5-in. reducer for prediction, posttest, and experimental data	38

A-6.	Comparison of differential pressure across pump simulator for prediction, posttest, and experimental data	38
A-7.	Comparison of differential pressure across steam generator simulator for prediction, posttest, and experimental data	39
A-8.	Comparison of differential pressure across primary coolant pumps for prediction, posttest, and experimental data	39
A-9.	Comparison of differential pressure across intact loop steam generator for prediction, posttest, and experimental data	40
A-10.	Comparison of differential pressure across primary coolant Pump 1 for prediction, posttest, and experimental data	40
A-11.	Comparison of differential pressure across primary coolant Pump 2 for prediction, posttest, and experimental data	41
A-12.	Comparison of flow rate from accumulator for prediction, posttest, and experimental data	41
A-13.	Comparison of flow rate from low-pressure injection system pump for prediction, posttest, and experimental data	42
A-14.	Comparison of flow rate from high-pressure injection system pump for prediction, posttest, and experimental data	42
A-15.	Comparison of liquid level in accumulator for prediction, posttest, and experimental data	43
A-16.	Comparison of liquid level in steam generator secondary side for prediction, posttest, and experimental data	43
A-17.	Comparison of liquid level in pressurizer for prediction, posttest, and experimental data	44
A-18.	Comparison of mass flow in intact loop hot leg for prediction, posttest, and experimental data	44
A-19.	Comparison of total emergency core coolant flow rate for prediction, posttest, and experimental data	45
A-20.	Comparison of integral of emergency core coolant flow for prediction, posttest, and experimental data	45

A-21.	Comparison of momentum flux in broken loop cold leg for prediction, posttest, and experimental data	46
A-22.	Comparison of momentum flux in broken loop hot leg for prediction, posttest, and experimental data	46
A-23.	Comparison of momentum flux in intact loop cold leg for prediction, posttest, and experimental data	47
A-24.	Comparison of momentum flux in intact loop hot leg for prediction, posttest, and experimental data	47
A-25.	Comparison of momentum flux at instrument Stalk 1 for prediction, posttest, and experimental data	48
A-26.	Comparison of momentum flux in upper end box for prediction, posttest, and experimental data	48
A-27.	Comparison of momentum flux in upper end box for prediction, posttest, and experimental data	49
A-28.	Comparison of momentum flux at instrument Stalk 2 for prediction, posttest, and experimental data	49
A-29.	Comparison of pressure in broken loop cold leg for prediction, posttest, and experimental data	50
A-30.	Comparison of pressure in broken loop hot leg for prediction, posttest, and experimental data	50
A-31.	Comparison of pressure in broken loop hot leg pump simulator outlet for prediction, posttest, and experimental data	51
A-32.	Comparison of pressure in steam generator simulator outlet for prediction, posttest, and experimental data	51
A-33.	Comparison of pressure in broken loop cold leg spool piece midpoint for prediction, posttest, and experimental data	52
A-34.	Comparison of pressure in intact loop cold leg for prediction, posttest, and experimental data	52
A-35.	Comparison of pressure in intact loop hot leg for prediction, posttest, and experimental data	53
A-36.	Comparison of pressure in intact loop pressurizer for prediction, posttest, and experimental data	53
A-37.	Comparison of pressure at instrument Stalk 1 at 0.631 m above reactor vessel bottom for prediction, posttest, and experimental data	54

A-38.	Comparison of pressure at instrument Stalk 1 at 5.319 m above reactor vessel bottom for prediction, posttest, and experimental data	54
A-39.	Comparison of pressure at instrument Stalk 2 at 0.631 m above reactor vessel bottom for prediction, posttest, and experimental data	55
A-40.	Comparison of pressure in blowdown suppression tank for prediction, posttest, and experimental data	55
A-41.	Comparison of pressure in steam generator secondary side for prediction, posttest, and experimental data	56
A-42.	Comparison of pressure in accumulator for prediction, posttest, and experimental data	56
A-43.	Comparison of pressure at emergency core coolant cold leg injection point for prediction, posttest, and experimental data	57
A-44.	Comparison of Pump 1 speed for prediction, posttest, and experimental data	57
A-45.	Comparison of average fluid velocity in broken loop cold leg for prediction, posttest, and experimental data	58
A-46.	Comparison of average fluid velocity in broken loop hot leg for prediction, posttest, and experimental data	58
A-47.	Comparison of average fluid velocity in intact loop cold leg for prediction, posttest, and experimental data	59
A-48.	Comparison of average fluid velocity in intact loop hot leg for prediction, posttest, and experimental data	59
A-49.	Comparison of average coolant temperature in broken loop hot leg for prediction, posttest, and experimental data	60
A-50.	Comparison of average coolant temperature in intact loop cold leg for prediction, posttest, and experimental data	60
A-51.	Comparison of average coolant temperature in intact loop hot leg for prediction, posttest, and experimental data	61
A-52.	Comparison of coolant temperature on instrument Stalk 1 at 4.808 m above reactor vessel bottom for prediction, posttest, and experimental data	61
A-53.	Comparison of coolant temperature on instrument Stalk 1 at 4.199 m above reactor vessel bottom for prediction, posttest, and experimental data	62

A-54.	Comparison of coolant temperature on instrument Stalk 1 at 3.589 m above reactor vessel bottom for prediction, posttest, and experimental data	62
A-55.	Comparison of coolant temperature on instrument Stalk 1 at 2.979 m above reactor vessel bottom for prediction, posttest, and experimental data	63
A-56.	Comparison of coolant temperature on instrument Stalk 1 at 2.370 m above reactor vessel bottom for prediction, posttest, and experimental data	63
A-57.	Comparison of coolant temperature on instrument Stalk 1 at 1.760 m above reactor vessel bottom for prediction, posttest, and experimental data	64
A-58.	Comparison of coolant temperature on instrument Stalk 1 at 0.744 m above reactor vessel bottom for prediction, posttest, and experimental data	64
A-59.	Comparison of coolant temperature on instrument Stalk 1 at 0.643 m above reactor vessel bottom for prediction, posttest, and experimental data	65
A-60.	Comparison of coolant temperature on instrument Stalk 1 at 0.439 m above reactor vessel bottom for prediction, posttest, and experimental data	65
A-61.	Comparison of coolant temperature on instrument Stalk 1 at 0.338 m above reactor vessel bottom for prediction, posttest, and experimental data	66
A-62.	Comparison of coolant temperature on instrument Stalk 1 at 0.236 m above reactor vessel bottom for prediction, posttest, and experimental data	66
A-63.	Comparison of coolant temperature on instrument Stalk 1 at 1.166 m above reactor vessel bottom for prediction, posttest, and experimental data	67
A-64.	Comparison of coolant temperature on instrument Stalk 2 at 4.808 m above reactor vessel bottom for prediction, posttest, and experimental data	67
A-65.	Comparison of coolant temperature on instrument Stalk 2 at 4.199 m above reactor vessel bottom for prediction, posttest, and experimental data	68
A-66.	Comparison of coolant temperature on instrument Stalk 2 at 3.589 m above reactor vessel bottom for prediction, posttest, and experimental data	68

A-67.	Comparison of coolant temperature on instrument Stalk 2 at 2.370 m above reactor vessel bottom for prediction, posttest, and experimental data	69
A-68.	Comparison of coolant temperature on instrument Stalk 2 at 0.846 m above reactor vessel bottom for prediction, posttest, and experimental data	69
A-69.	Comparison of coolant temperature on instrument Stalk 2 at 0.643 m above reactor vessel bottom for prediction, posttest, and experimental data	70
A-70.	Comparison of coolant temperature on instrument Stalk 2 at 0.541 m above reactor vessel bottom for prediction, posttest, and experimental data	70
A-71.	Comparison of coolant temperature on instrument Stalk 2 at 0.236 m above reactor vessel bottom for prediction, posttest, and experimental data	71
A-72.	Comparison of coolant temperature on instrument Stalk 2 at 1.166 m above reactor vessel bottom for prediction, posttest, and experimental data	71
A-73.	Comparison of coolant temperature in fuel Module 1 lower end box for prediction, posttest, and experimental data	72
A-74.	Comparison of coolant temperature in fuel Module 2 lower end box for prediction, posttest, and experimental data	72
A-75.	Comparison of coolant temperature in fuel Module 3 lower end box for prediction, posttest, and experimental data	73
A-76.	Comparison of coolant temperature in fuel Module 1 upper end box for prediction, posttest, and experimental data	73
A-77.	Comparison of coolant temperature in fuel Module 1 upper end box at drag disc-turbine transducer for prediction, posttest, and experimental data	74
A-78.	Comparison of coolant temperature in fuel Module 2 upper end box for prediction, posttest, and experimental data	74
A-79.	Comparison of coolant temperature in fuel Module 3 upper end box for prediction, posttest, and experimental data	75

A-80.	Comparison of coolant temperature in fuel Module 3 upper end box at drag disc-turbine transducer for prediction, posttest, and experimental data	75
A-81.	Comparison of coolant temperature in fuel Module 4 upper end box for prediction, posttest, and experimental data	76
A-82.	Comparison of coolant temperature in fuel Module 5 upper end box for prediction, posttest, and experimental data	76
A-83.	Comparison of coolant temperature in fuel Module 5 upper end box at drag disc-turbine transducer for prediction, posttest, and experimental data	77
A-84.	Comparison of coolant temperature in fuel Module 6 upper end box for prediction, posttest, and experimental data	77
B-1.	RELAP4/MOD6 boiling curve	82
B-2.	RELAP4/MOD6 blowdown heat transfer surface	83
B-3.	Effects of the Biasi critical heat flux correlation on the RELAP4/MOD6 boiling curve	84
B-4.	TRAC-P1A boiling curve	86
B-5.	Effects of the Iloeje minimum film boiling correlation on the TRAC-P1A boiling curve	87

TABLE

1.	Comparison of Fuel Rod Models Used in RELAP4/MOD6 and FRAP-T5....	27
----	---	----

SUMMARY

A posttest analysis of Loss-of-Coolant Experiment (LOCE) L2-3, which was conducted in the Loss-of-Fluid Test (LOFT) facility, was performed to gain an understanding of the cause of the disparity between predicted and measured fuel rod cladding temperature responses in the LOFT core. LOCE L2-3 was performed as part of the LOFT Experimental Program conducted by EG&G Idaho, Inc., for the U.S. Nuclear Regulatory Commission. LOCE L2-3 is the second experiment in the LOFT Power Ascension Test Series L2 (first series of LOFT nuclear experiments), which was designed to investigate the response of the LOFT nuclear core to the blowdown, refill, and reflood transients during LOCEs conducted at gradually increasing power levels. LOCE L2-3 was conducted at a maximum linear heat generation rate of 39.37 kW/m, corresponding to 100% power for a typical large pressurized water reactor.

Results from LOCE L2-3 show that a core-wide rewet occurred early in the transient (during blowdown starting at about 8 s after rupture) which was not calculated in the pretest prediction analysis. This early core-wide rewet resulted in the peak fuel rod cladding temperatures being lower (by a mean value of 166 K for 24 thermocouples) than had been calculated. This posttest analysis was concerned with determining why the early core-wide rewet was not predicted by the RELAP4/MOD6 pretest analysis.

Three factors were postulated to have caused the disparity between predicted and measured fuel rod cladding temperatures for LOCE L2-3: (a) the initial fuel rod stored energy, (b) the heat transfer surface, and (c) the calculation of system hydraulic response. These factors were examined and are discussed in this report. It was determined that the heat transfer surface was the major factor causing the disparity.

POSTTEST ANALYSIS OF LOFT LOSS-OF-COOLANT EXPERIMENT L2-3

1. INTRODUCTION

Loss-of-Coolant Experiment (LOCE) L2-3 was the second experiment performed in the Loss-of-Fluid Test (LOFT) Power Ascension Test Series L2, which is the first series of experiments to be performed in the LOFT facility with the nuclear core producing power. LOCE L2-3 simulated a postulated loss-of-coolant accident (LOCA) resulting from a 200% double-ended offset shear break in the cold leg-of the primary coolant system of a large pressurized water reactor (PWR). At the time of experiment initiation, the LOFT reactor was operating at a 39.37-kW/m maximum linear heat generation rate (corresponding to 100% power in a typical large PWR).

Prior to conducting LOCE L2-3, pretest prediction analyses^{1,2} were performed using the RELAP4/MOD6³ and FRAP-T4⁴ computer codes. In general, the system hydraulics predicted in the pretest analyses are in good agreement with the experimental data. However, LOCE L2-3 data showed that a core-wide rewet occurred early in the transient (about 8 s after rupture). This core-wide rewet was not predicted in the pretest prediction analyses. A posttest analysis of LOCE L2-3 was subsequently performed. The main objective of the posttest analysis was to understand the cause of the disparity between the experiment predictions and the measured fuel rod cladding temperature response in the LOFT core. Based on this analysis, recommendations were made to change the RELAP4/MOD6 computer code to allow a more physically realistic prediction of the data.

A description of the LOFT system and experimental program is provided in Reference 5. The major components are illustrated in Figure 1. Figure 2 shows the fuel rod position designations within the LOFT reactor core.

In this report, Section 2 presents comparisons of system hydraulics data from the posttest analysis, pretest predictions, and LOCE L2-3. Section 3 discusses the postulated factors to cause the disparity between the predicted and the measured fuel rod cladding temperature for LOCE L2-3 and proposes the resolution for possible causes of the disparity. Section 3

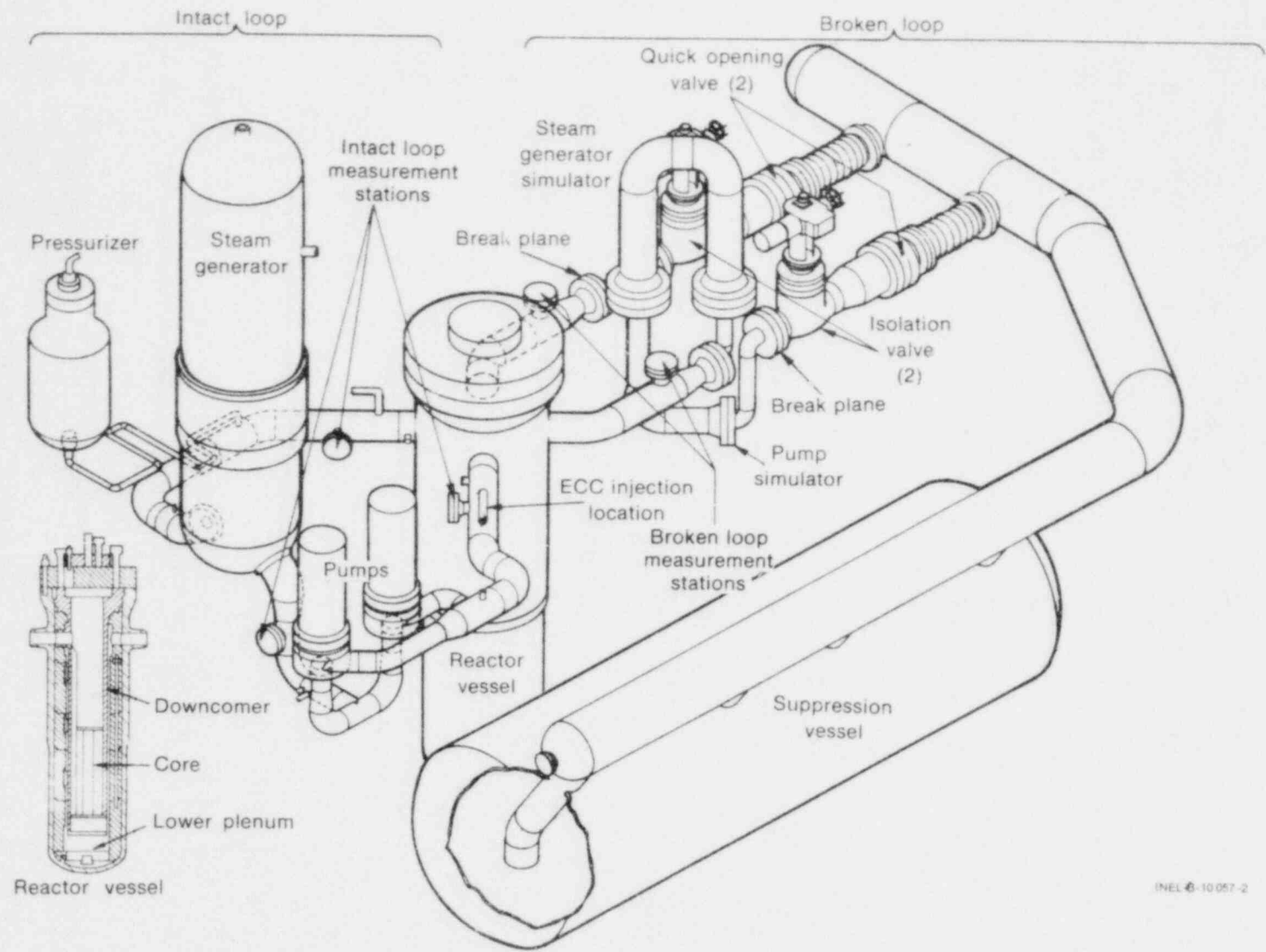


Figure 1. Axonometric projection of LOFT system.

INEL-6-10057-2

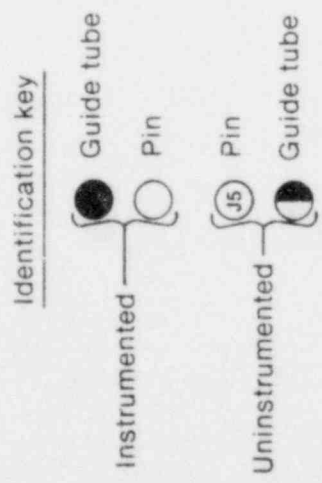
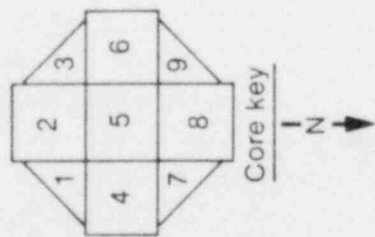
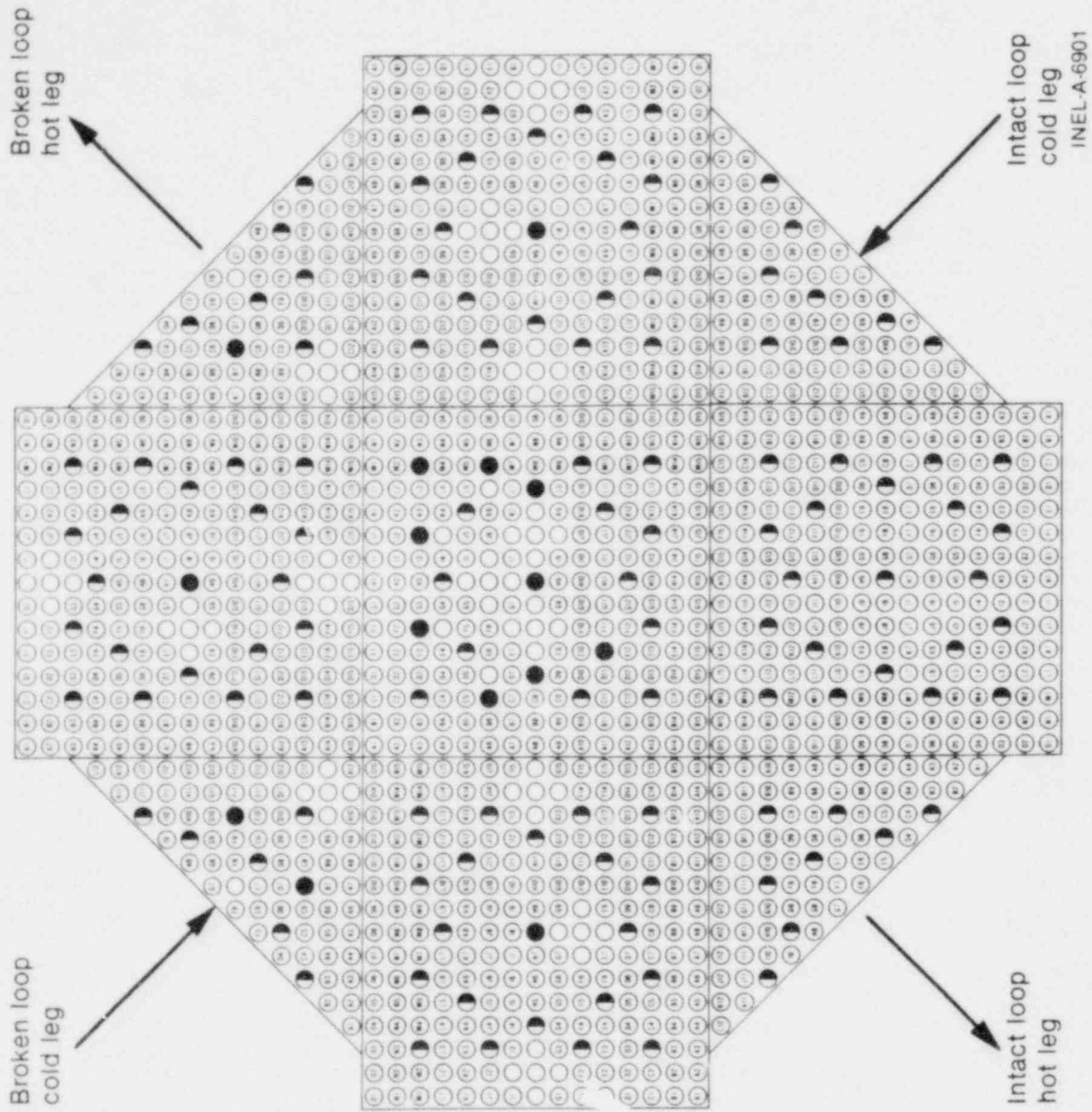


Figure 2. LOFT core map showing position designations.

also compares fuel rod cladding temperature data from the posttest analysis, pretest predictions, and LOCE L2-3. Section 4 presents the conclusions and suggested future work.

2. ANALYSIS OF SYSTEM HYDRAULICS RESPONSE

This posttest analysis used the same RELAP4/MOD6 model of the LOFT system, break flow multipliers (0.84), and transition quality (0.0025) as the experiment predictions (EP)^{1,2}. The RELAP4/MOD6 code was updated^a to use Biasi's⁶ critical heat flux (CHF) correlation. The test initial conditions given in the Experiment Data Report for LOCE L2-3⁷ were used in the posttest calculation.

Figure 3 shows the comparison of calculated and measured upper plenum pressure. The predictions are in very good agreement with the experimental data. Figures 4 and 5 show the comparison of measured and calculated mass flow in the broken loop cold leg and in the intact loop cold leg, respectively. Both the posttest analysis and EP calculated mass flows are in very good agreement with the experimental data. Figure 6 presents the comparison of calculated and measured mass flow in the broken loop hot leg. The posttest analysis and EP predicted mass flows are in excellent agreement with the experimental data. Figure 7 indicates the comparison of calculated and measured fluid temperature in the broken loop cold leg. The predictions and the experimental data are in very good agreement. From the above comparisons, it is concluded that the posttest analysis and EP calculate the most important system hydraulic parameters very well. More comparisons of the calculated and measured system hydraulics are given in Appendix A. In general, the predictions agree with the experimental data within the range allowed by the instrument uncertainty.

a. RELAP4/MOD6, Update 4, Idaho National Engineering Laboratory Configuration Control Numbers H009884B and H009584B were used for system hydraulics and hot rod calculations, respectively.

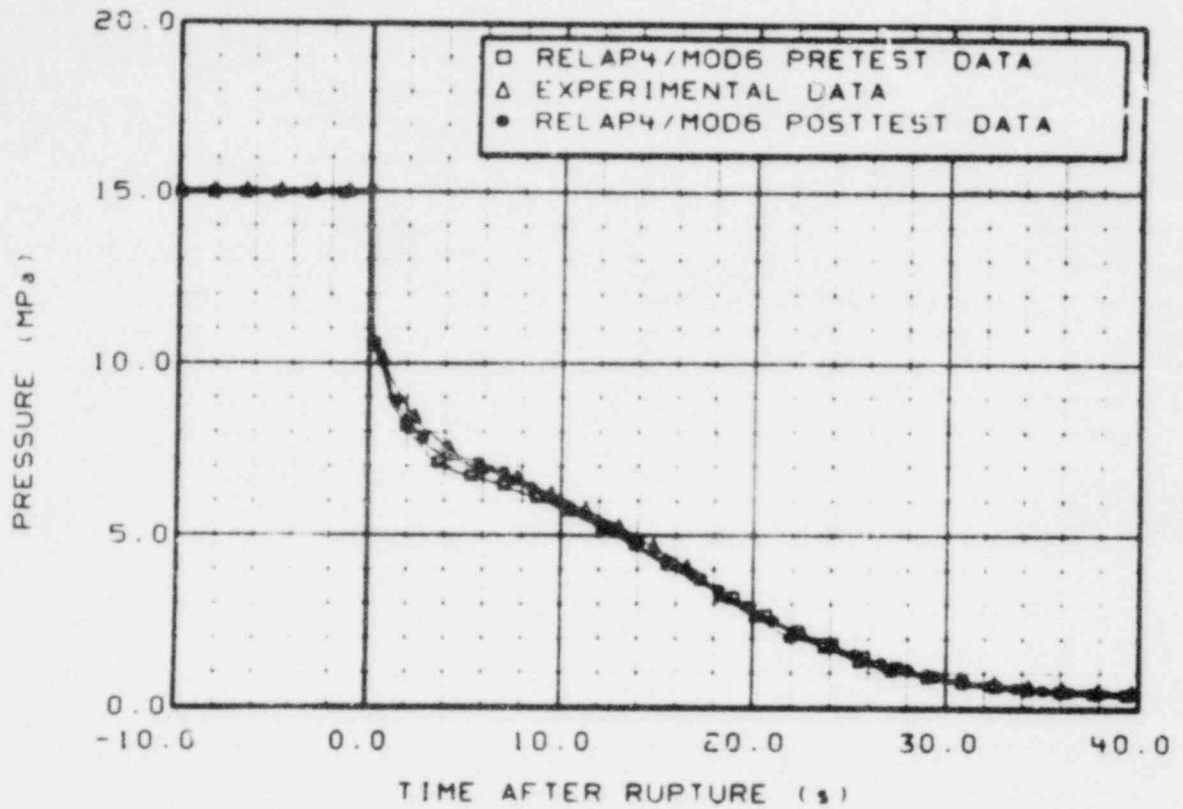


Figure 3. Comparison of pressure in upper end box for prediction, posttest, and experimental data.

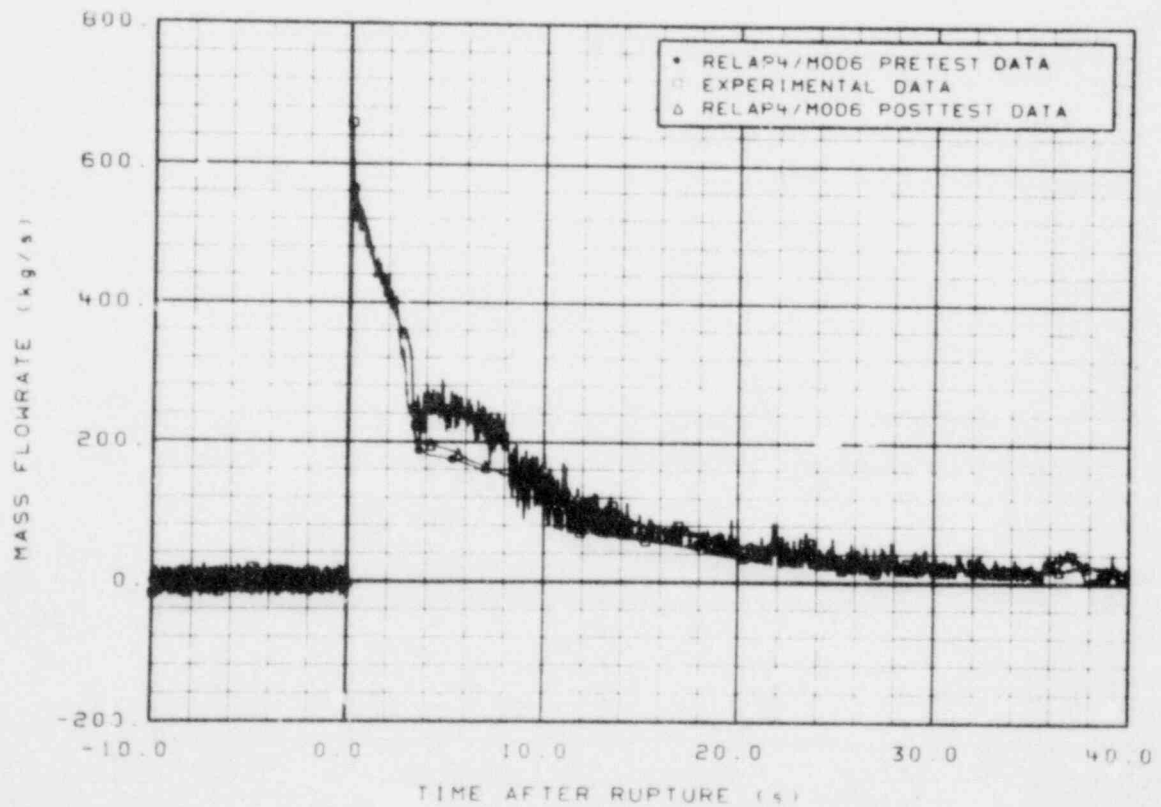


Figure 4. Comparison of mass flow in broken loop cold leg for prediction, posttest, and experimental data.

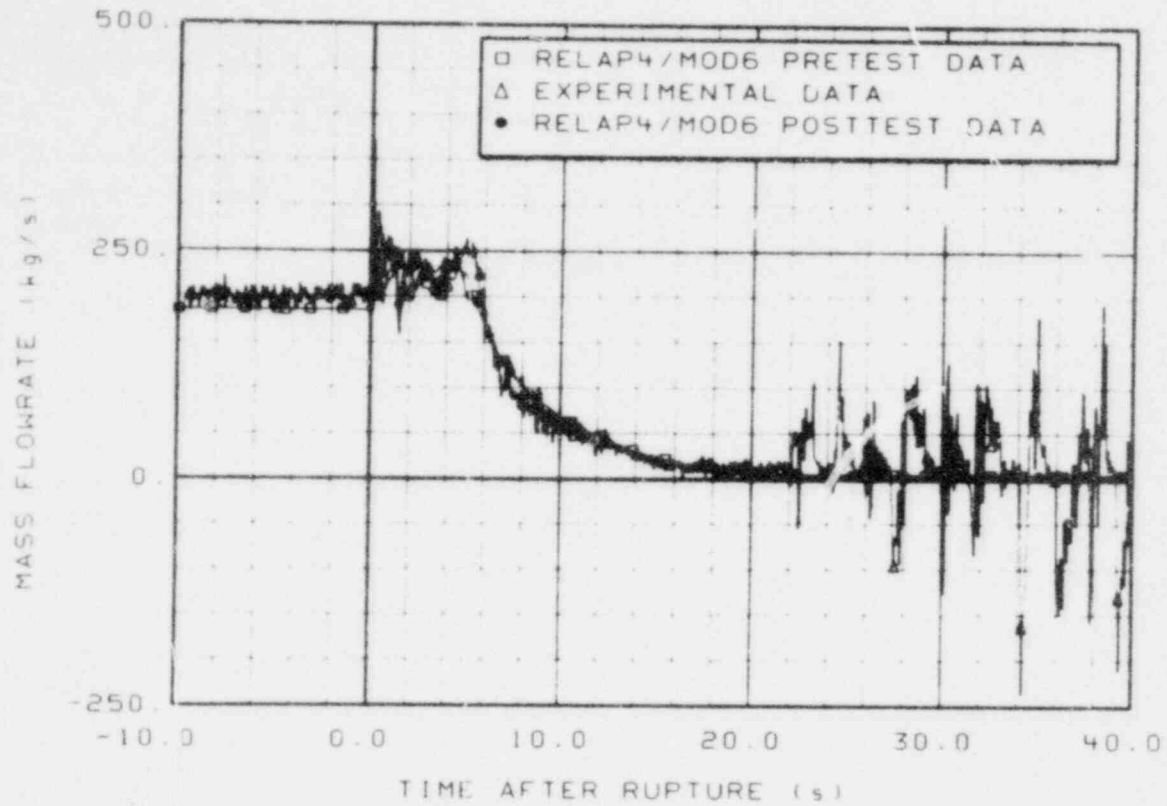


Figure 5. Comparison of mass flow in intact loop cold leg for prediction, posttest, and experimental data.

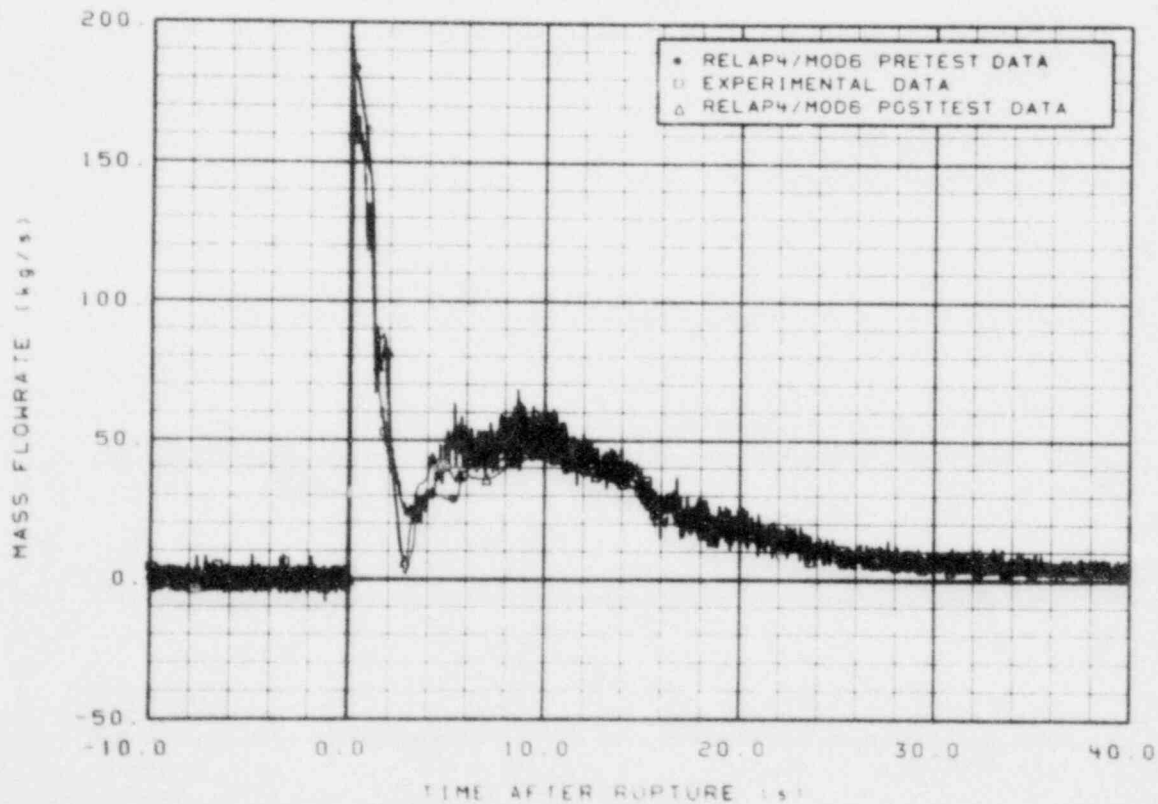


Figure 6. Comparison of mass flow in broken loop hot leg for prediction, posttest, and experimental data.

Figures 3 through 7 also indicate that the results from the posttest analysis are in slightly better agreement with the experimental data than are the EP results. A sensitivity study which included a RELAP4/MODE system run using the measured initial test conditions⁷ without the Biasi CHF correlation was performed to investigate the cause of the improved calculation of LOCE L2-3 results by the posttest analysis. The results of this sensitivity study run and the posttest analysis using the Biasi CHF correlation are almost identical. It is concluded that use of measured initial test conditions improves calculation of the system hydraulics slightly in the posttest analysis. However, to control the test initial conditions, as specified in the experiment operating specification, is very important for the EP analysis.

Figure 8 presents a comparison between the posttest analysis and experimental data for mass flow in the broken and intact loop cold legs. Immediately after experiment initiation, the core inlet flow reversed to supply the mass flow demand of the broken loop cold leg. Hot fluid from the core passed downward through the lower plenum and up the downcomer into the broken loop cold leg. The hot fluid arrival in the broken loop cold leg at 2.5 s dramatically reduced the mass flow. This is due to the transition from the high density subcooled break flow to the low density saturation break flow. The intact loop cold leg flow, driven by the operating pumps, exceeded the broken loop flow for 2 s causing an increase in positive core flow, which had rereversed after saturation in the lower plenum, and provided subcooled fluid to the downcomer. The subcooled fluid mixed with saturated fluid in the downcomer and lower plenum and induced a two-phase density wave which traversed the core from bottom to top. The two-phase density wave was detected by the self-powered neutron detectors (SPND), thermocouples, and liquid level detectors. Figure 9 shows the SPND and cladding thermocouple outputs. The decrease in negative SPND output was caused by the combined effects of local gamma flux attenuation and an increase in the delayed neutron flux. The flux changes were caused by the two-phase density wave. Similar trends of the experimental data were predicted by the posttest analysis. The predicted mass flow rate was inside the experimental data uncertainty band ($\pm 7\%$) as shown in Figure 8. However, the transition from subcooled break flow to saturation break flow for

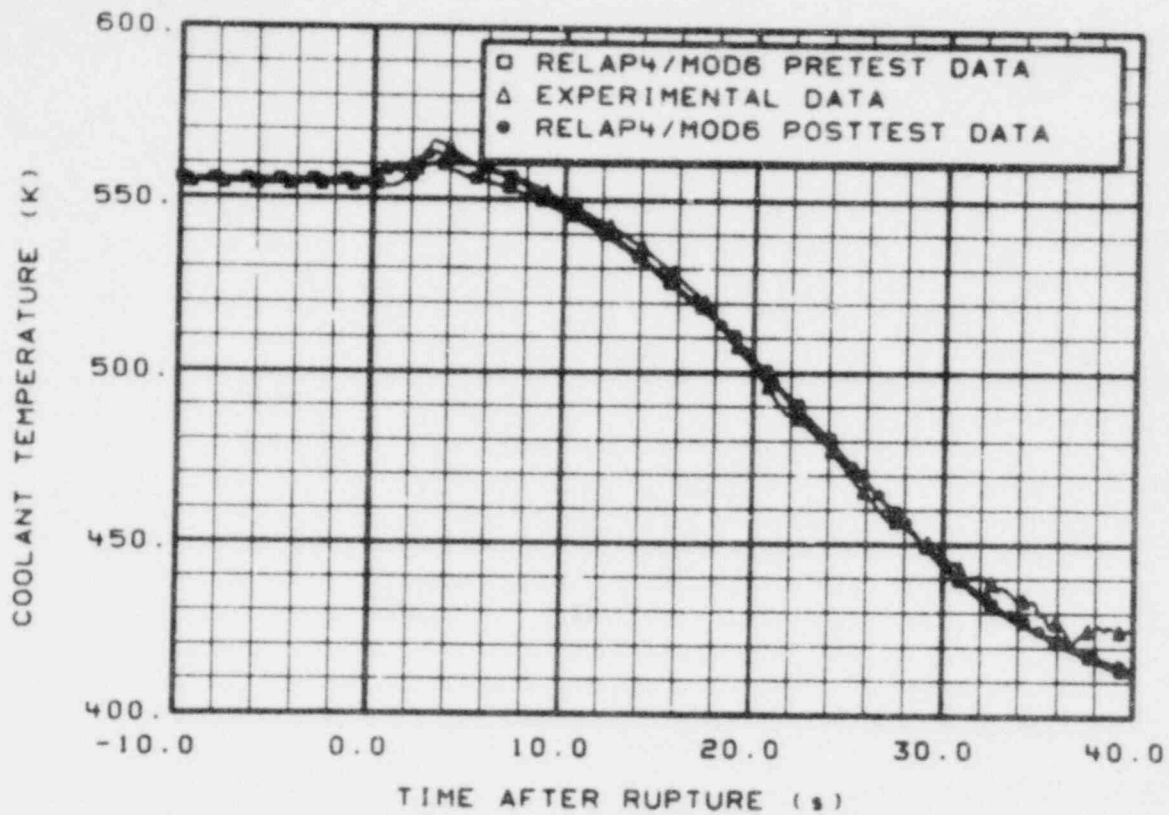


Figure 7. Comparison of average coolant temperature in broken loop cold leg for prediction, posttest, and experimental data.

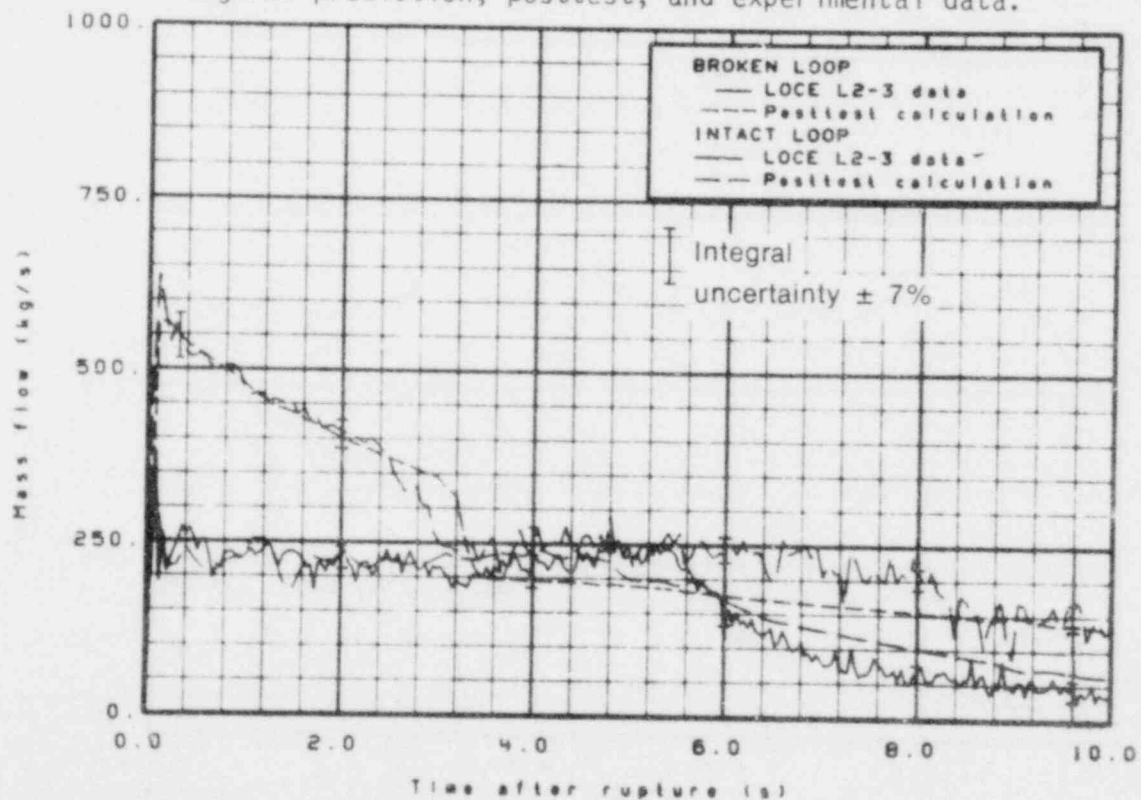


Figure 8. Comparison of posttest calculated and measured mass flow in broken and intact loop cold legs.

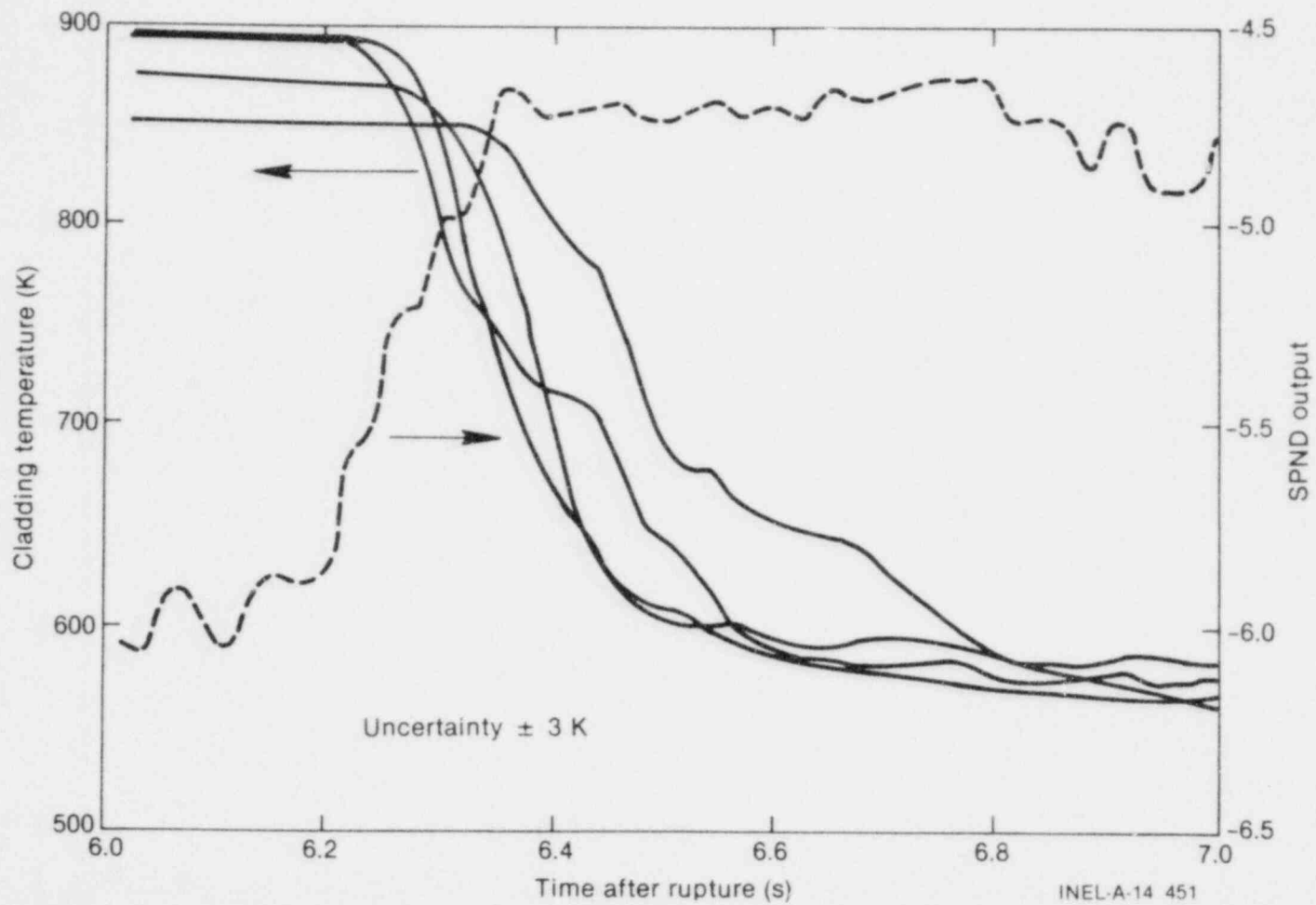


Figure 9. SPND output versus cladding temperatures.

the posttest analysis was about 0.5 s later than was shown by the experimental data. This is due to the coarse nodalization in the system model from the downcomer to the break plane. The coarse nodalization results in a lower average temperature at the break plane and a delay in transition from subcooled to saturated flow. Figure 10 presents the comparison of net mass flow in the broken and intact loop cold legs for the posttest analysis and the experimental data. The posttest analysis is in good agreement with the experimental data except for the intervals of 2.5 to 3.5 s and 4.8 to 5.8 s. From 2.5 to 3.5 s, the discrepancy is due to the nodalization. The reason for the discrepancy in the 4.8-to-5.8-s interval is not known.

In general, the system hydraulics data calculated in the posttest analysis agree with the experimental data very well. This is a very important factor to understanding the fuel rod temperature response discussed in Section 3.

3. ANALYSIS OF FUEL ROD TEMPERATURE RESPONSE

Fuel rod cladding temperatures from LOCE L2-3 showed that a core-wide rewet occurred at about 8 s after rupture which was not predicted by the EP analyses. This section discusses the factors postulated to have caused the disparity between predicted and measured fuel rod cladding temperatures and the proposed resolutions for the possible causes. This section also compares fuel rod cladding temperature data from the posttest analysis, EP analyses, and LOCE L2-3.

3.1 Discussion of the Disparity Between Calculated and Measured Fuel Rod Surface Temperatures

Three factors were postulated to have caused the early core-wide rewet observed during LOCE L2-3 to not be predicted by the EP analyses: (a) the initial fuel rod stored energy, (b) the calculation of system hydraulic response, and (c) the RELAP4/MOD6 core heat transfer. These postulates are examined in the following sections.

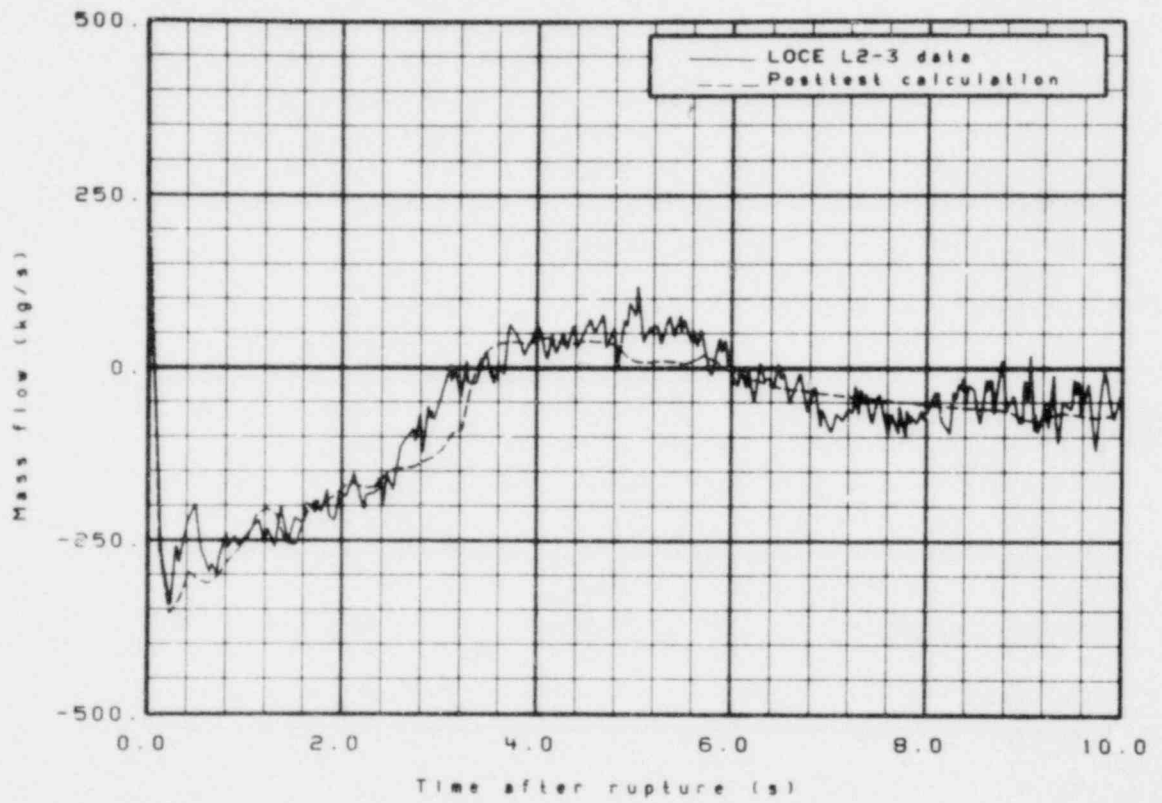


Figure 10. Comparison of net mass flow in intact and broken loop cold legs for posttest and experimental data.

3.1.1 Fuel Rod Stored Energy

The initial heatup rates have been shown to be a strong function of stored energy and to be a weak function of initial heat transfer and gap conductance⁸. Sensitivity studies on the effect of stored energy, gap conductance, and heat transfer boundary conditions on the fuel rod temperature response have also been given in Reference 8. It was concluded in Reference 8 that stored energy and initial temperature rise can be closely correlated. The same correlation method which tabulated the initial cladding temperature slope and fuel rod stored energy for LOCEs L2-2, L2-3, and L2-4 was used to predict the initial fuel rod stored energy, as shown in Figure 11. The correlation is in good agreement with the LOCE L2-3 data and is within the $\pm 2\sigma$ uncertainty band of the correlation parameters. Therefore, the discrepancy between the cladding temperatures predicted in the EP and the experimental data is not caused by the initial fuel rod stored energy.

3.1.2 Calculation of System Hydraulic Response

As discussed in Section 2, it is shown that the system hydraulic conditions predicted in the EP analyses are in good agreement with the experimental data and that the difference between the EP and the posttest analysis calculations for system hydraulics is very small. In the posttest analysis, a core-wide rewet was predicted. The only difference between the EP and the posttest analysis is that in the posttest analysis the measured initial test conditions⁷ and the Biasi CHF correlation were used. It is concluded that the disparity between the fuel rod cladding temperatures predicted in the EP and those shown in the experimental data is not due to the calculation of system hydraulics.

3.1.3 RELAP4/MOD6 Core Heat Transfer

From the RELAP4/MOD6 heat transfer study, it is shown that the use of the boiling curve in RELAP4/MOD6 has two variables which can be altered and may cause early fuel rod rewet to be calculated: The first variable is the

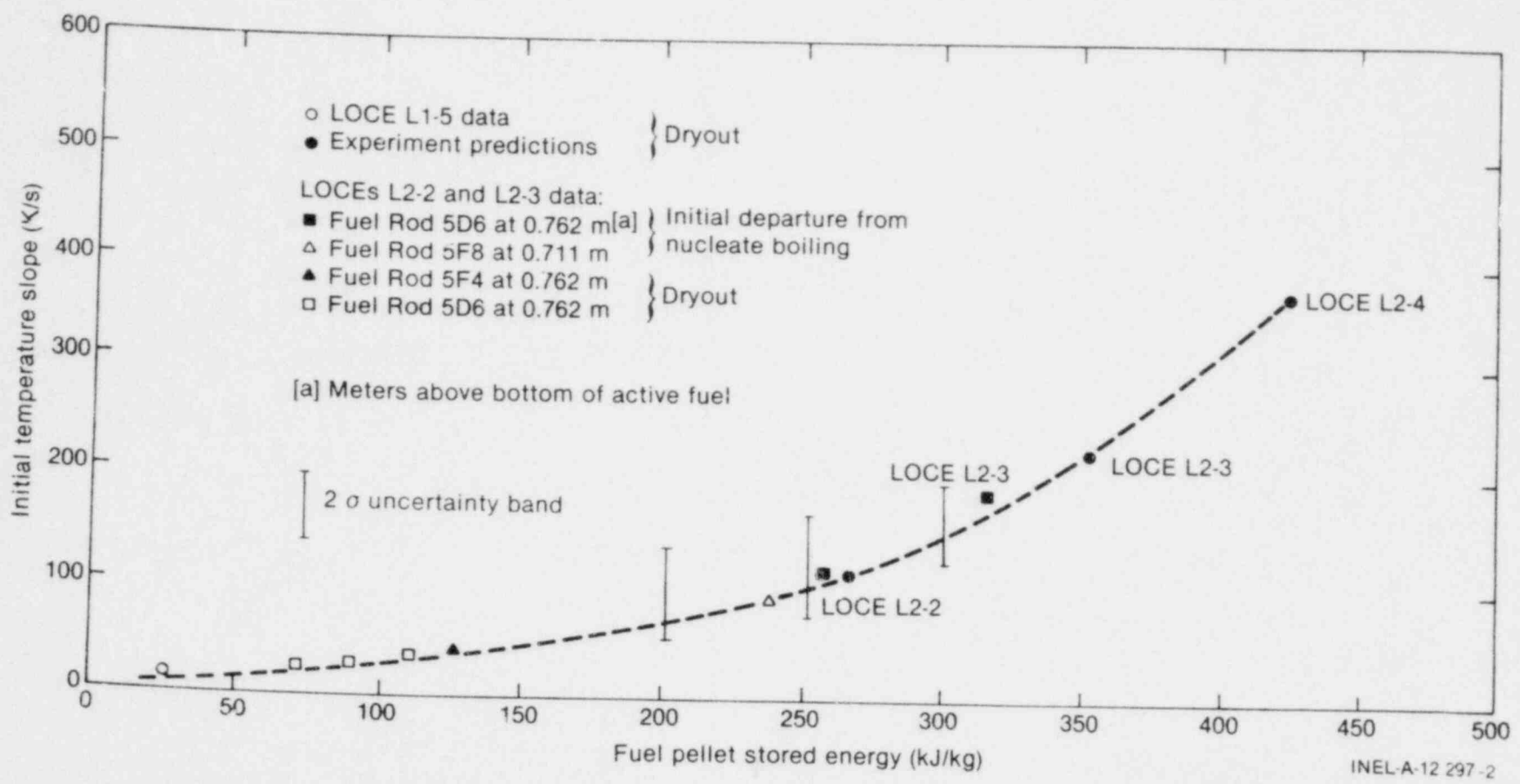


Figure 11. Initial fuel rod cladding temperature slope as a function of fuel rod stored energy.

CHF and the second is the minimum film boiling temperature (ΔT_{min}). A review of heat transfer correlations used in RELAP4/MOD6 has been performed, and a 3-D plotting routine has been used to plot out the heat transfer surface calculated by RELAP4/MOD6.^a A comparison of ΔT_{min} versus X (quality) curve data from a General Electric Company Test⁹ and data generated by the HTS2 routine of RELAP4/MOD6 is shown in Figure 12. Figure 12 shows that RELAP4/MOD6 will never predict rewetting when the local equilibrium quality is greater than 50% at 6.87 MPa. The reason is that Hsu-Buckner's CHF correlation¹⁰ used by RELAP4/MOD6 was developed by correlating the Semiscale high-flow CHF data and may not be suitable for LOFT mid-flow cases (mass flux of 100 to 600 kg/s-m²). As an alternate approach, the Biasi CHF correlation⁶ which covered the mass flux ranges from 100 to 6000 kg/s-m² has been built into RELAP4/MOD6. Figure 13 presents a similar comparison to that shown in Figure 12. With the Biasi CHF correlation, RELAP4/MOD6 can calculate rewetting for quality higher than 50%. However, the trend with respect to mass flux is the opposite of that shown by the General Electric Company minimum film boiling temperature test data⁹ which shows ΔT_{min} increasing as mass flux increases. It should also be noted that the RELAP4/MOD6 data show lower temperatures than is shown in the experimental data. However, the uncertainty on the minimum film boiling temperature test data from General Electric Company is very large.

The LOCE L2-3 posttest analysis was performed with RELAP4/MOD6 updated (changed from the configuration used in the EP analyses) to include the Biasi CHF correlation and measured initial test conditions. The fuel rod temperature responses calculated by the posttest analysis followed the experimental data much better than those calculated in the EP analyses and showed an early core-wide rewet. Therefore, it is concluded that the disparity between the fuel rod cladding temperature response of the EP and the experimental data is mainly due to an unrealistic heat transfer surface in RELAP4/MOD6.

a. A detailed discussion of the RELAP4/MOD6 heat transfer surface is given in Appendix B.

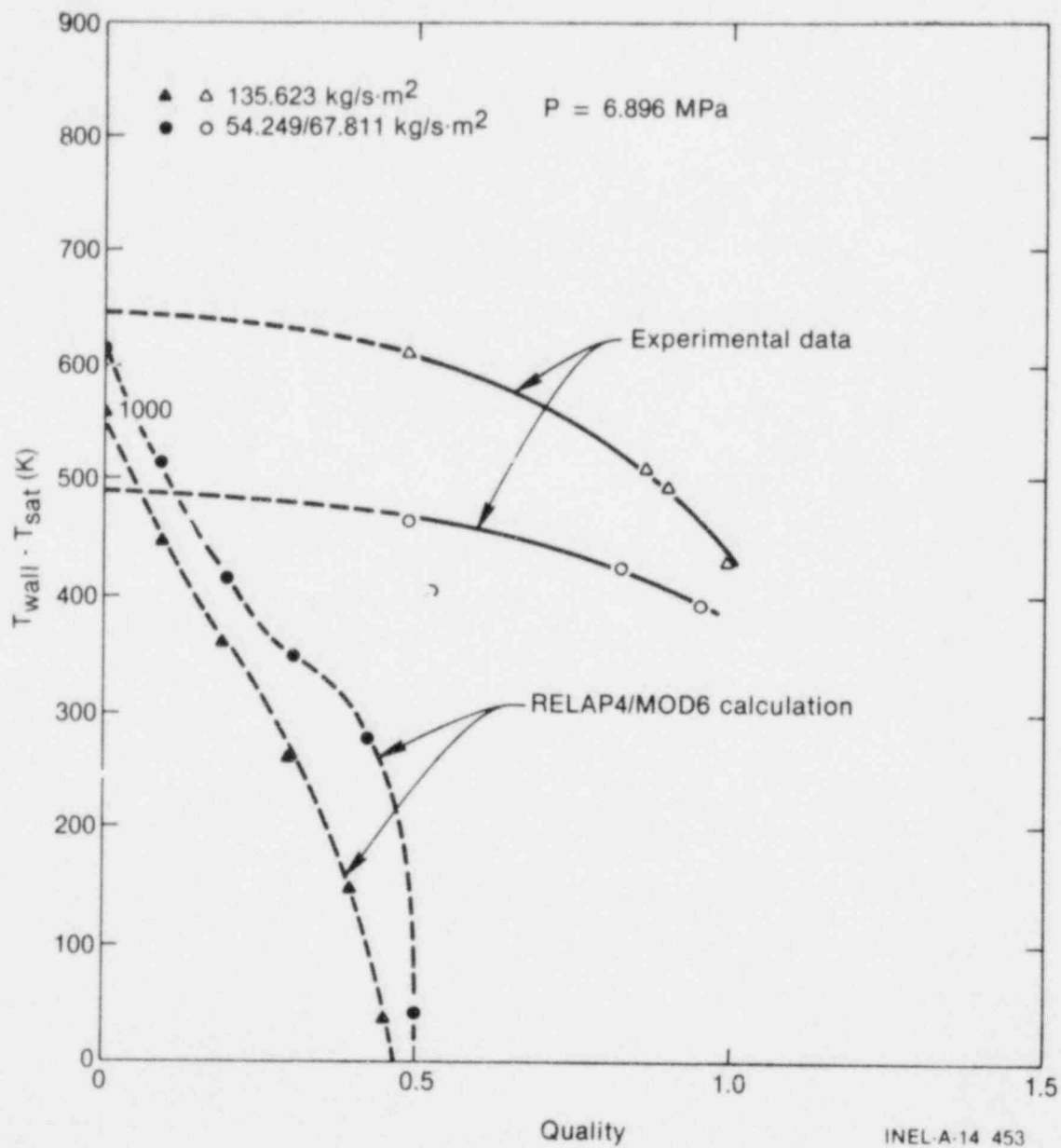


Figure 12. RELAP4/MOD6 calculated minimum film boiling temperature compared with experimental data.

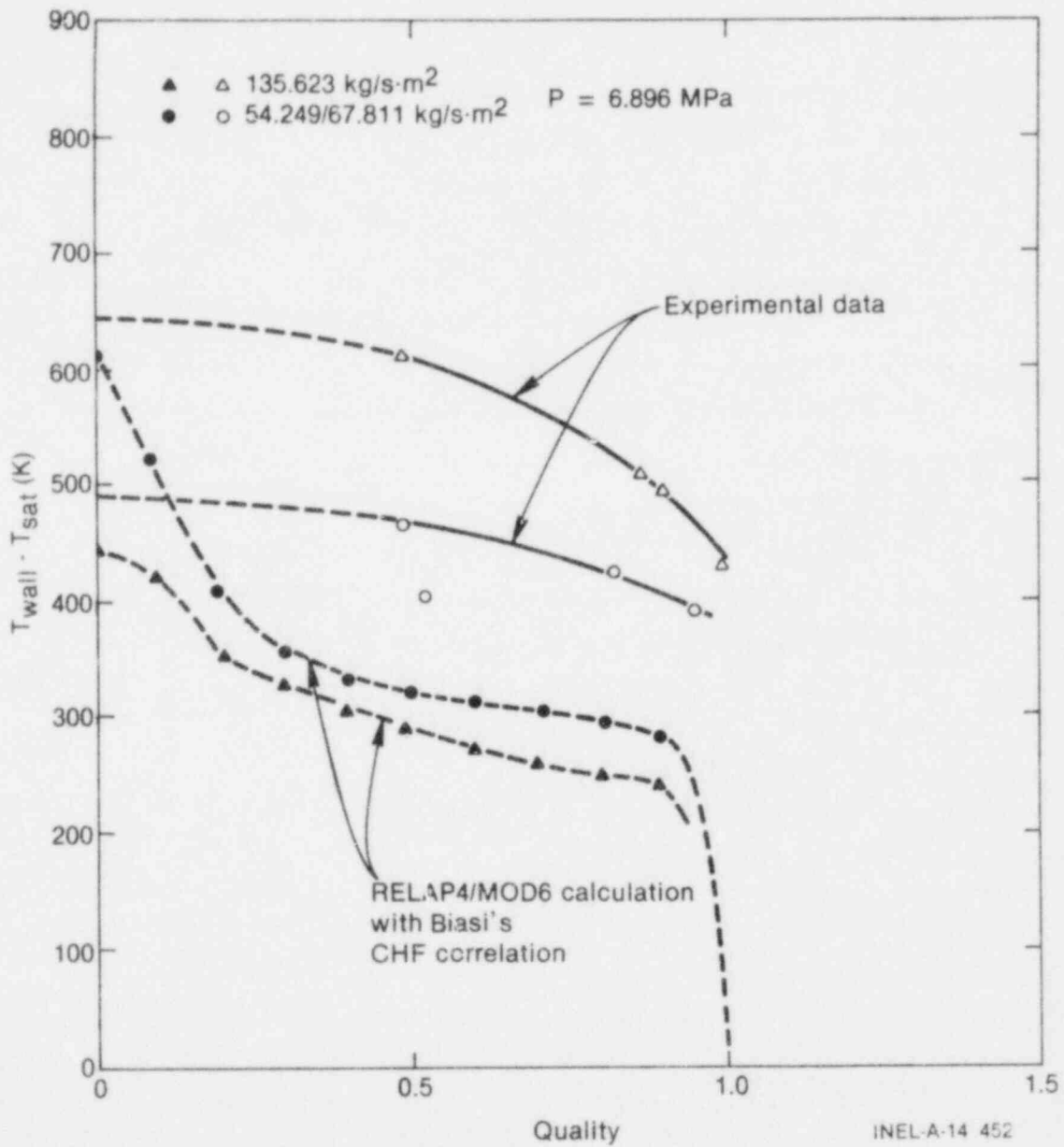


Figure 13. RELAP4/MOD6-Biasi calculated minimum film boiling temperature compared with experimental data.

3.2 Comparison of the Fuel Rod Cladding Surface Temperature Response Between Posttest Analysis and Experimental Data

Figures 14 through 29 show the fuel rod cladding surface temperature response calculated in the posttest analysis compared with the experimental data. A core-wide rewet was predicted in the posttest analysis calculation. The fuel rod cladding surface temperature calculated in the posttest analysis is in reasonably good agreement with the experimental data. However, the peak cladding surface temperature in the posttest calculation was about 70 K higher than was observed in the experimental data. During the first 10 s of the LOCE L2-3 blowdown, the CHF time calculated in the posttest analysis occurred about 0.5 s later than in the experimental data, and for the lower and upper thirds of the fuel rod, the rewet time was calculated to occur about 0.5 to 1.0 s earlier in the posttest calculation than in the experimental data. For the upper third of the fuel rod, the experimental data show that the fuel rod experienced a multiple rewetting. This multiple rewetting phenomenon was calculated in the posttest analysis but was not predicted in the EP. Similarly, the posttest calculation for the second rewetting for the upper third of the fuel rod was about 3.0 to 3.5 s earlier than was shown in the experimental data, and the second CHF time was about 0.5 s later in the calculation than in the experimental data. These discrepancies resulted from the dryout void fraction used in RELAP4/MOD6 and some of the fine hydraulic structures not predicted in the posttest calculation.

The high fuel rod peak cladding surface temperature calculated in the posttest analysis was reinvestigated. A FRAP-T5 code¹¹ model using the flow and heat transfer values calculated by RELAP4/MOD6 as boundary conditions was used to calculate the fuel rod cladding surface temperature. Figure 30 presents the fuel rod cladding surface temperature at the hot spot calculated by FRAP-T5 compared with the experimental data. The FRAP-T5 calculation is in excellent agreement with the experimental data. A study has been made to find the reason why the cladding temperature calculated by FRAP-T5 is lower than that calculated by RELAP4/MOD6. Table 1 shows a comparison of fuel rod models used in the RELAP4/MOD6 and FRAP-T5 codes.

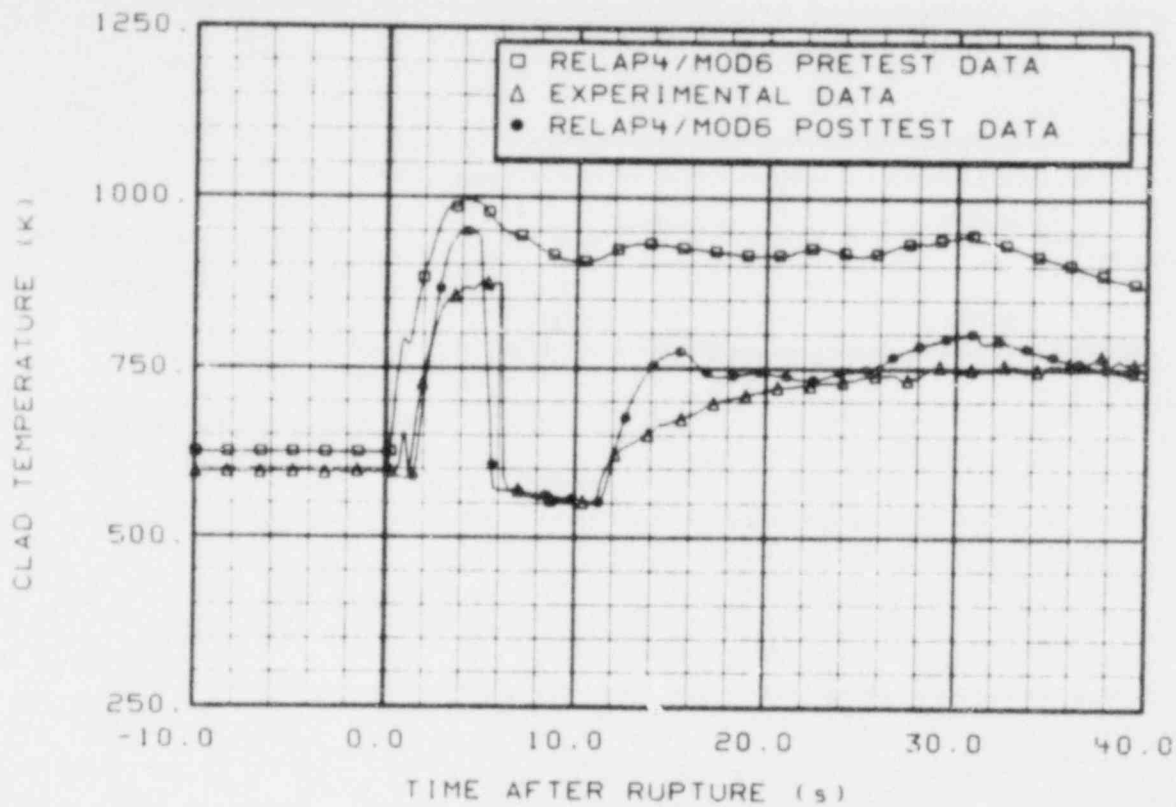


Figure 14. Comparison of cladding temperature on fuel Rod 5F4 at 0.381 m above bottom of core for prediction, posttest, and experimental data.

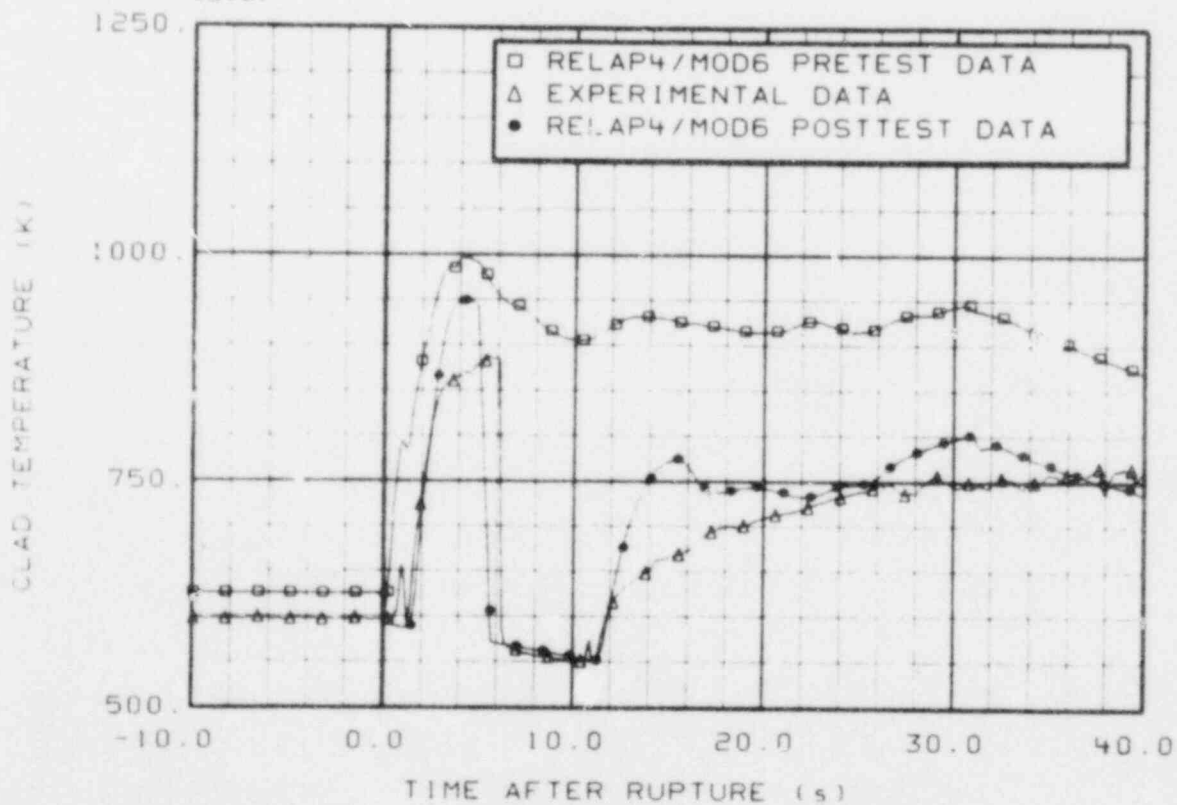


Figure 15. Comparison of cladding temperature on fuel Rod 5J4 at 0.381 m above bottom of core for prediction, posttest, and experimental data.

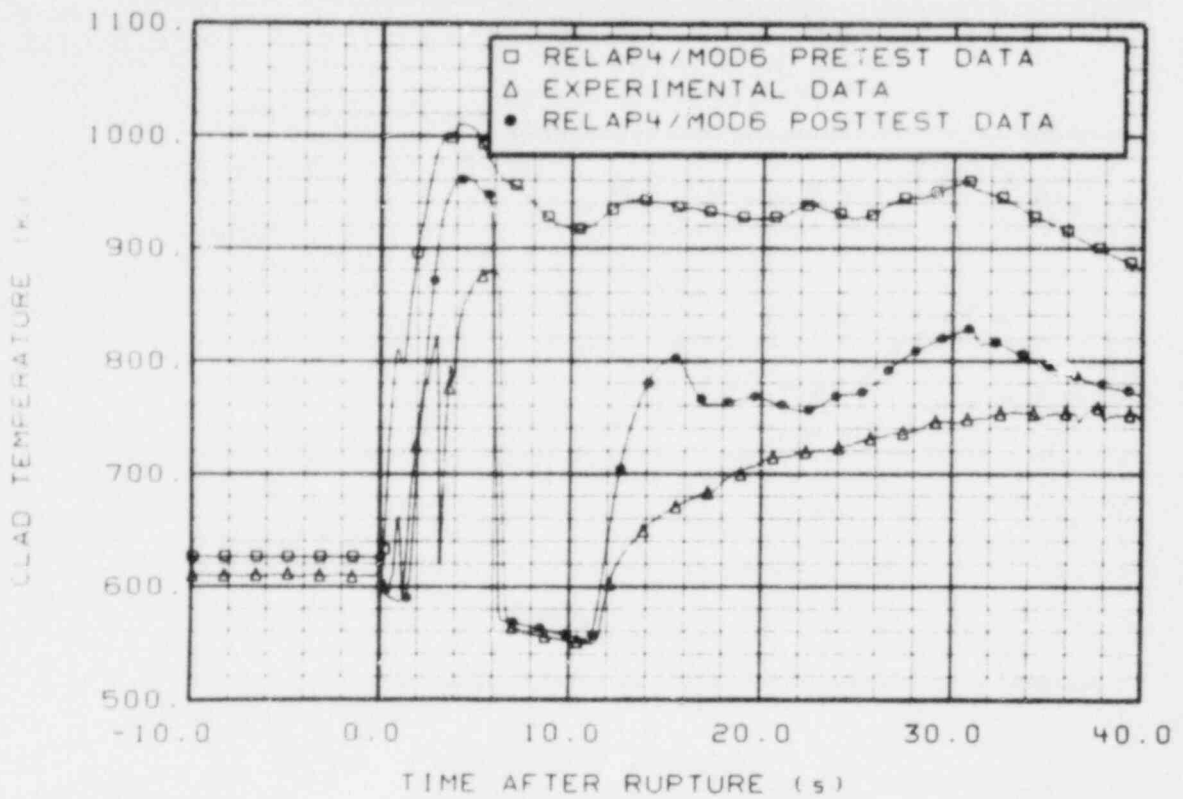


Figure 16. Comparison of cladding temperature on fuel Rod 5F4 at 0.533 m above bottom of core for prediction, posttest, and experimental data.

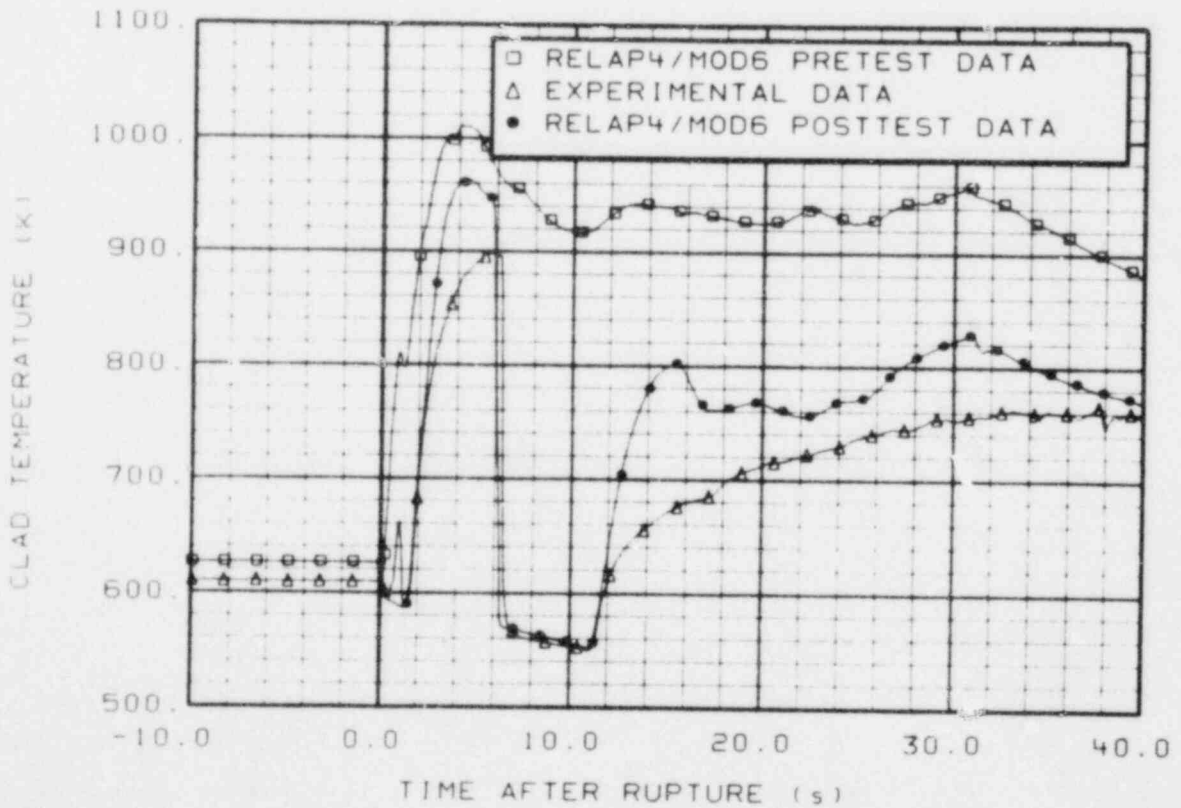


Figure 17. Comparison of cladding temperature on fuel Rod 5J4 at 0.533 m above bottom of core for prediction, posttest, and experimental data.

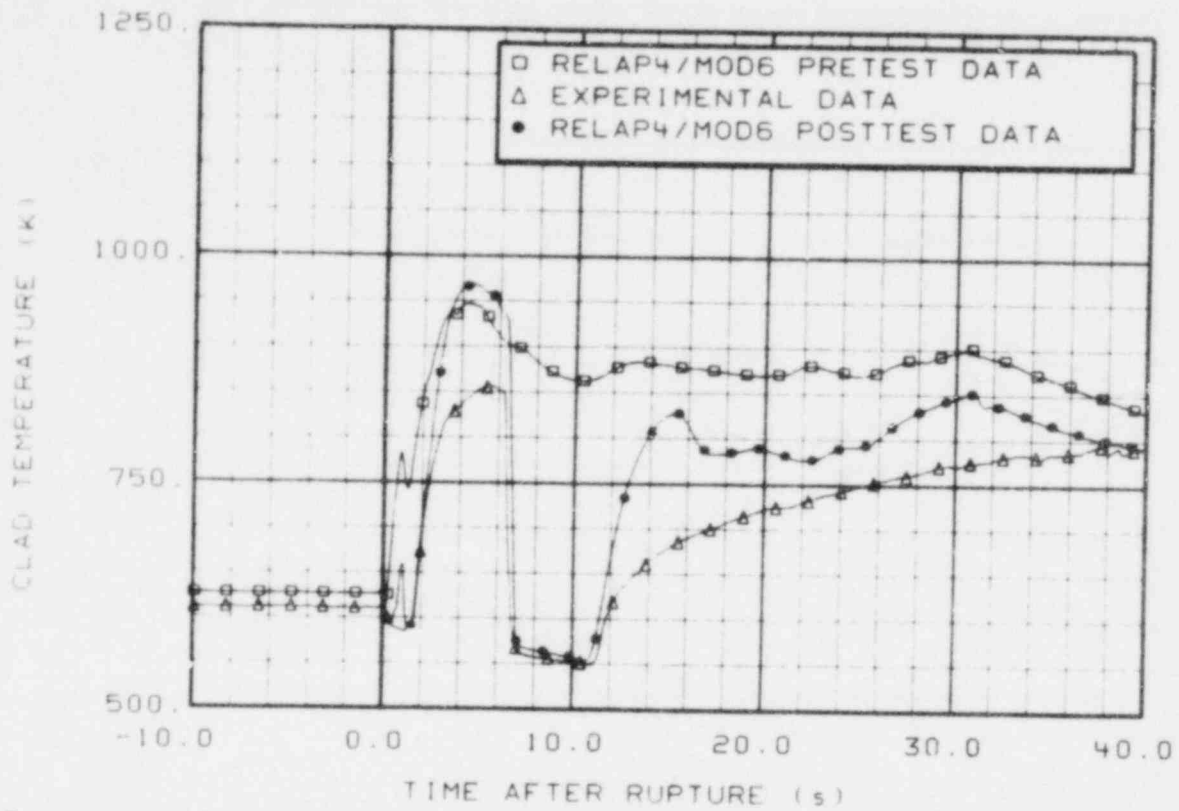


Figure 18. Comparison of cladding temperature on fuel Rod 5F4 at 0.660 m above bottom of core for prediction, posttest, and experimental data.

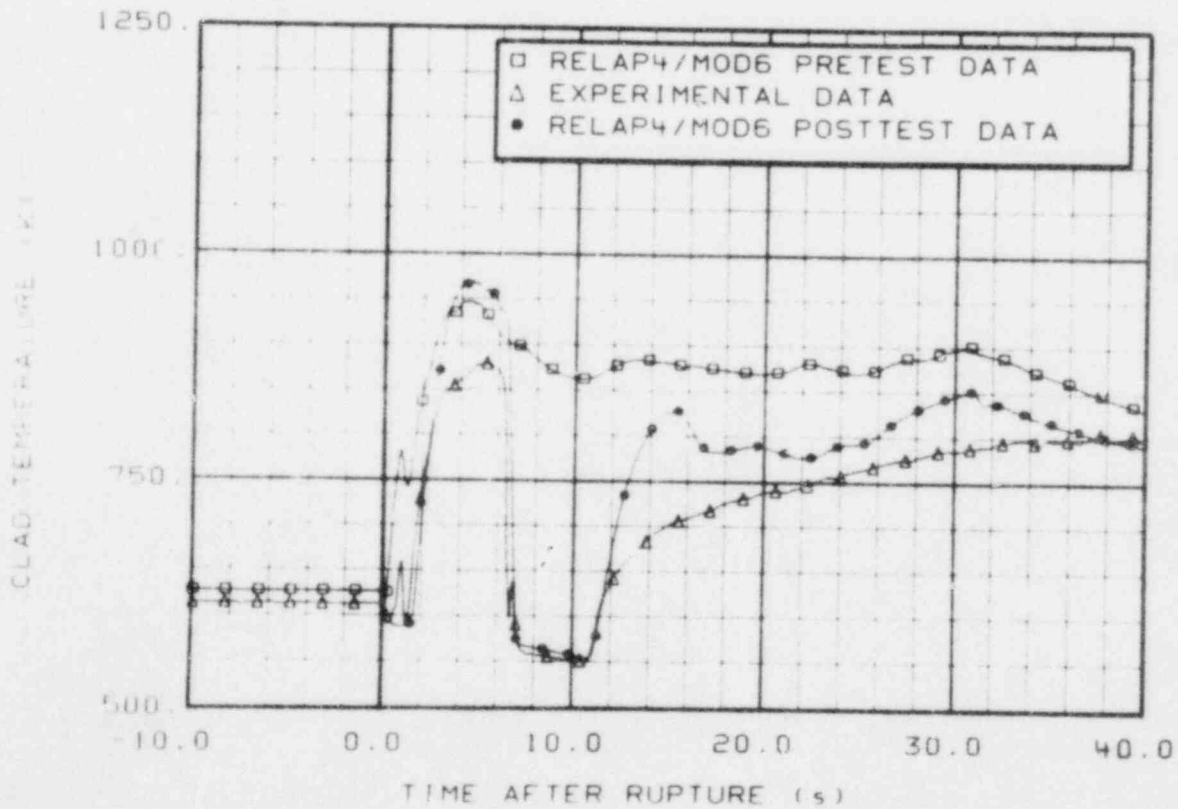


Figure 19. Comparison of cladding temperature on fuel Rod 5J4 at 0.660 m above bottom of core for prediction, posttest, and experimental data.

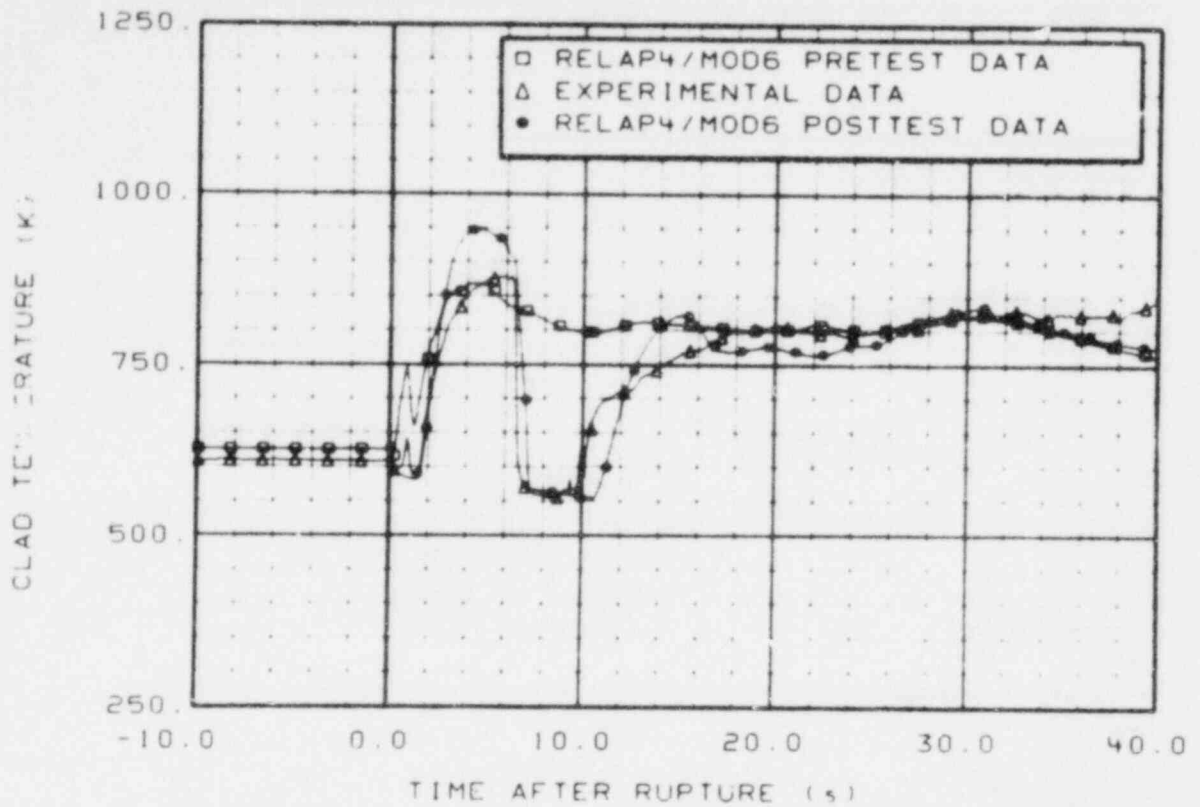


Figure 20. Comparison of cladding temperature on fuel Rod 5D6 at 0.762 m above bottom of core for prediction, posttest, and experimental data.

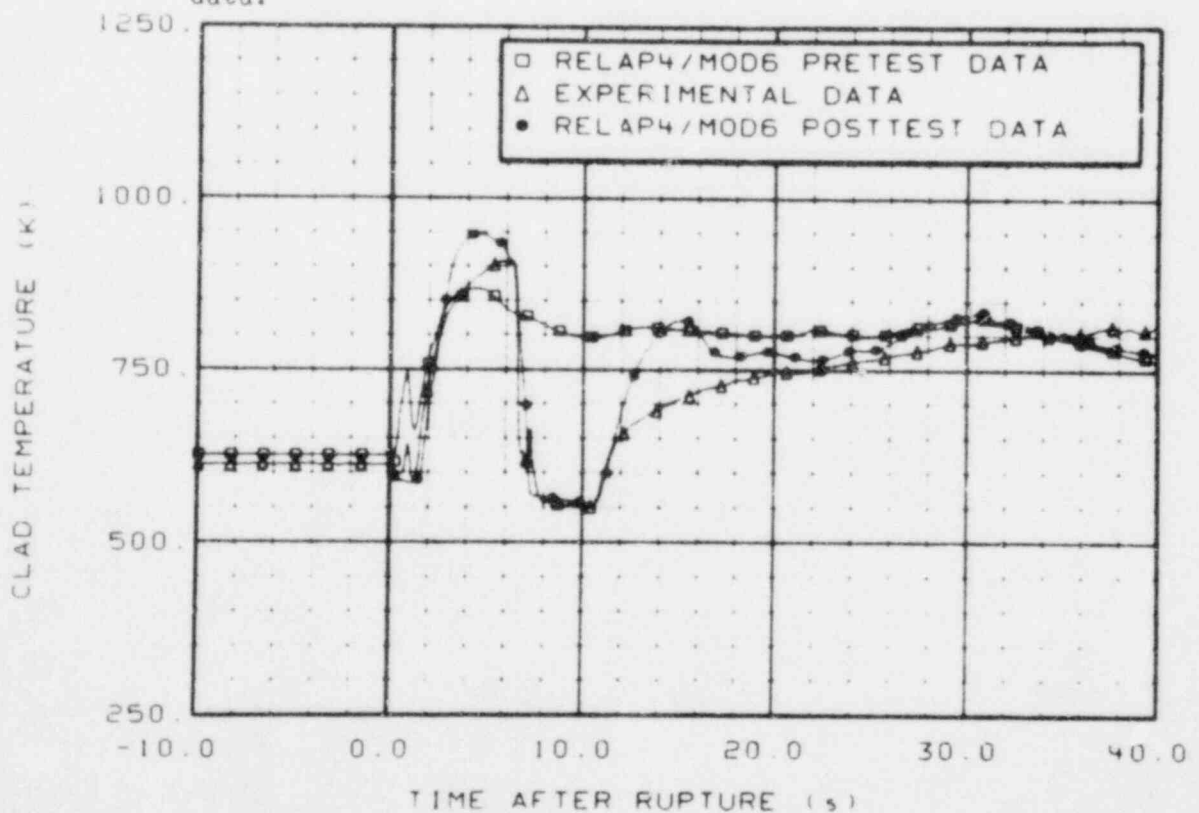


Figure 21. Comparison of cladding temperature on fuel Rod 5F4 at 0.762 m above bottom of core for prediction, posttest, and experimental data.

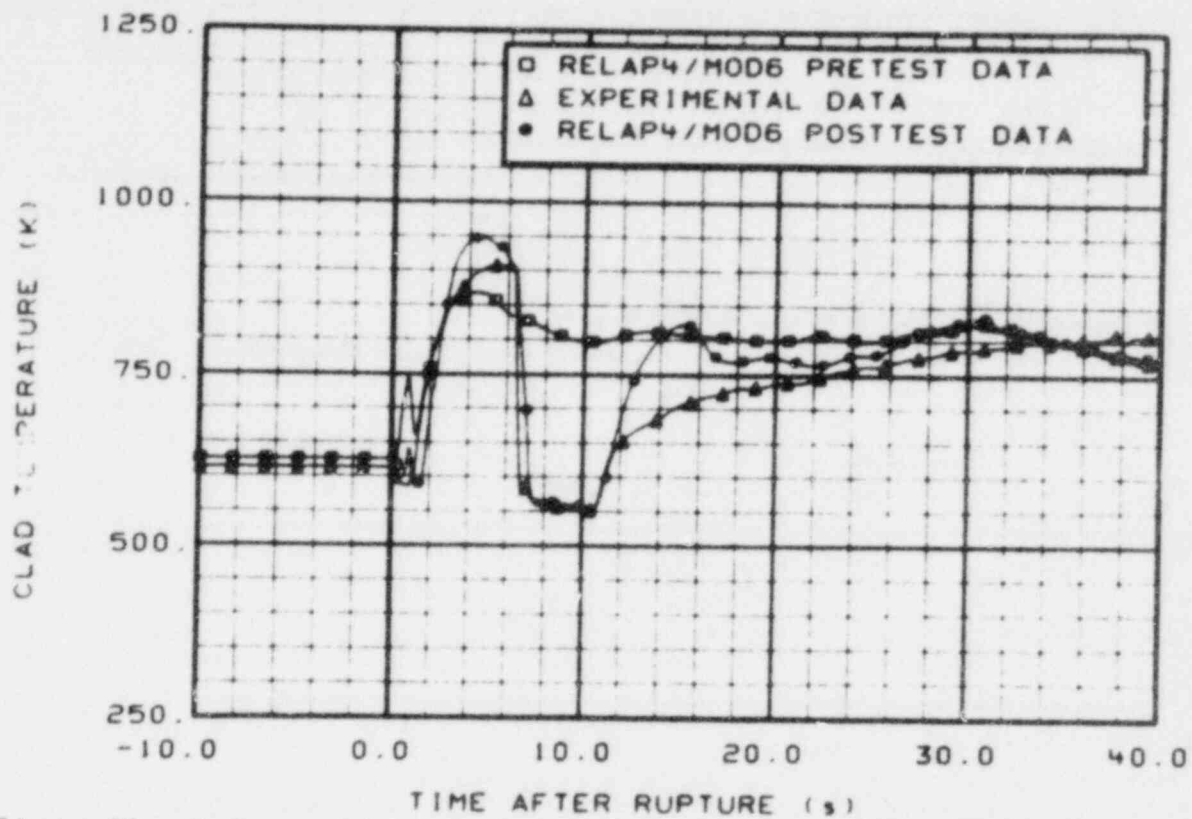


Figure 22. Comparison of cladding temperature on fuel Rod 5J4 at 0.762 m above bottom of core for prediction, posttest, and experimental data.

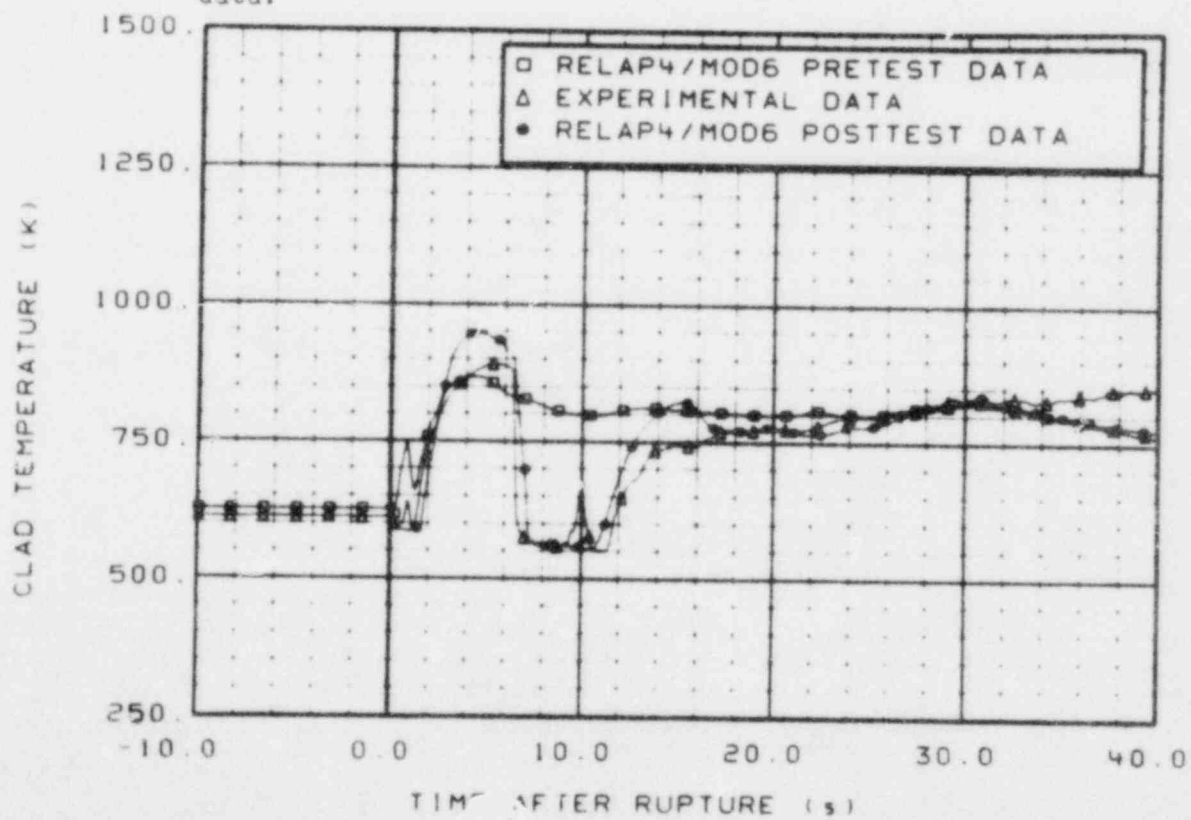


Figure 23. Comparison of cladding temperature on fuel Rod 5L6 at 0.762 m above bottom of core for prediction, posttest, and experimental data.

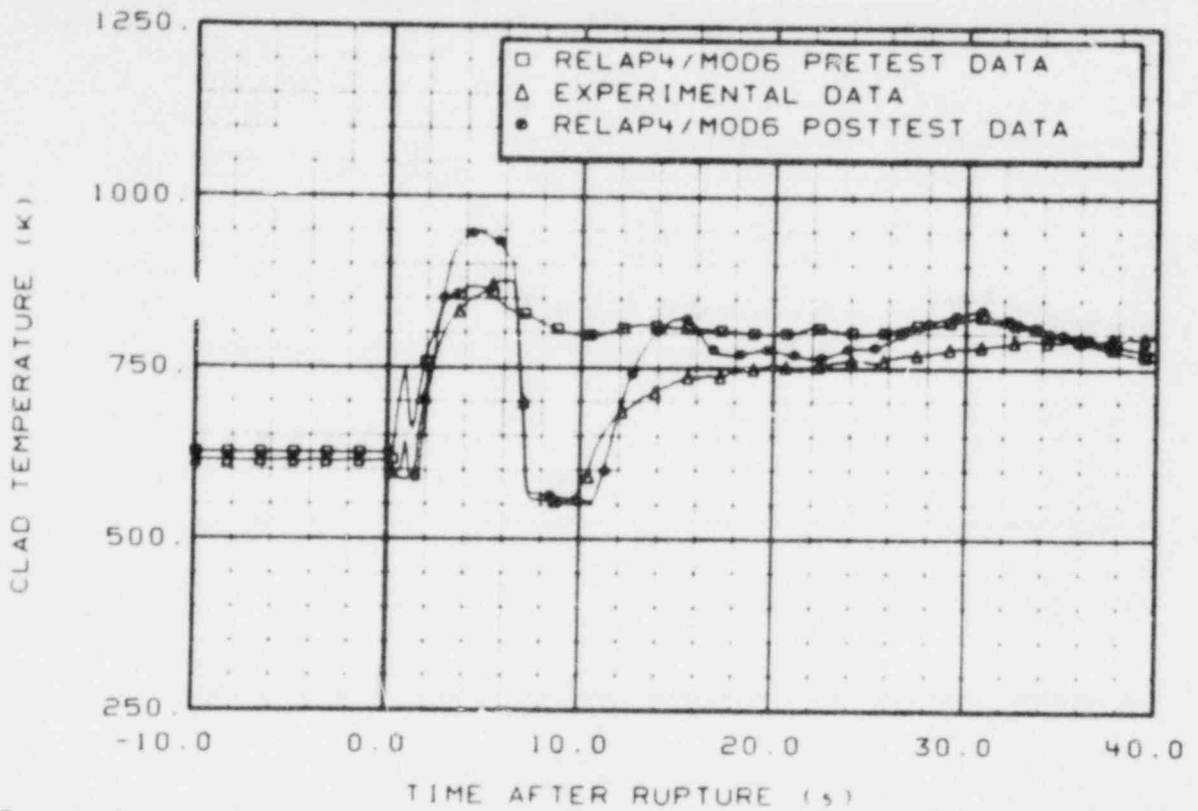


Figure 24. Comparison of cladding temperature on fuel Rod 5D6 at 0.813 m above bottom of core for prediction, posttest, and experimental data.

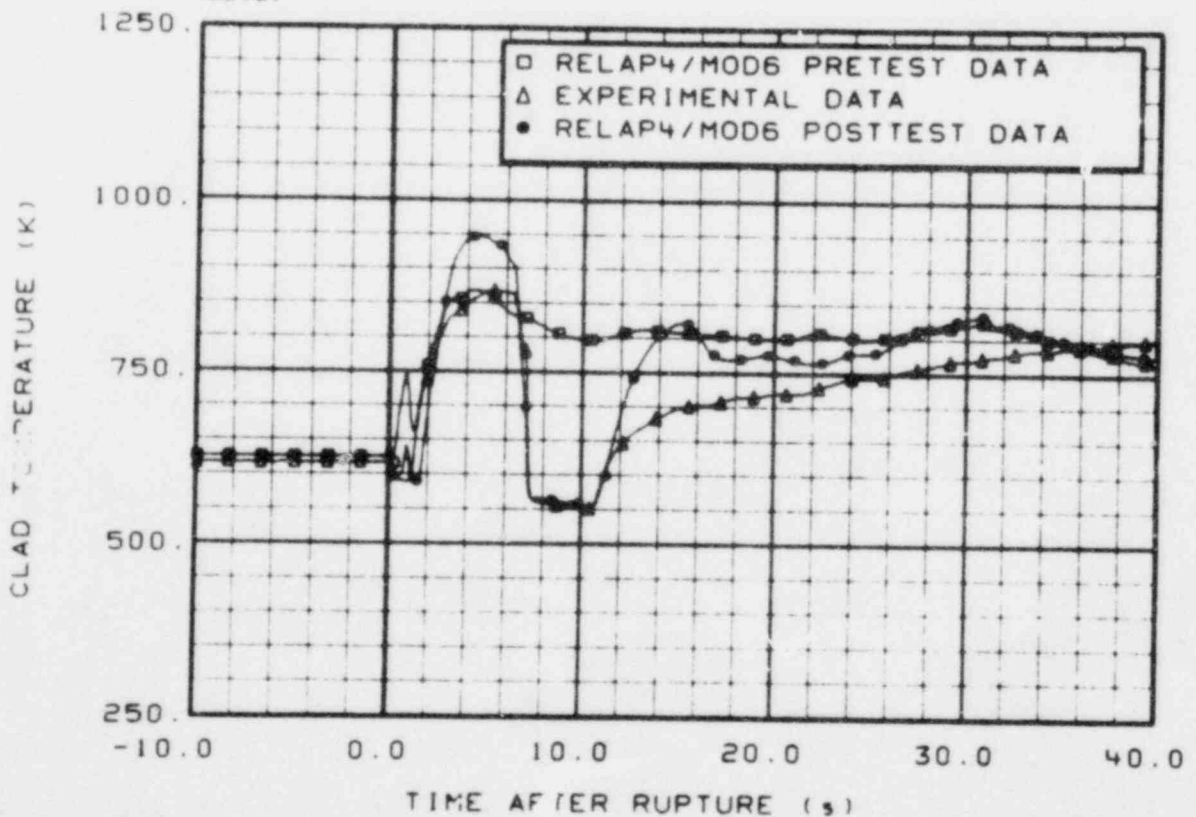


Figure 25. Comparison of cladding temperature on fuel Rod 5L6 at 0.813 m above bottom of core for prediction, posttest, and experimental data.

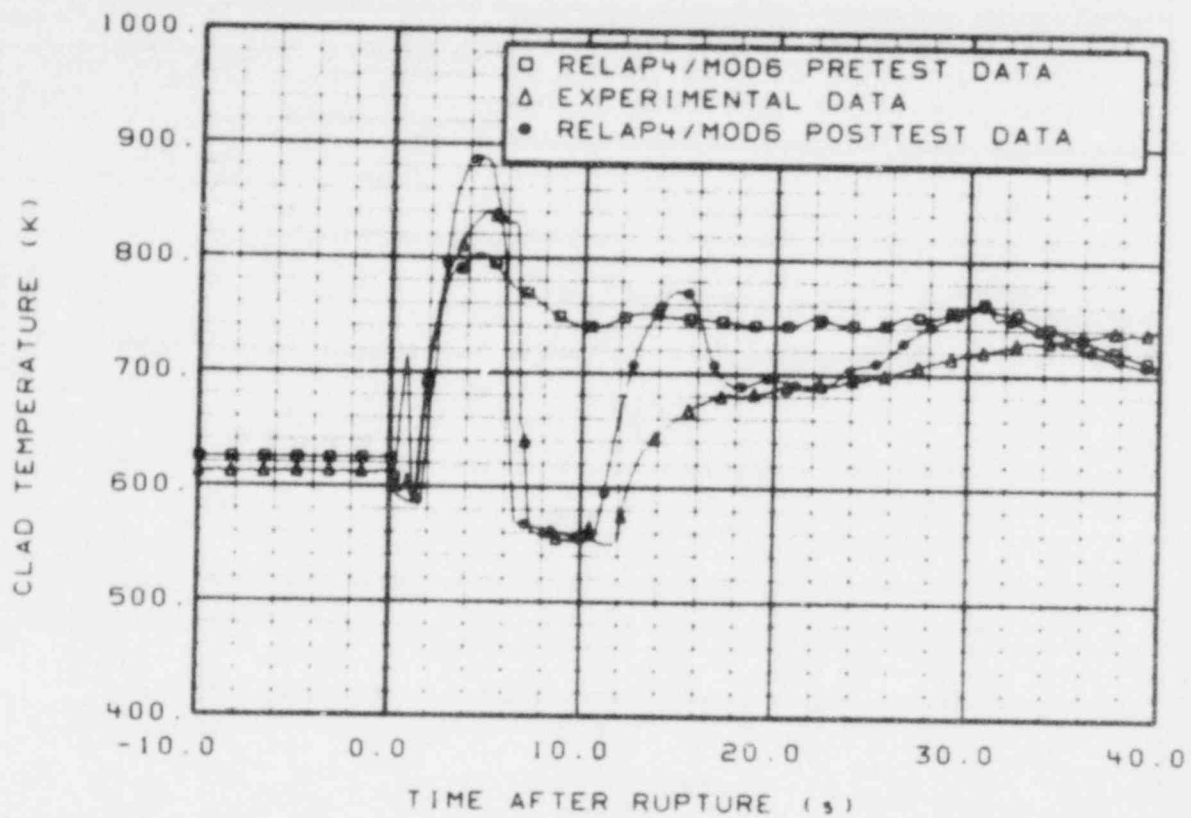


Figure 26. Comparison of cladding temperature on fuel Rod 5D6 at 0.940 m above bottom of core for prediction, posttest, and experimental data.

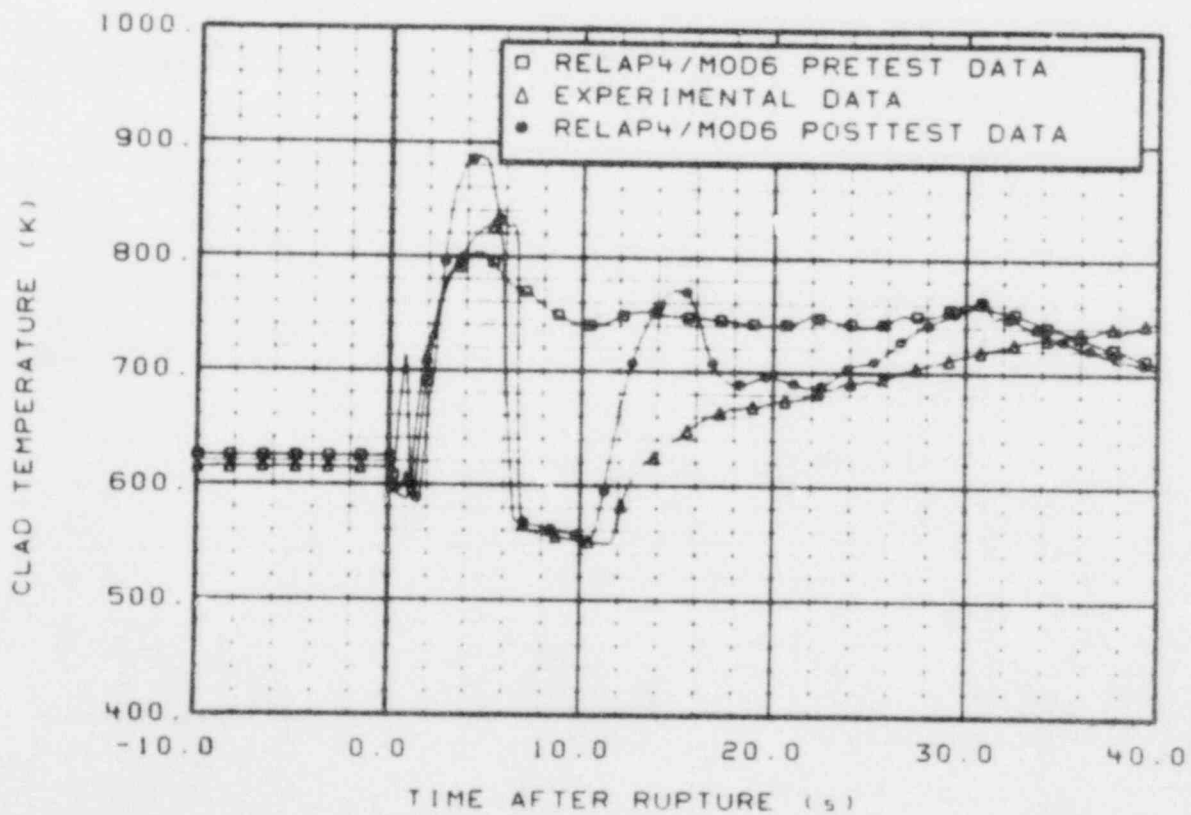


Figure 27. Comparison of cladding temperature on fuel Rod 5L6 at 0.940 m above bottom of core for prediction, posttest, and experimental data.

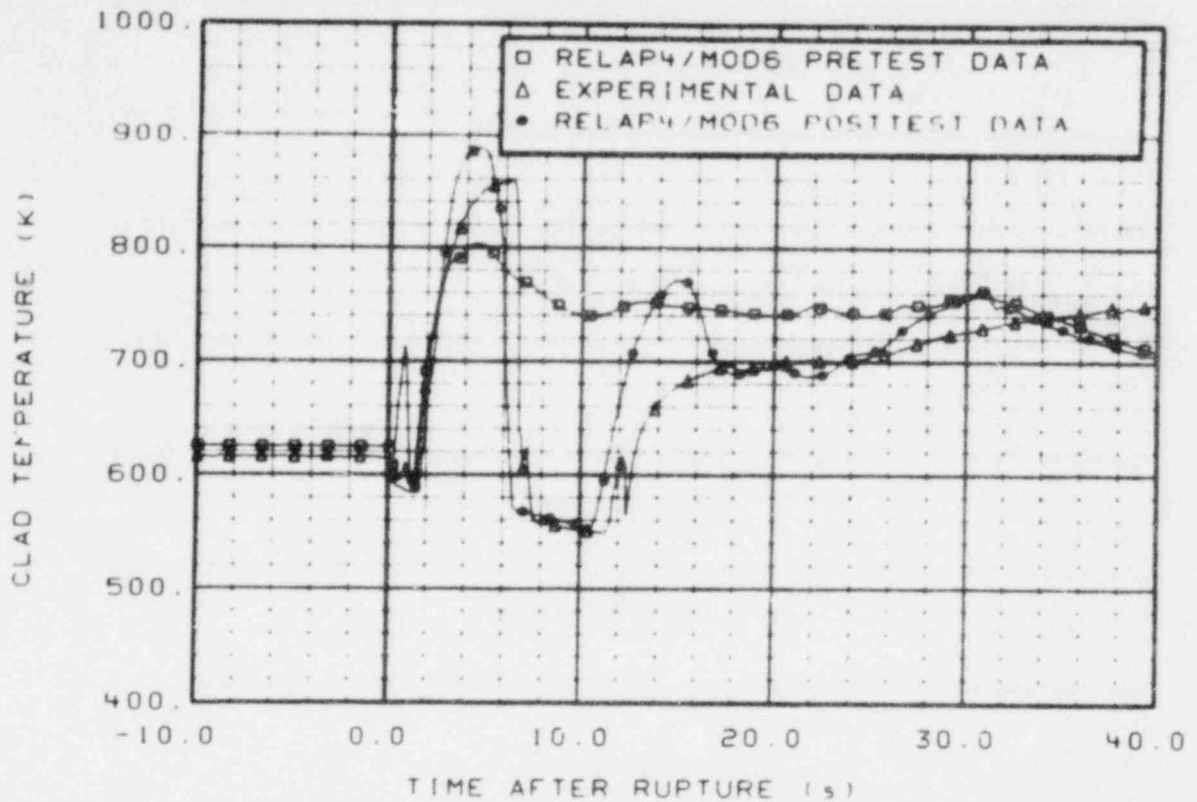


Figure 28. Comparison of cladding temperature on fuel Rod 5D6 at 0.991 m above bottom of core for prediction, posttest, and experimental data.

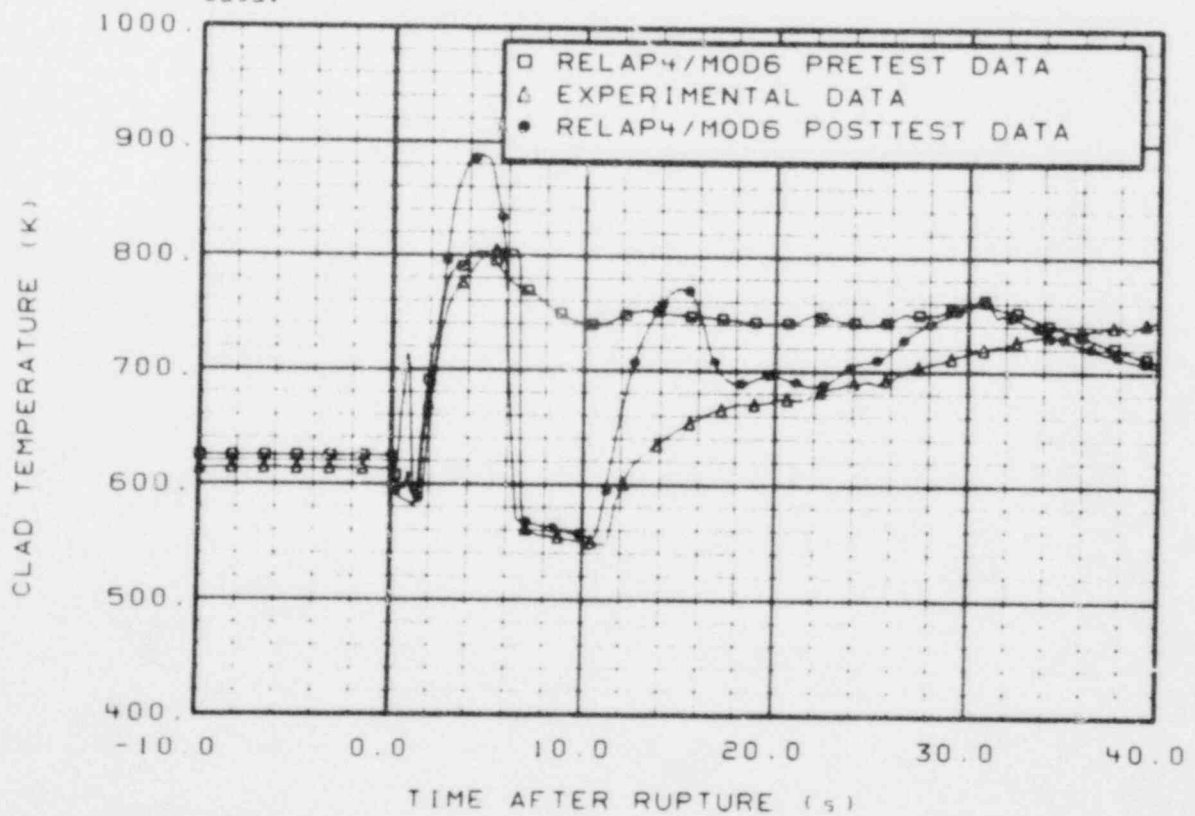


Figure 29. Comparison of cladding temperature on fuel Rod 5L6 at 0.991 m above bottom of core for prediction, posttest, and experimental data.

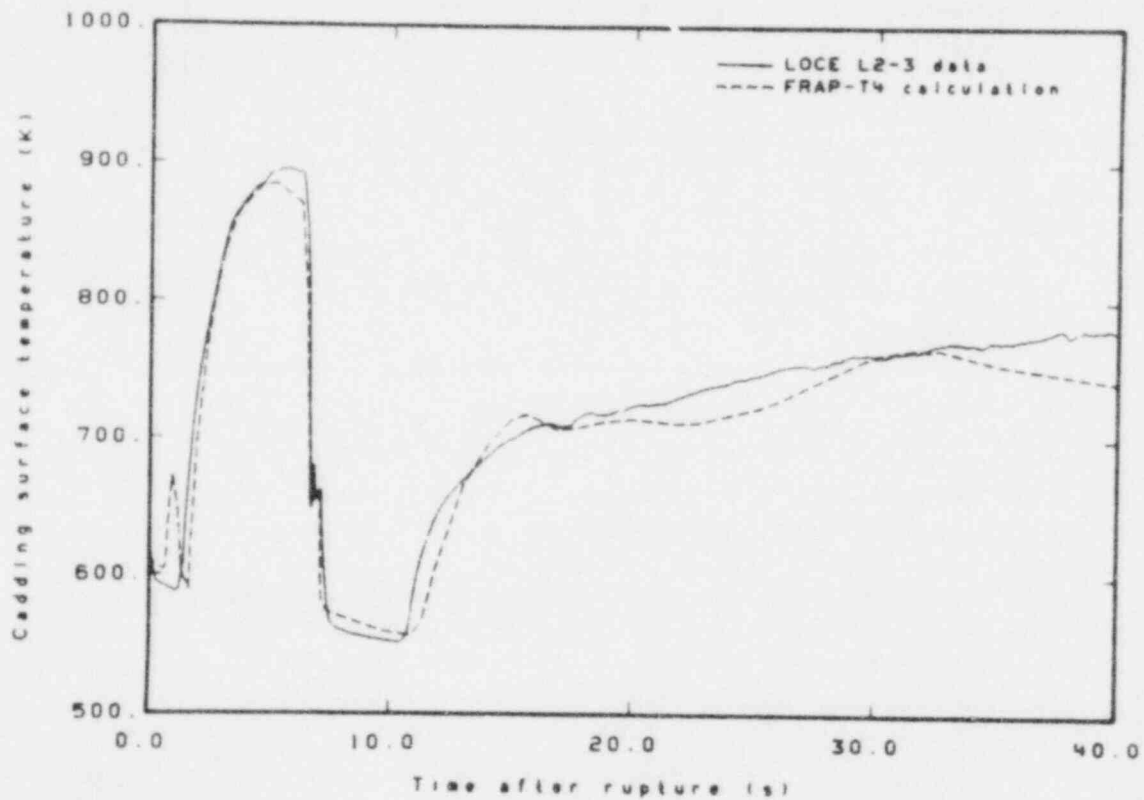


Figure 30. Comparison of cladding temperature on fuel Rod 518 at 0.620 m above bottom of core for FRAP-T4 prediction and experimental data.

TABLE 1. COMPARISON OF FUEL ROD MODELS USED IN RELAP4/MOD6 AND FRAP-T5

<u>Modeling of Fuel Rod Phenomena</u>	<u>RELAP4/MOD6</u>	<u>FRAP-T5</u>
Elastic-plastic fuel and cladding deformation	Radial and axial expansions for pellet and cladding	Radial and axial expansions for pellet and cladding; pellet relocation ^a
Fission gas release	GAPCON model ¹²	GRASS model ¹³
Gap conductance	MacDonald-Broughton model ¹⁴	Ross-Stoute ¹⁵ with fuel crack model
Transient fuel rod gas pressure	Ideal Gas Law	Ideal Gas Law
Material table	MATPRO, Version 7 ¹⁶	MATPRO, Version 11 ¹⁷

a. The fuel relocation and fuel crack models are used together in the FRAP-T5 code.

The main difference between the fuel rod models used in the RELAP4/MOD6 and FRAP-T5 codes is the fuel and gap conductance models. The fuel relocation model used in FRAP-T5 would result in a smaller gap width than that calculated by RELAP4/MOD6, and a smaller gap width would result in lower initial storage energy. During the heat up period of the blowdown, the heat up rate calculated by FRAP-T5 is smaller than that calculated by RELAP4/MOD6 because the storage energy calculated by FRAP-T5 is lower than that calculated by RELAP4/MOD6. Therefore, the cladding surface temperature calculated by FRAP-T5 for LOCE L2-3 is lower than that calculated by RELAP4/MOD6.

4. CONCLUSIONS

The posttest analysis using RELAP4/MOD6 calculated the hydraulic behavior in the LOFT system for LOCE L2-3 very well. A core-wide rewet was calculated by RELAP4/MOD6 when modified to include the Biasi CHF correlation. When FRAP-T5 was used to calculate the fuel rod cladding surface temperature, the calculation was in excellent agreement with the experimental data. However, the ΔT_{\min} trend with respect to mass flux calculated by RELAP4/MOD6 was opposite to the minimum film boiling test data (ΔT_{\min} increases as mass flux increases) from General Electric Company. The calculated CHF time and rewetting time were a little too late and too early, respectively. The transition time from subcooled to saturated break flow calculated in the posttest analysis was a little too late. To solve the above discrepancies, the following future work is planned:

1. More accurate ΔT_{\min} tests for the mass flux from 10 to 300 kg/s-m² will be performed to check the RELAP4/MOD6 predicted ΔT_{\min} and the ΔT_{\min} trend with respect to mass flux calculated by RELAP4/MOD6.
2. The fuel rod model used in RELAP4/MOD6 will be changed to be consistent with the model used in FRAP-T5.
3. The dryout criterion in RELAP4/MOD6 will be reevaluated by comparing more existing experimental data.

4. A detailed understanding of post-CHF heat transfer to develop mechanistic models for analyzing and correlating the data will be made.

5. REFERENCES

1. W. H. Grush et al., Best Estimate Experiment Predictions for LOFT Nuclear Experiments L2-2, L2-3, and L2-4, LOFT-TR-101, November 1978.
2. E. J. Kee and W. H. Grush, Best Estimate Prediction for LOFT Nuclear Experiment L2-3, EP-L2-3, April 1979.
3. S. R. Fisher et al., RELAP4/MOD6 - A Computer Program for Transient Thermal-Hydraulic Analysis of Nuclear Reactors and Related Systems - User's Manual, CDAP-TR-003, January 1978.
4. L. J. Siefken et al., FRAP-T4 - A Computer Code for the Transient Analysis of Oxide Fuel Rods, CDAP-TR-78-027, July 1978.
5. D. L. Reeder, LOFT System and Test Description (5.5-ft Nuclear Core 1 LOCEs), NUREG/CR-0247, TREE-1208, July 1978.
6. L. Biasi et al., "Studies on Burnout - Part 3," Energia Nucleare, 14, 1967, pp. 530-536.
7. P. G. Prassinis et al., Experiment Data Report for LOFT Power Ascension Experiment L2-3, NUREG/CR-0792, TREE-1326, July 1979.
8. E. L. Tolman et al., Fuel Rod Response for LOFT Test L2-2 (MLHGR = 26.3 kW/m), LTR 20-97, January 1979.
9. Y. Y. Hsu and W. D. Buckner, "A Correlation for the Onset of Transient CHF," cited in L. S. Tong and G. L. Bennett, "NRC Water Reactor Safety Research Program," Nuclear Safety, 18, 1, January/February 1977.
10. General Electric Company, Film Boiling and Rewetting, NEDE-20975, August 1975.
11. L. J. Siefken, FRAP-T5 - A Computer Code for the Transient Analysis of Oxide Fuel Rods, NUREG/CR-0840, TREE-1281, June 1979.
12. C. R. Hann, C. E. Beyer, L. J. Parchen, GAPCON-THERMAL-1: A Computer Program for Calculating the Gap Conductance in Oxide Fuel Pins, BNWL-1778, September 1973.
13. J. Rest, GRASS-SST: A Comprehensive Mechanistic Model for the Prediction of Fission Gas Behavior in UO₂ Based Fuels During Steady State and Transient Conditions, NUREG/CR-0202, ANL-78-53, June 1978.
14. P. E. MacDonald and L. B. Thompson, MATPRO 09: A Handbook of Materials Properties for Use in the Analysis of Light Water Reactor Fuel Rod Behavior, TREE-NUREG-1005, December 1976, pp. 320-324.
15. A. M. Ross and R. L. Stoute, Heat Transfer Coefficient Between UO₂ and Zircaloy-2, AECL-1552, June 1962.

16. P. E. MacDonald and L. B. Thompson, MATPRO 07: A Handbook of Materials Properties for Use in the Analysis of Light Water Reactor Fuel Rod Behavior, ANCR-1263 (NRC-5), February 1976.
17. G. A. Reymann et al., MATPRO - Version 11: A Handbook of Materials Properties for Use in the Analysis of Light Water Reactor Fuel Rod Behavior, NUREG/CR-0497, TREE-1280, February 1979.

APPENDIX A

COMPARISON OF CALCULATED AND MEASURED SYSTEM
HYDRAULICS DATA FOR LOCE L2-3

APPENDIX A

COMPARISON OF CALCULATED AND MEASURED SYSTEM HYDRAULICS DATA FOR LOCE L2-3

The most important system hydraulic parameters calculated for Loss-of-Coolant Experiment L2-3 in the prediction and posttest analyses are compared with the experimental data in Section 2 of the text. To obtain better understanding of the system hydraulics calculated in the posttest analysis, more comparisons are given in this Appendix. Figures A-1 through A-84 show the system hydraulics data calculated in the posttest and prediction analyses compared with the experimental data. In general, the posttest and prediction analysis calculations agreed with the experimental data within the range allowed by the instrument uncertainty.

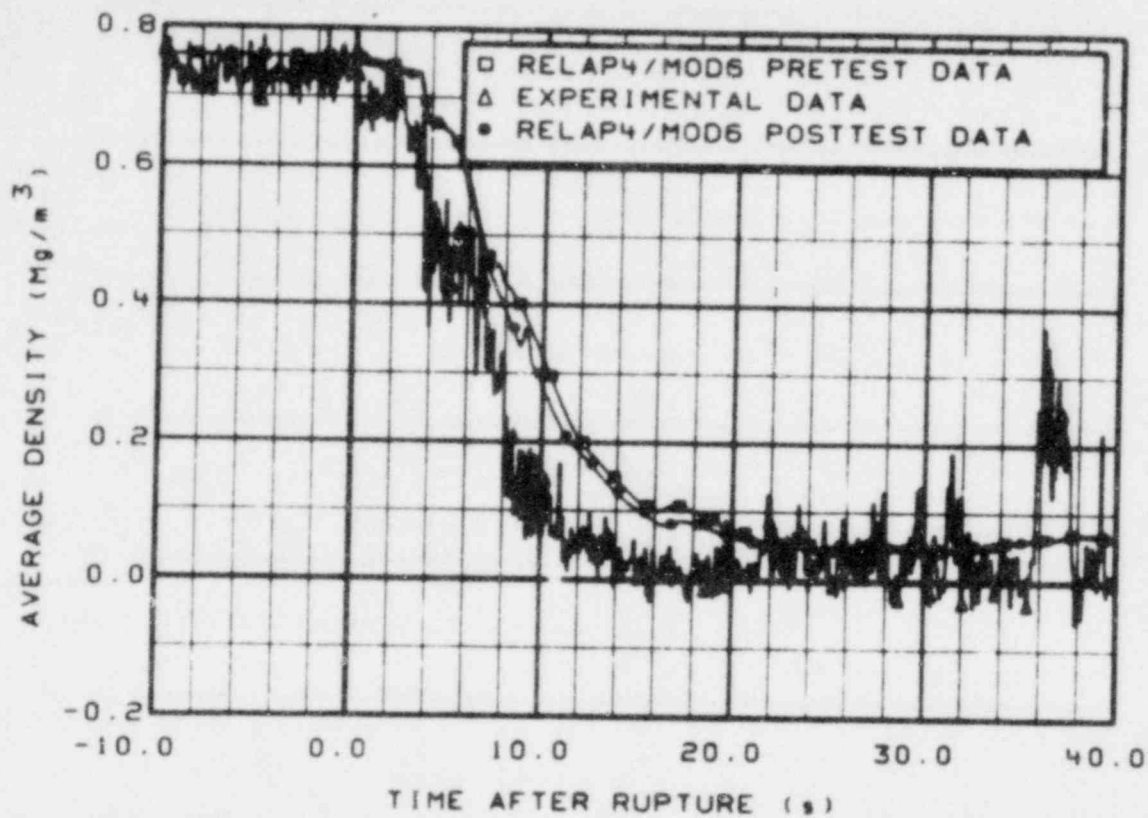


Figure A-1. Comparison of measured average density in broken loop cold leg for prediction, posttest, and experimental data.

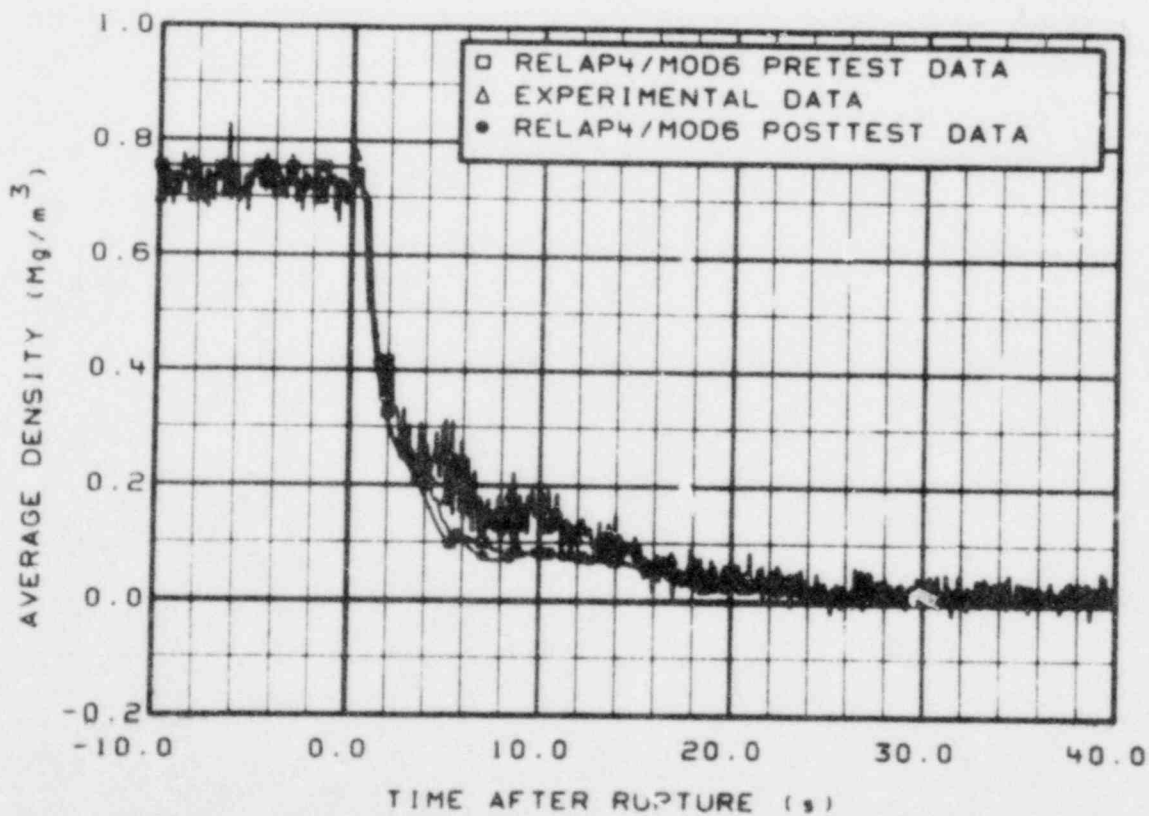


Figure A-2. Comparison of average density in broken loop hot leg for prediction, posttest, and experimental data.

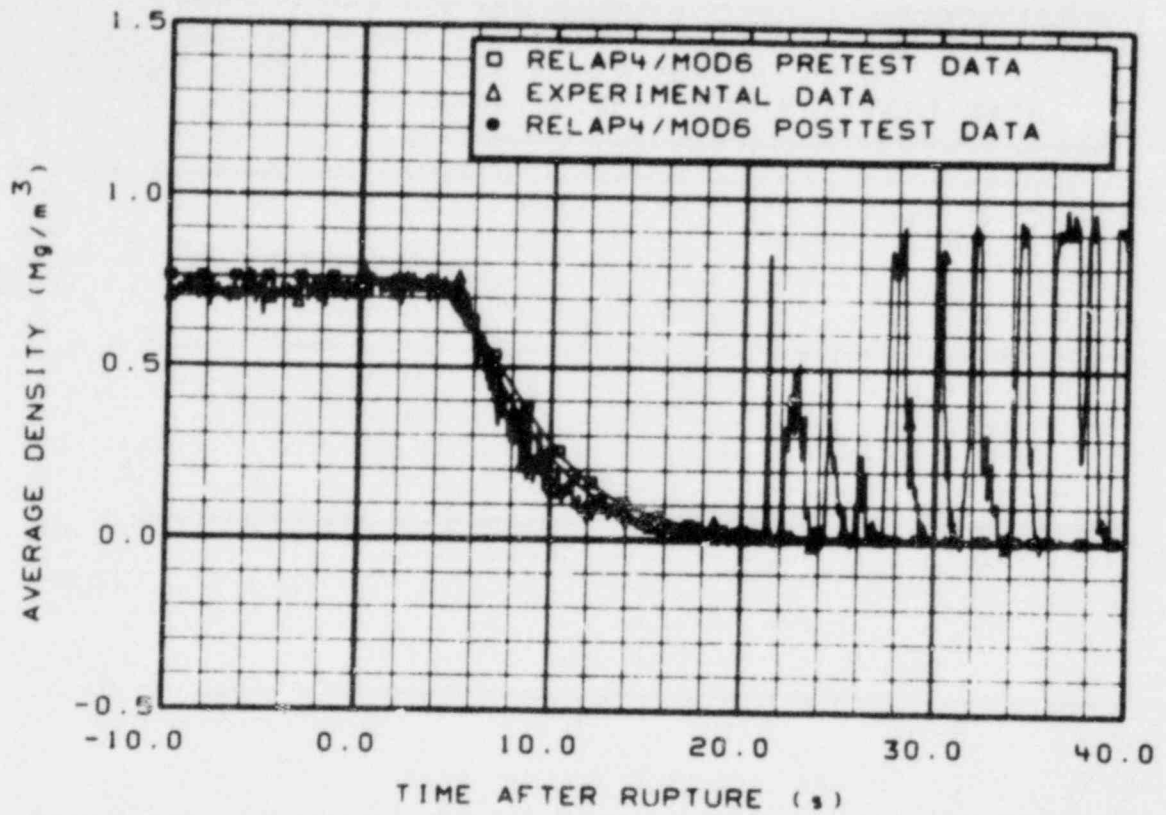


Figure A-3. Comparison of average density in intact loop cold leg for prediction, posttest, and experimental data.

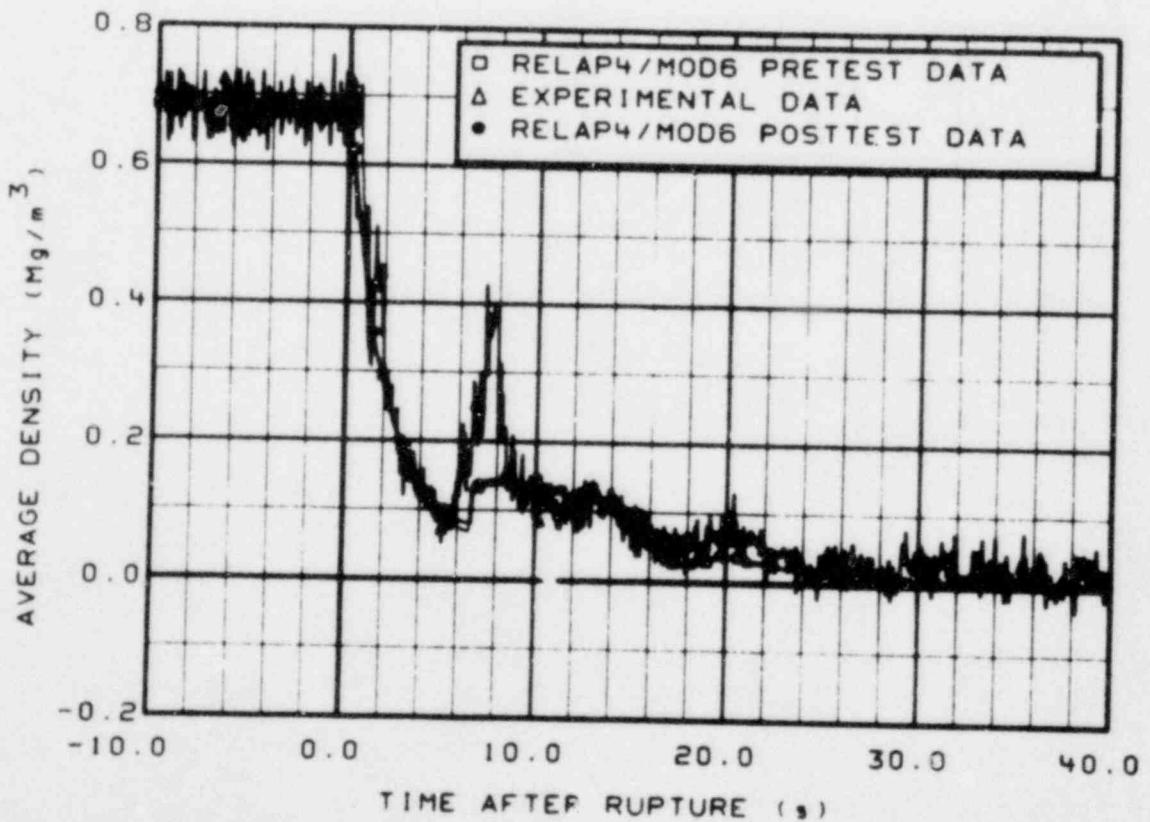


Figure A-4. Comparison of average density in intact loop hot leg for prediction, posttest, and experimental data.

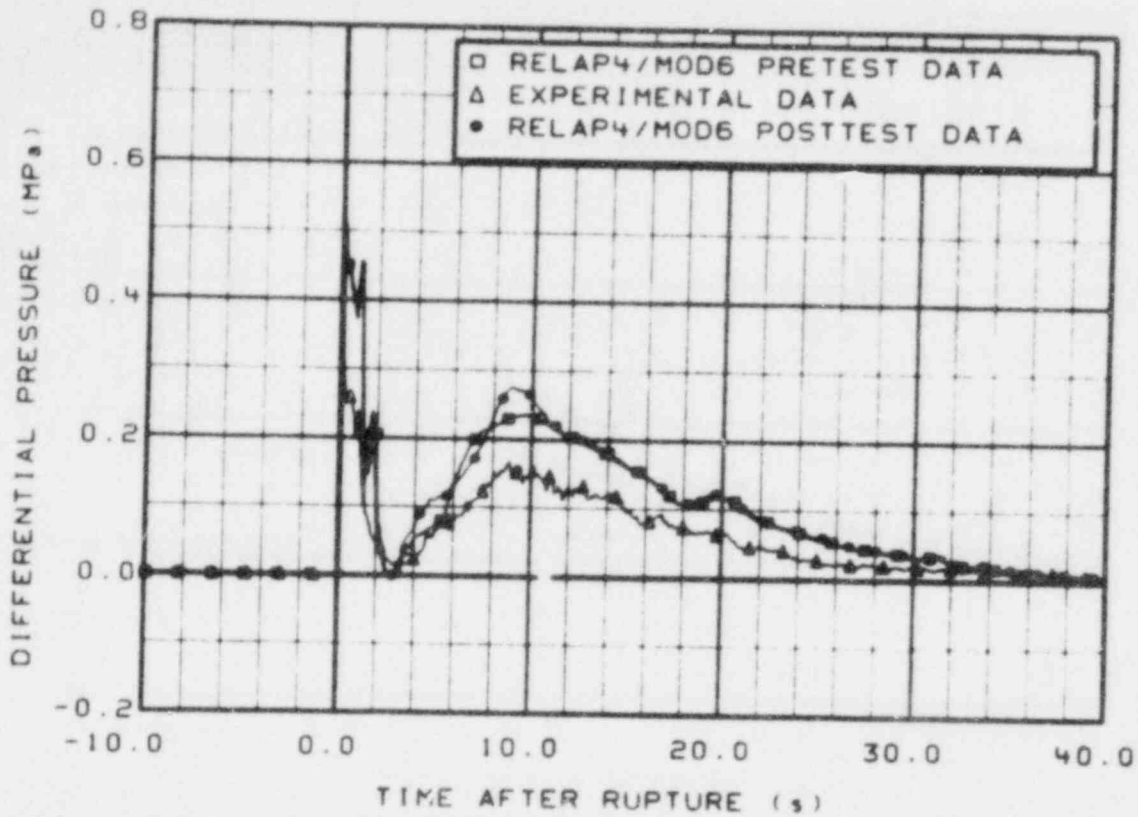


Figure A-5. Comparison of differential pressure across 14- to 5-in. reducer for prediction, posttest, and experimental data.

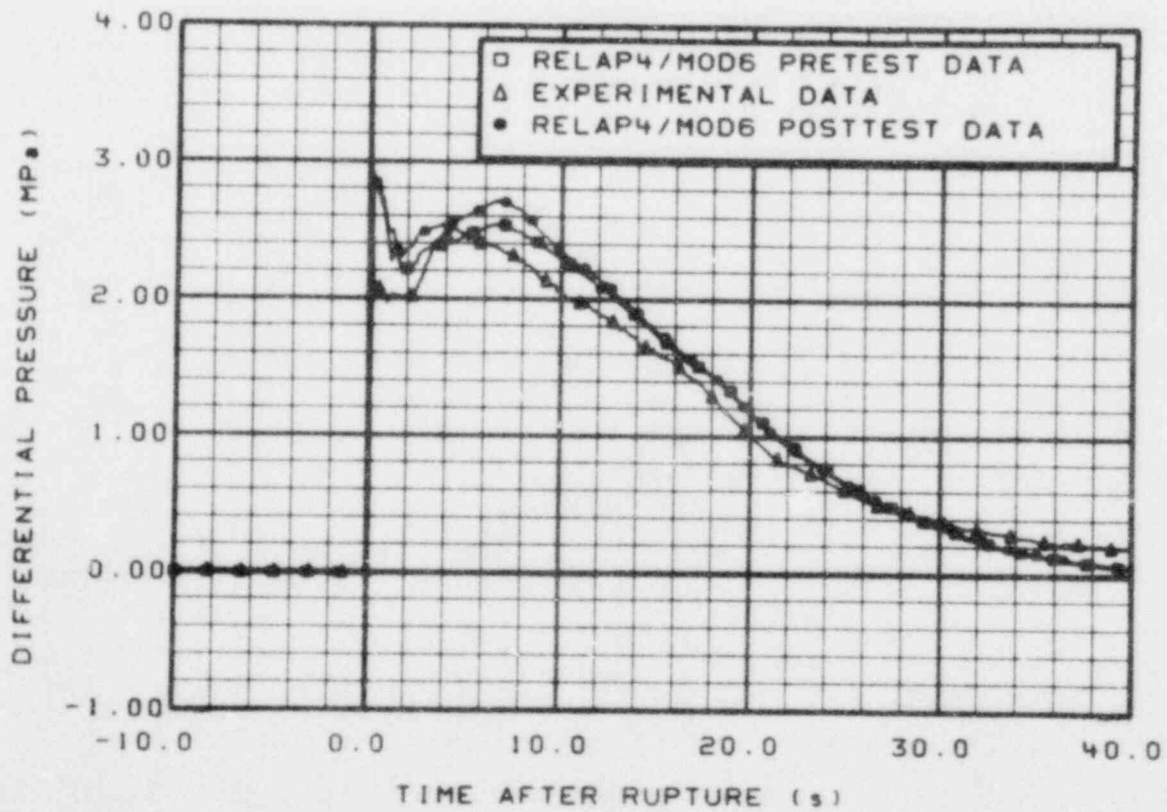


Figure A-6. Comparison of differential pressure across pump simulator for prediction, posttest, and experimental data.

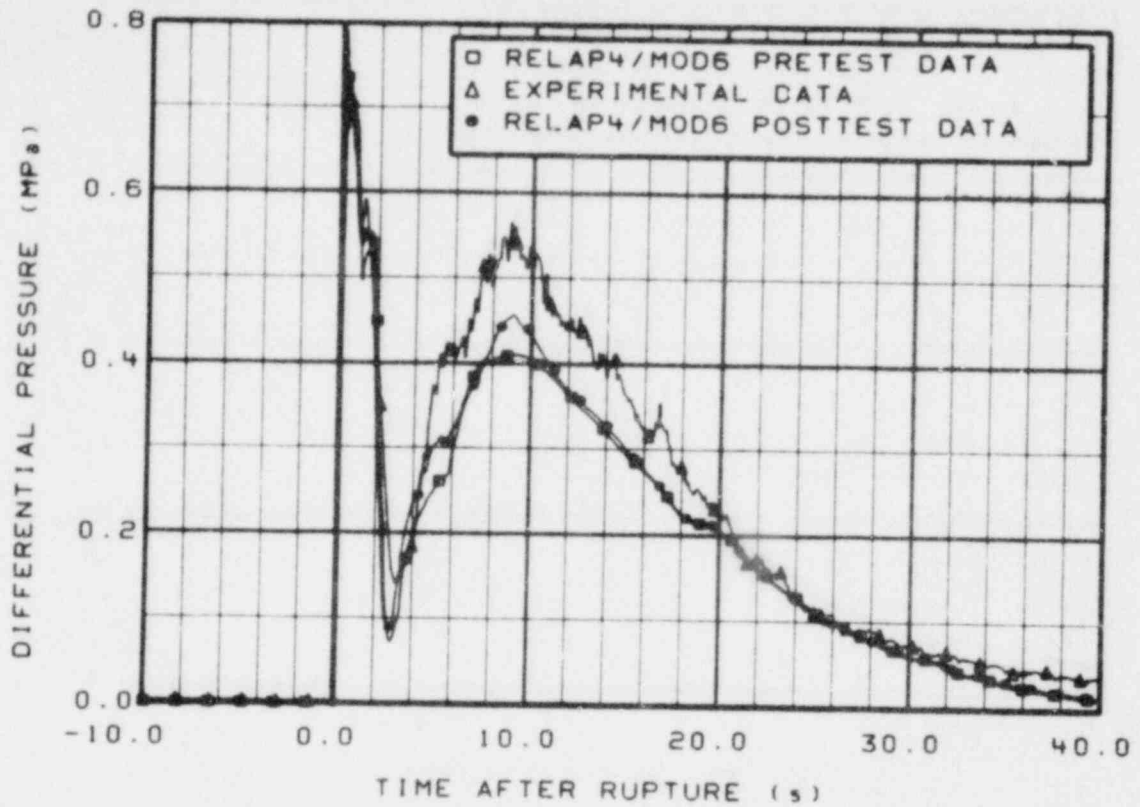


Figure A-7. Comparison of differential pressure across steam generator simulator for prediction, posttest, and experimental data.

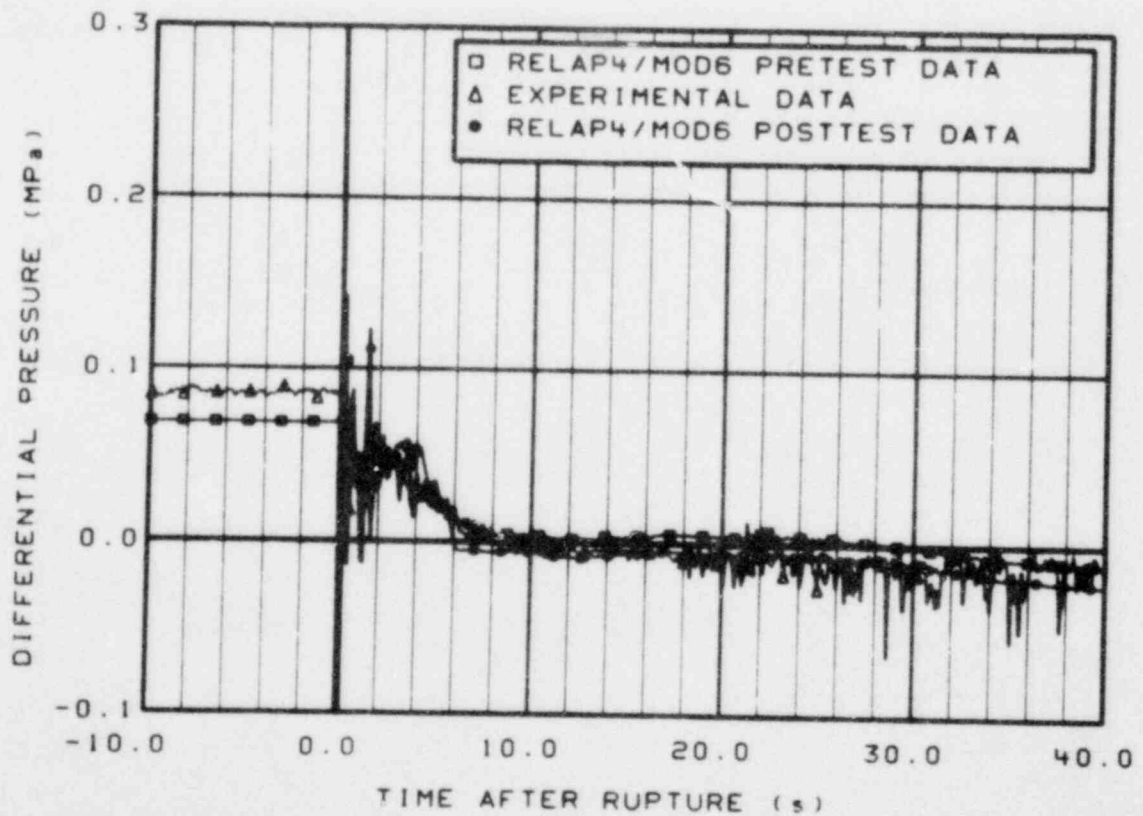


Figure A-8. Comparison of differential pressure across primary coolant pumps for prediction, posttest, and experimental data.

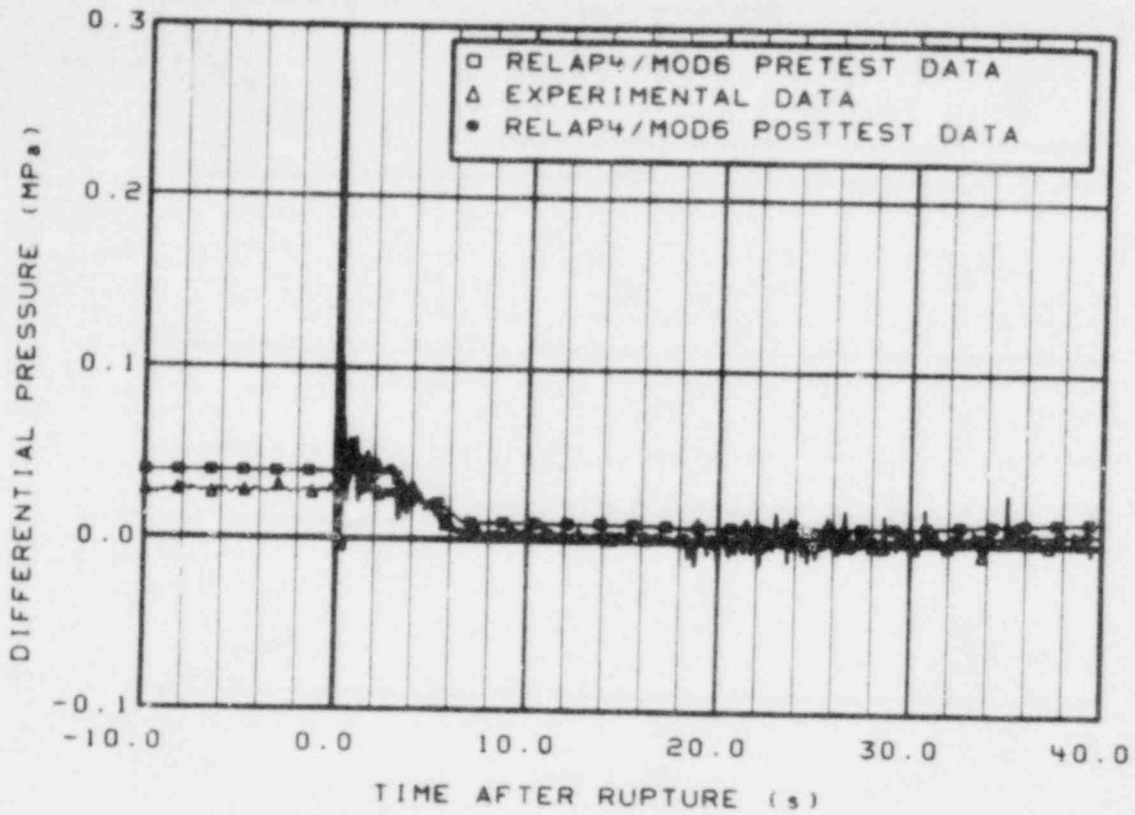


Figure A-9. Comparison of differential pressure across intact loop steam generator for prediction, posttest, and experimental data.

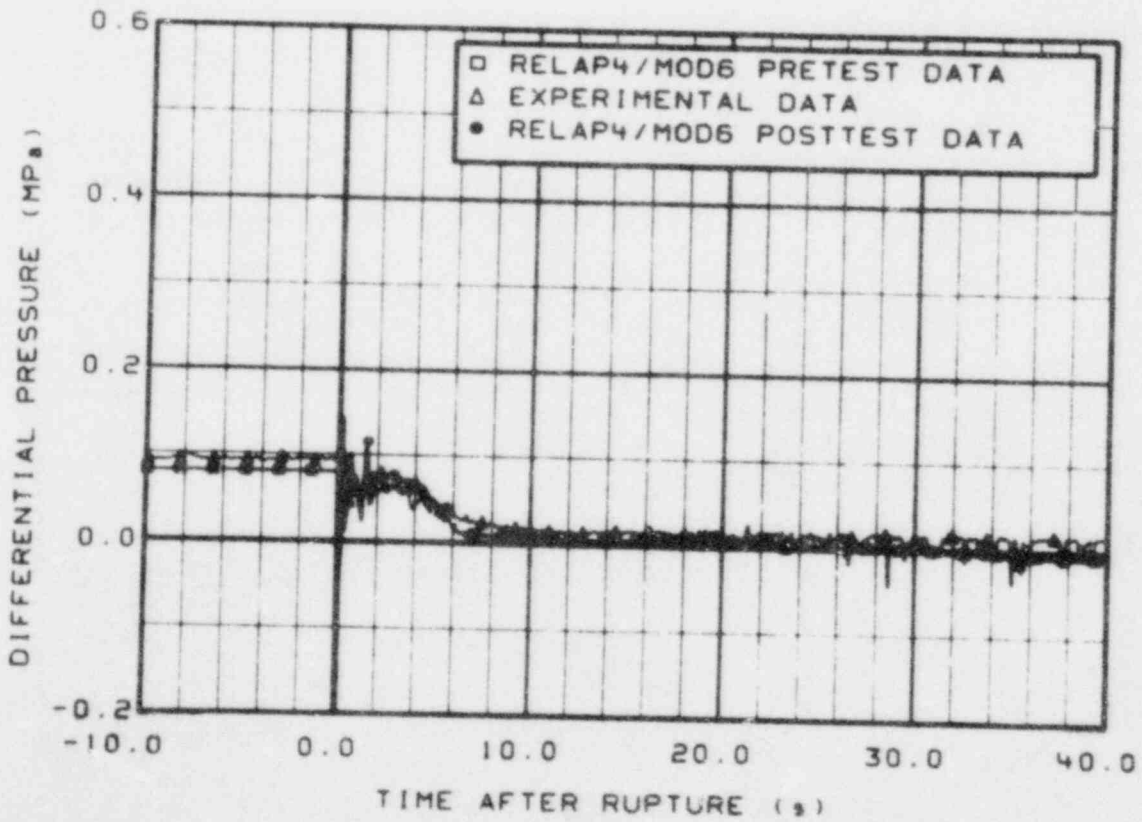


Figure A-10. Comparison of differential pressure across primary coolant Pump 1 for prediction, posttest, and experimental data.

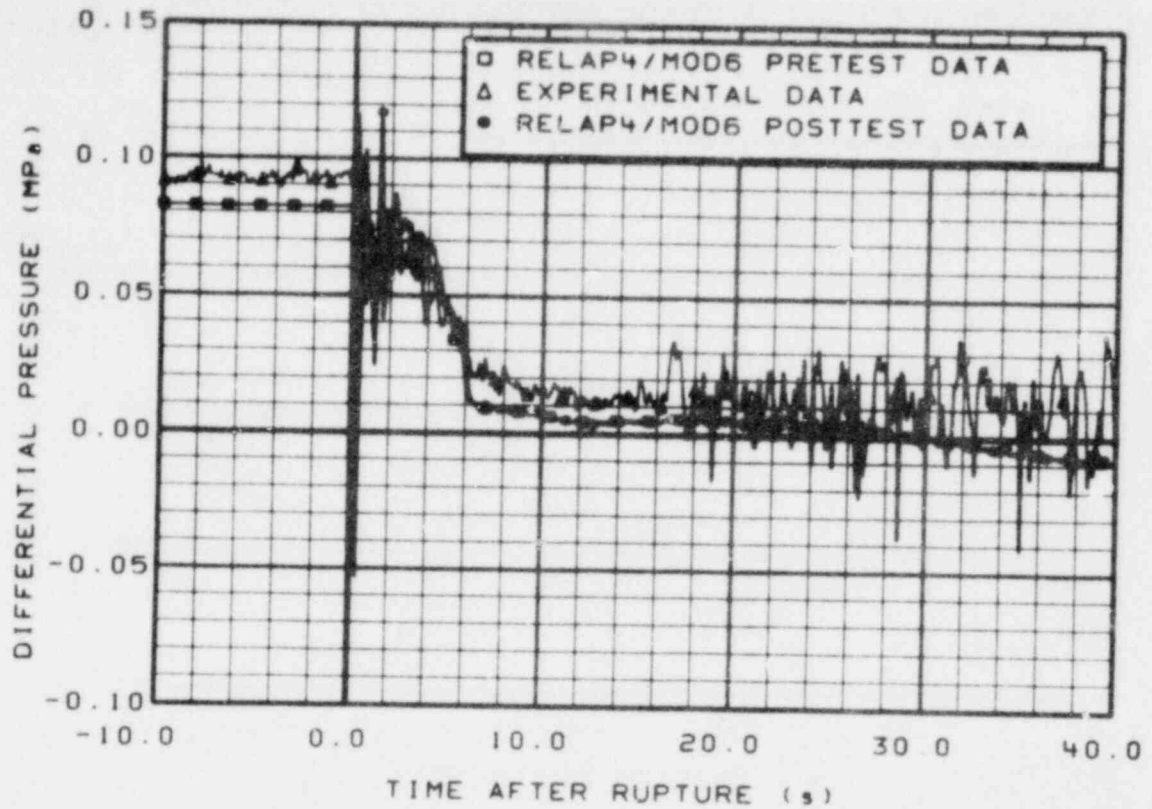


Figure A-11. Comparison of differential pressure across primary coolant Pump 2 for prediction, posttest, and experimental data.

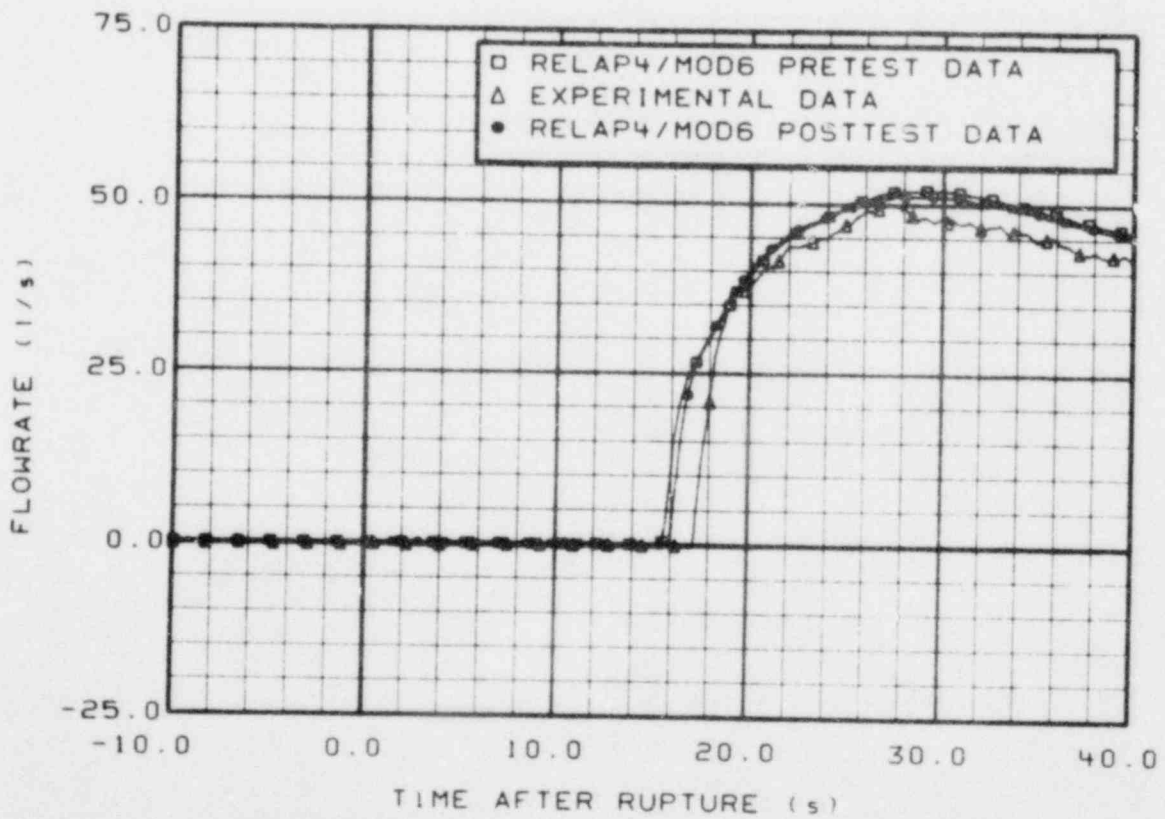


Figure A-12. Comparison of flow rate from accumulator for prediction, posttest, and experimental data.

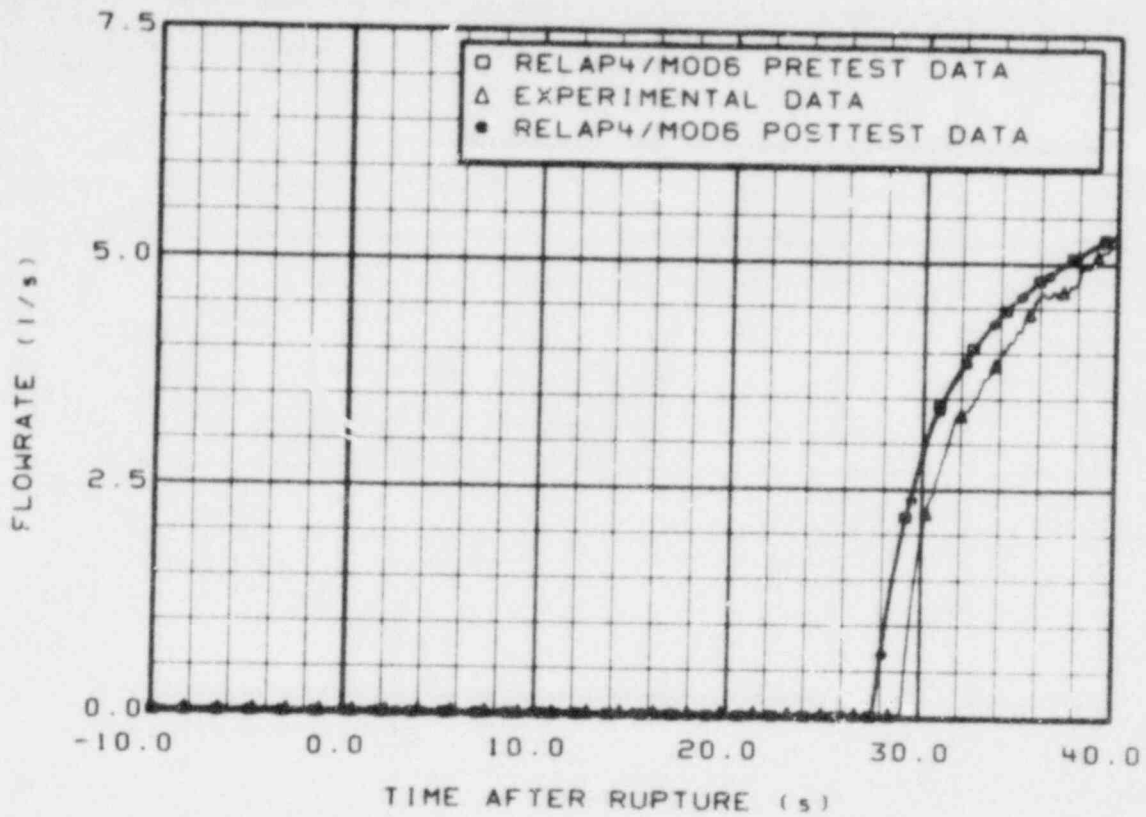


Figure A-13. Comparison of flow rate from low-pressure injection system pump for prediction, posttest, and experimental data.

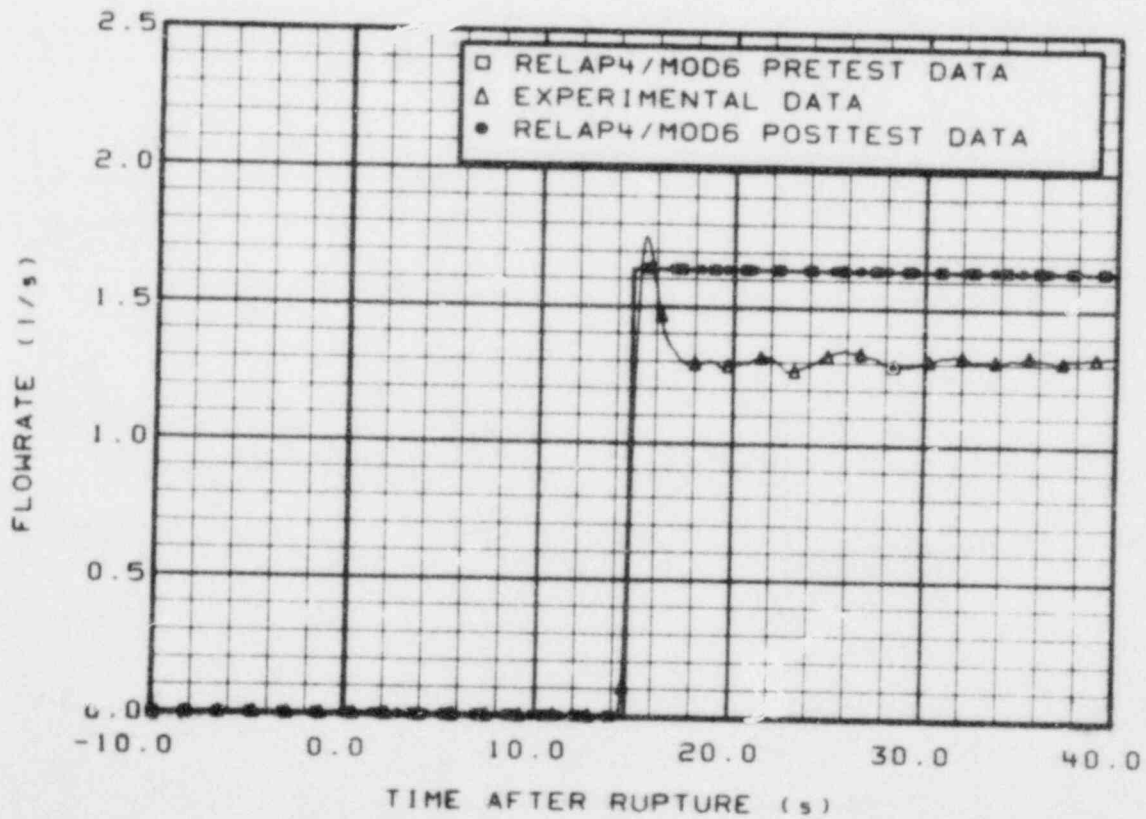


Figure A-14. Comparison of flow rate from high-pressure injection system pump for prediction, posttest, and experimental data.

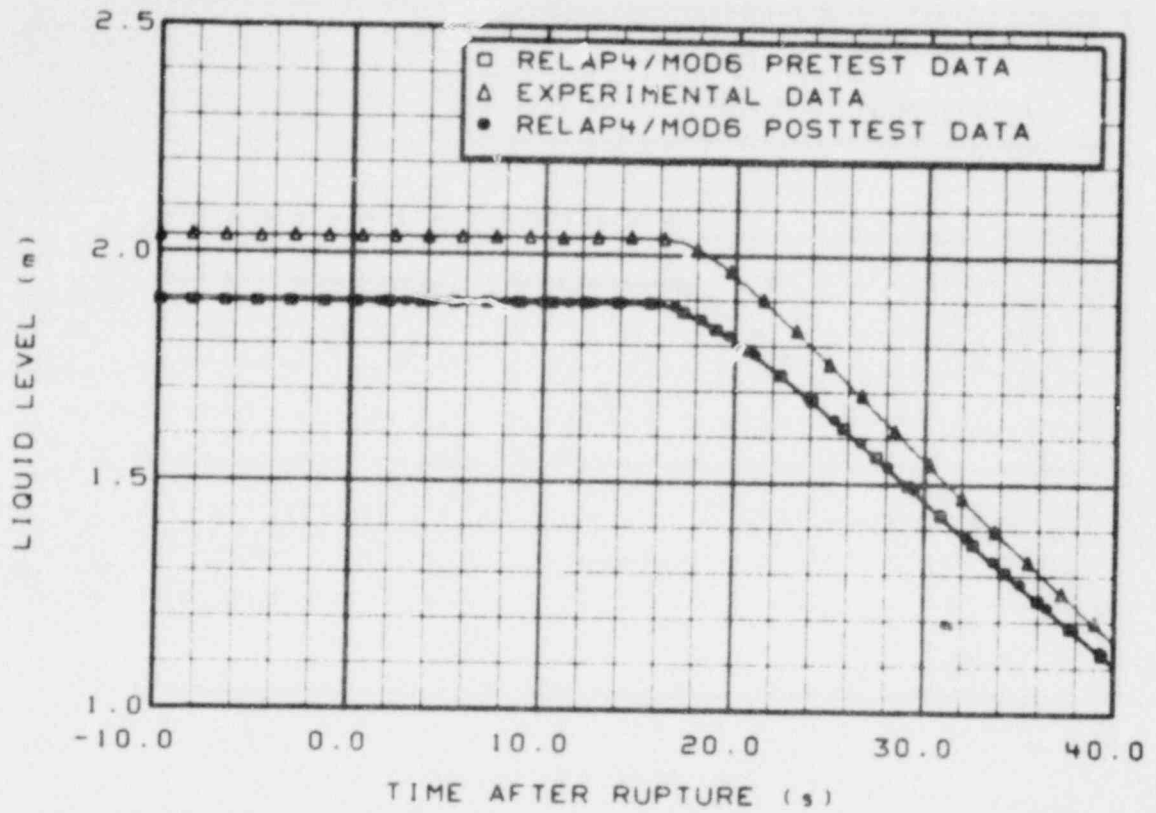


Figure A-15. Comparison of liquid level in accumulator for prediction, posttest, and experimental data.

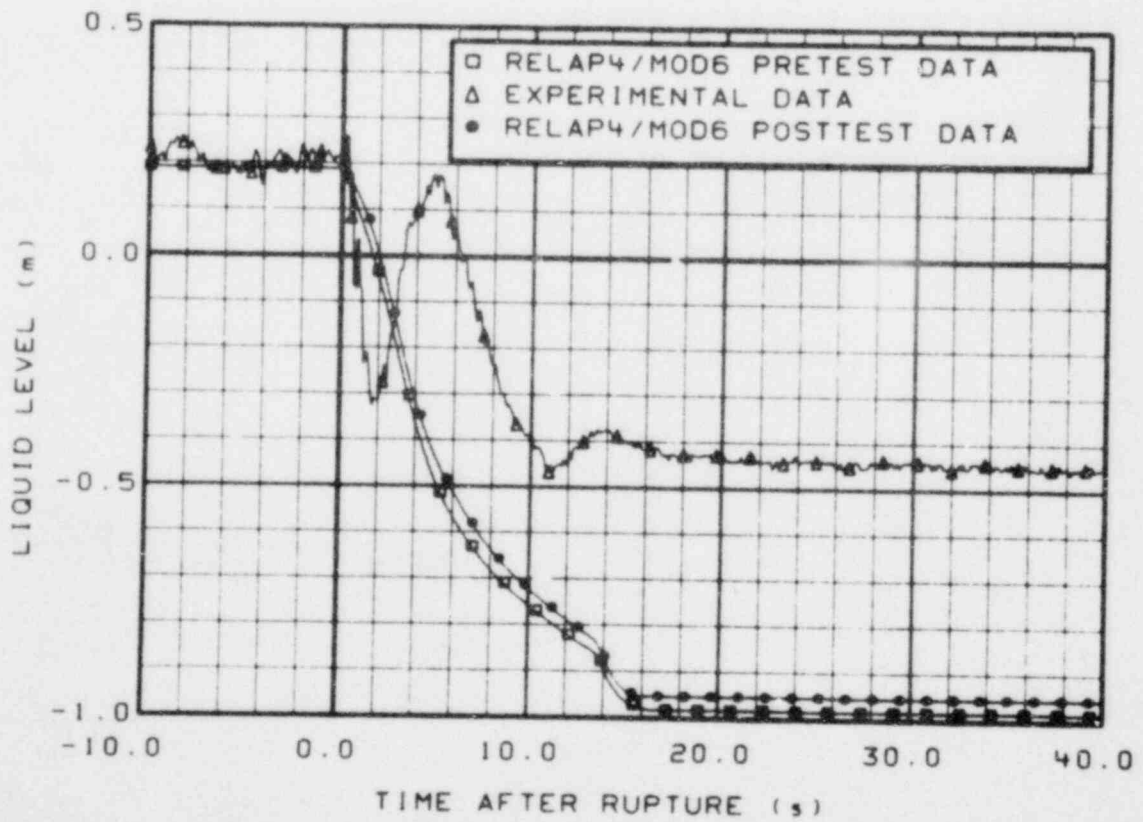


Figure A-16. Comparison of liquid level in steam generator secondary side for prediction, posttest, and experimental data.

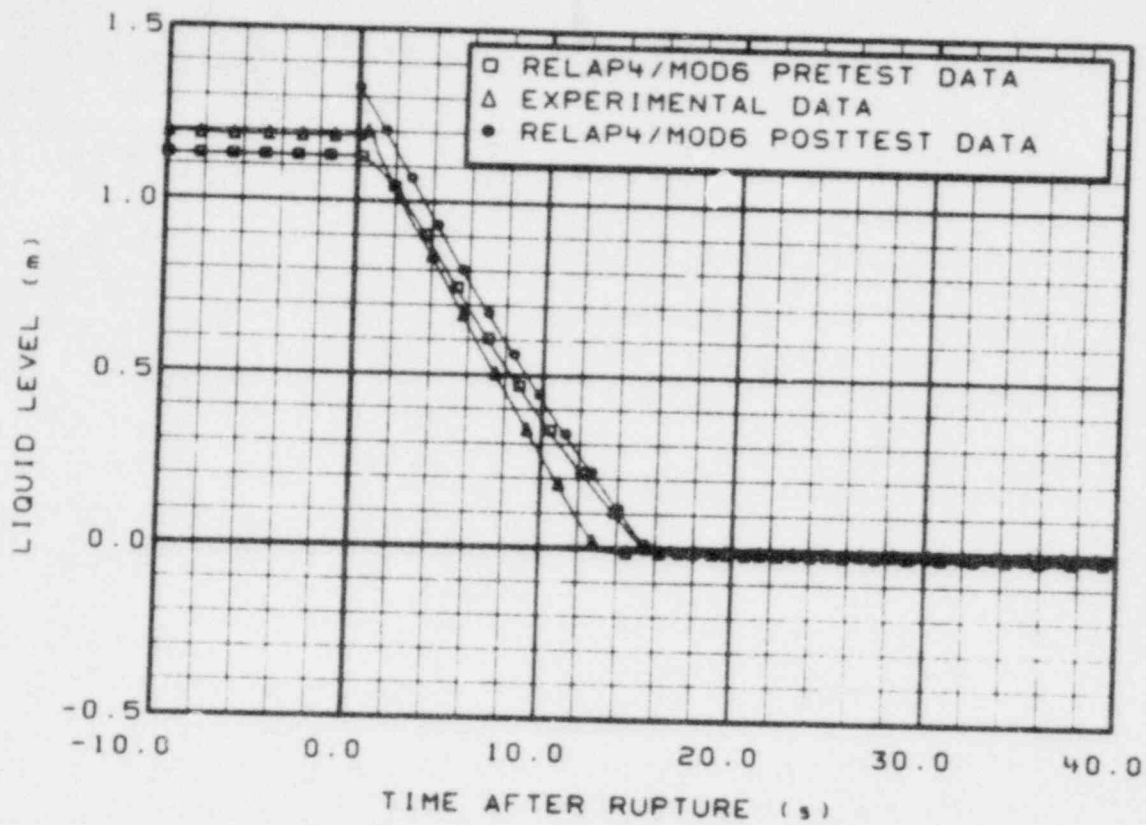


Figure A-17. Comparison of liquid level in pressurizer for prediction, posttest, and experimental data.

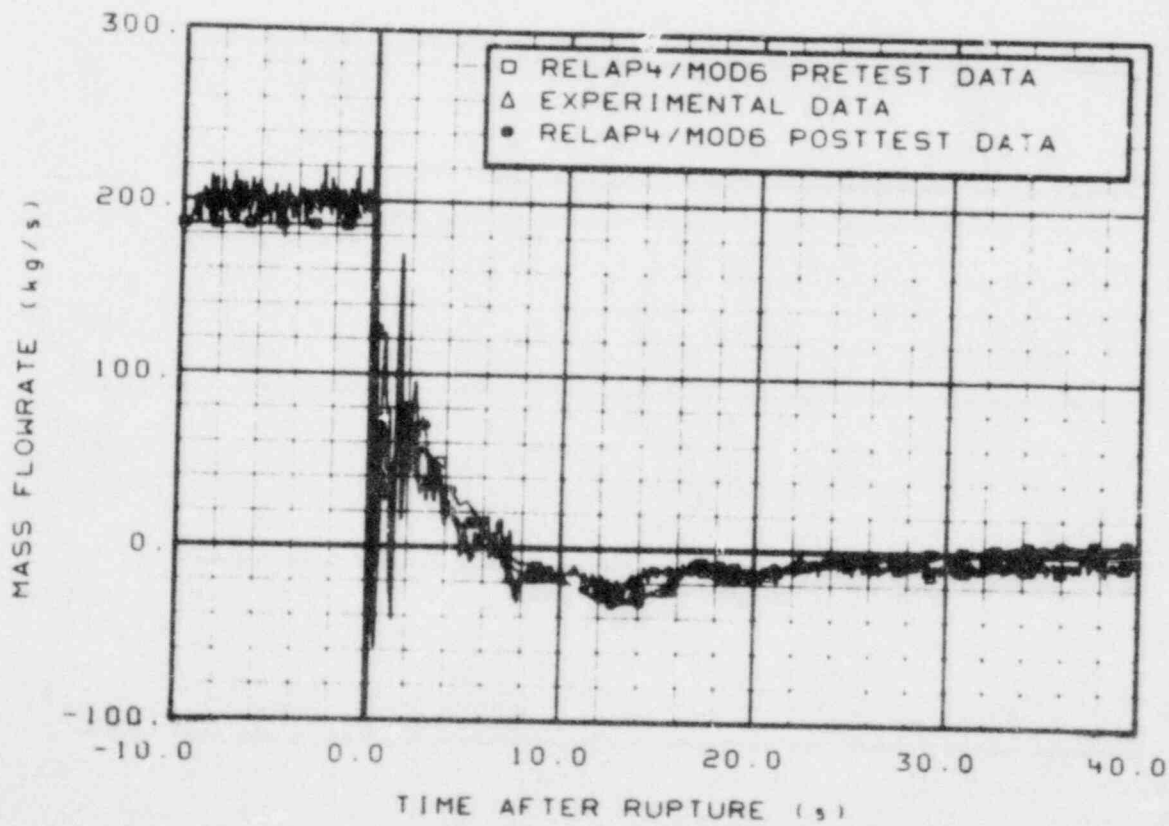


Figure A-18. Comparison of mass flow in intact loop hot leg for prediction, posttest, and experimental data.

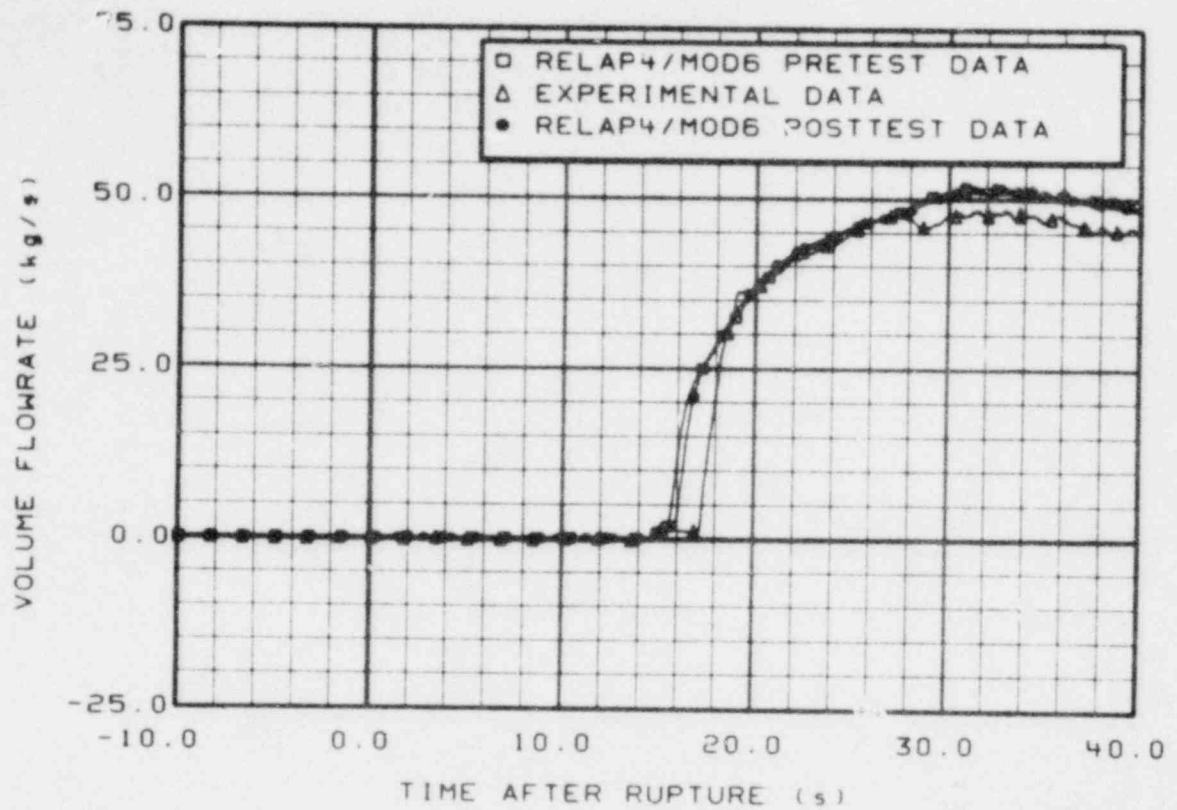


Figure A-19. Comparison of total emergency core coolant flow rate for prediction, posttest, and experimental data.

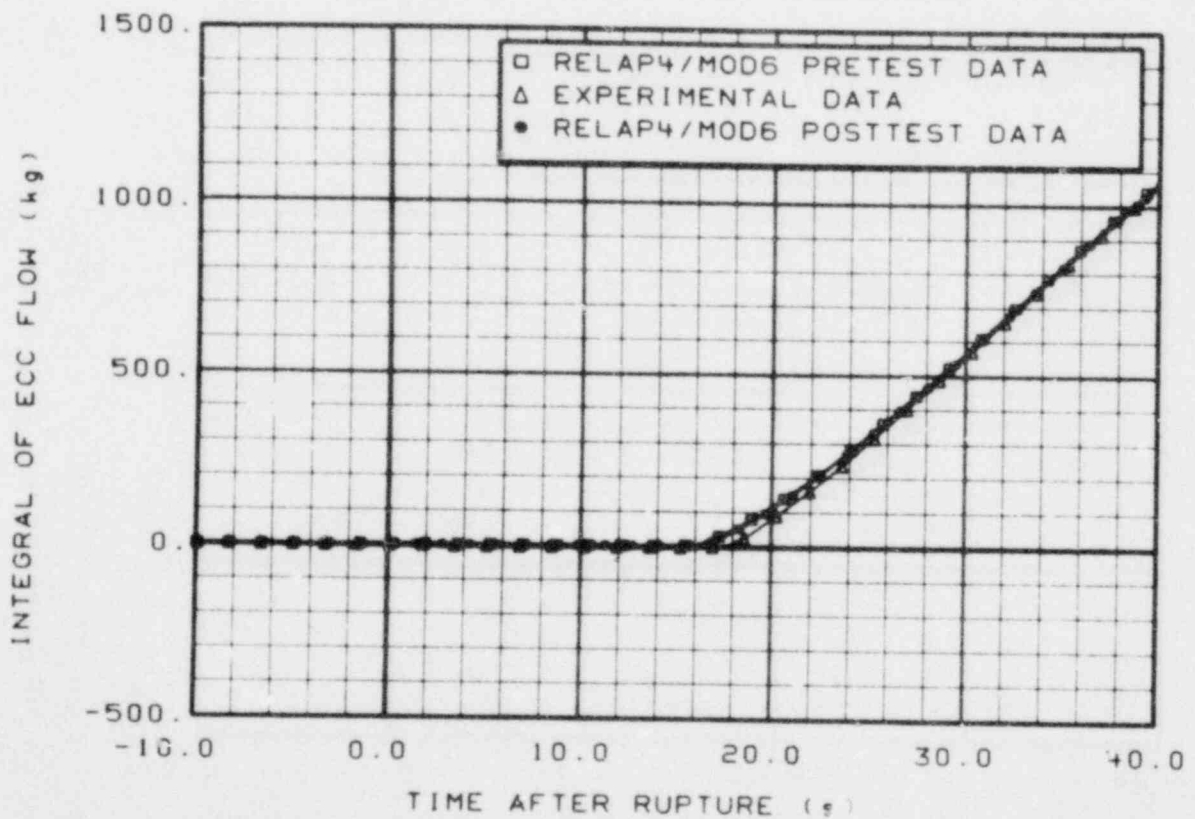


Figure A-20. Comparison of integral of emergency core coolant flow for prediction, posttest, and experimental data.

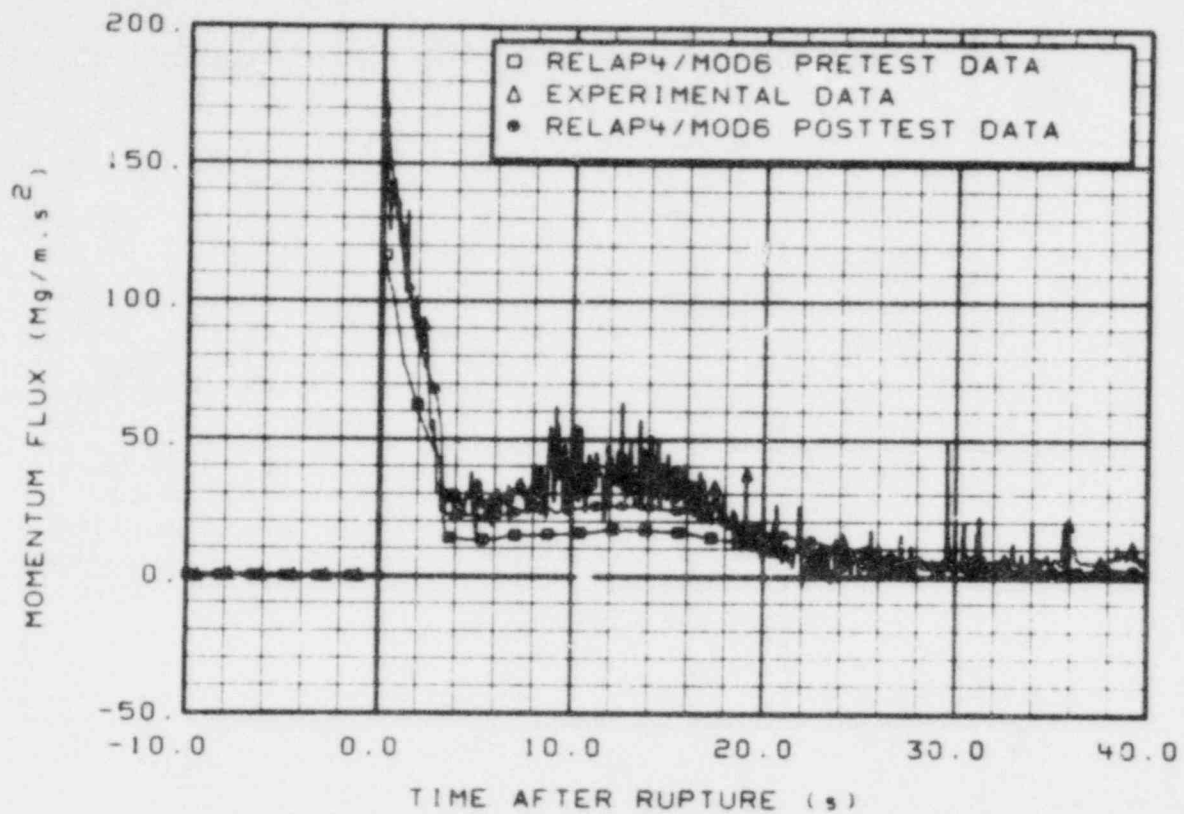


Figure A-21. Comparison of momentum flux in broken loop cold leg for prediction, posttest, and experimental data.

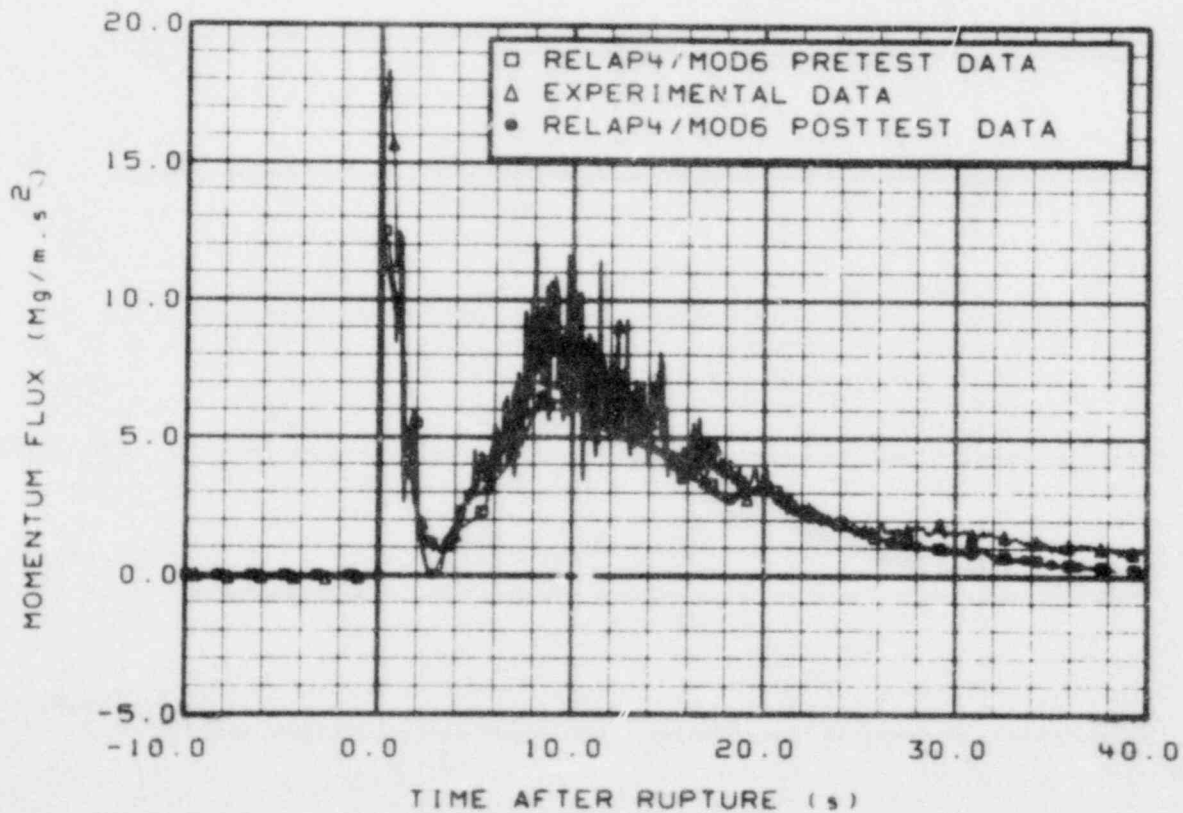


Figure A-22. Comparison of momentum flux in broken loop hot leg for prediction, posttest, and experimental data.

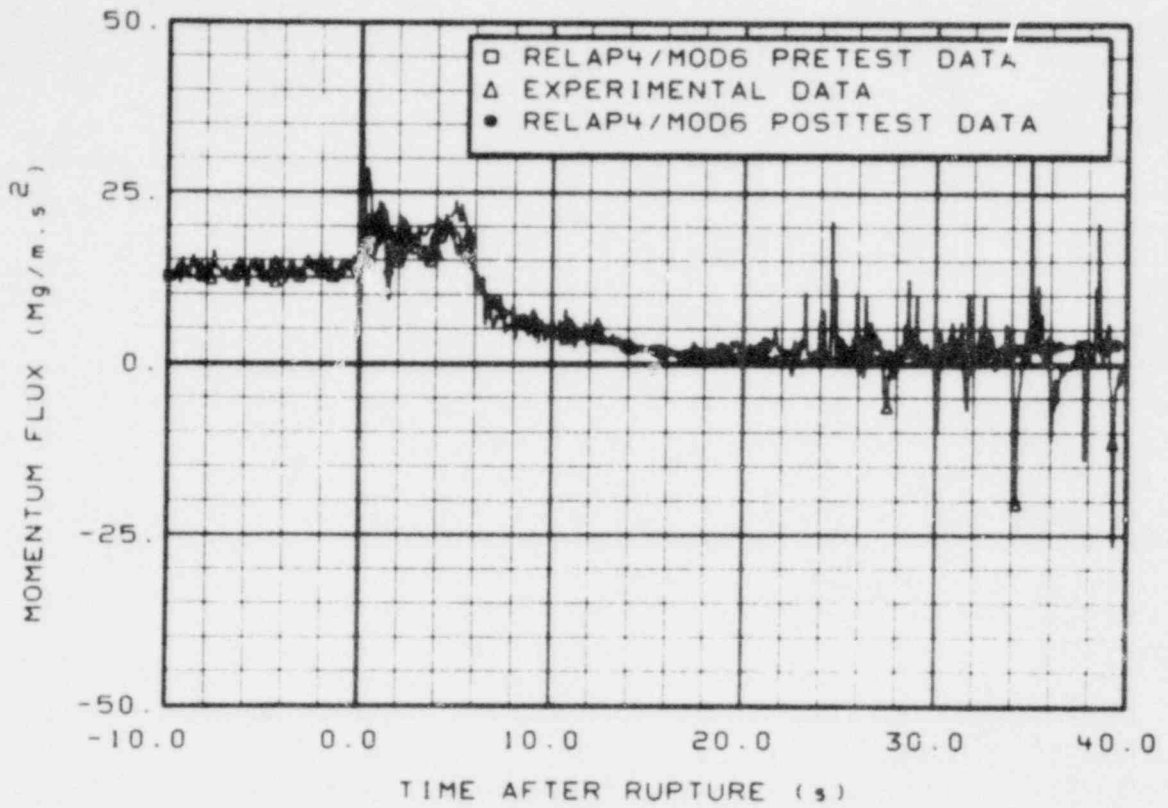


Figure A-23. Comparison of momentum flux in intact loop cold leg for prediction, posttest, and experimental data.

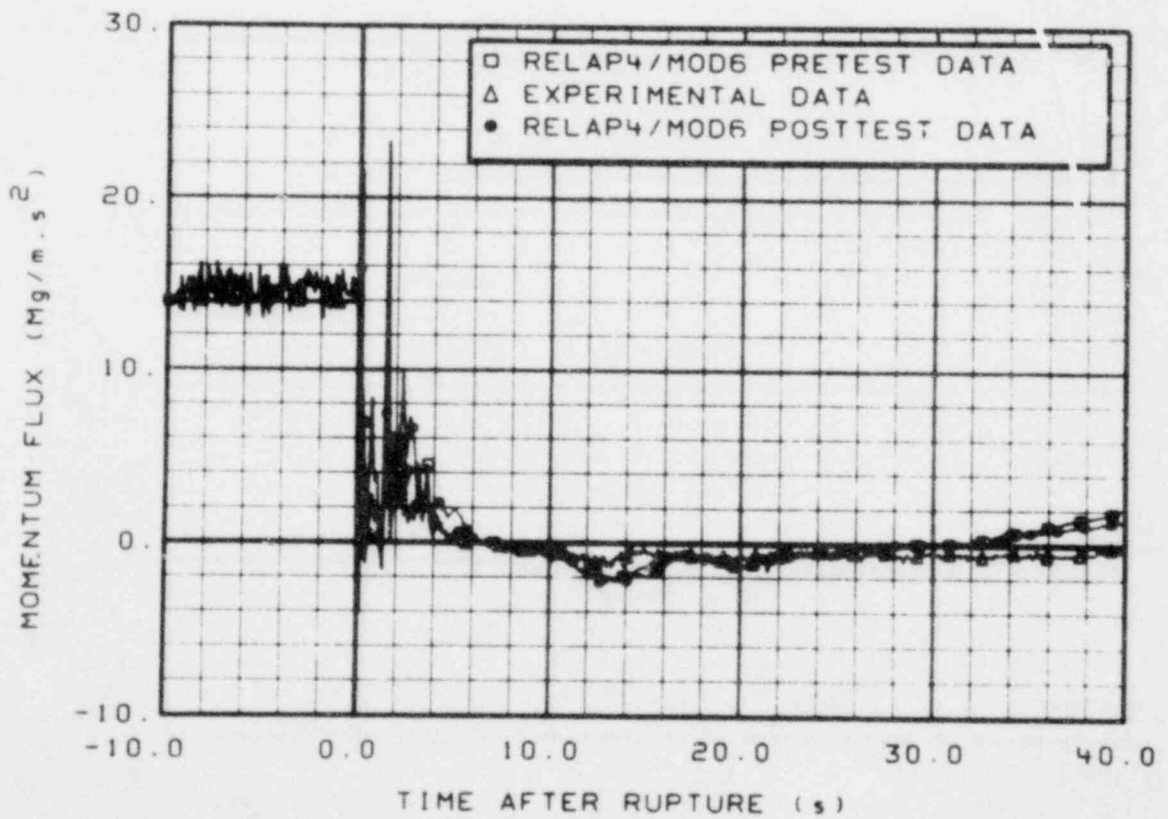


Figure A-24. Comparison of momentum flux in intact loop hot leg for prediction, posttest, and experimental data.

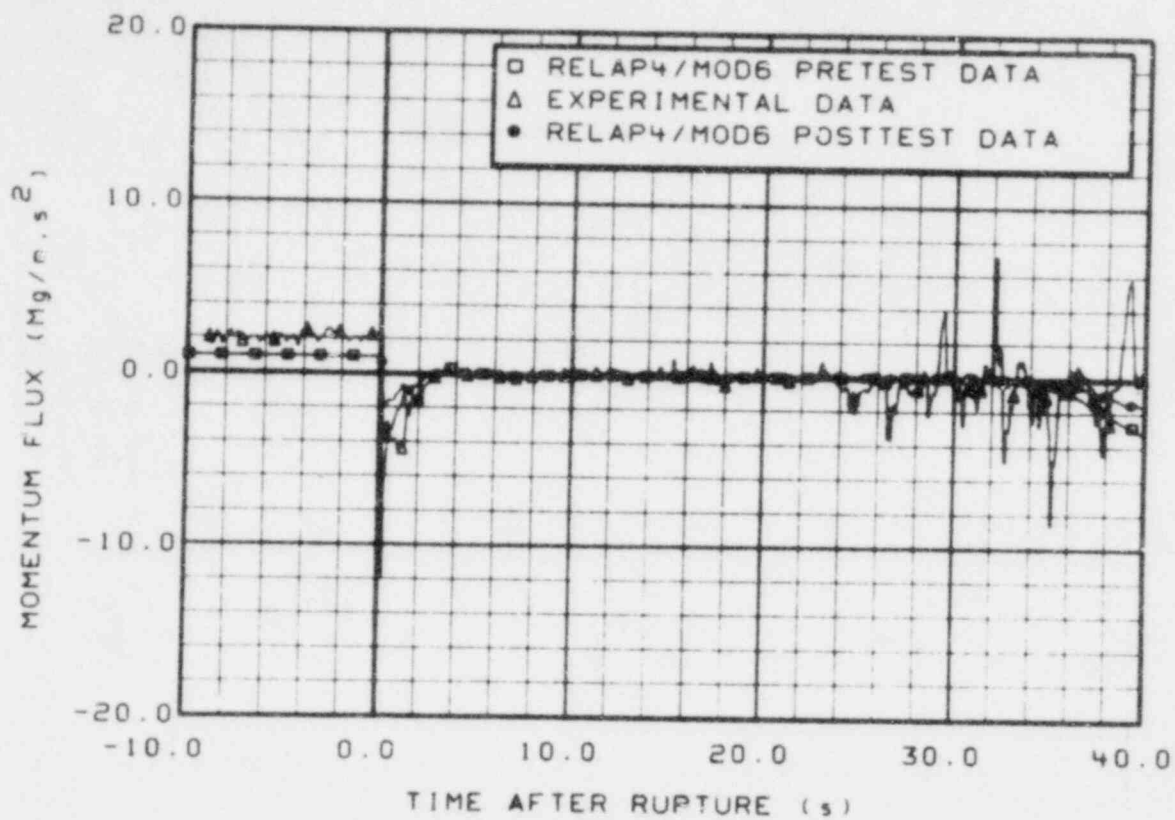


Figure A-25. Comparison of momentum flux at instrument Stalk 1 for prediction, posttest, and experimental data.

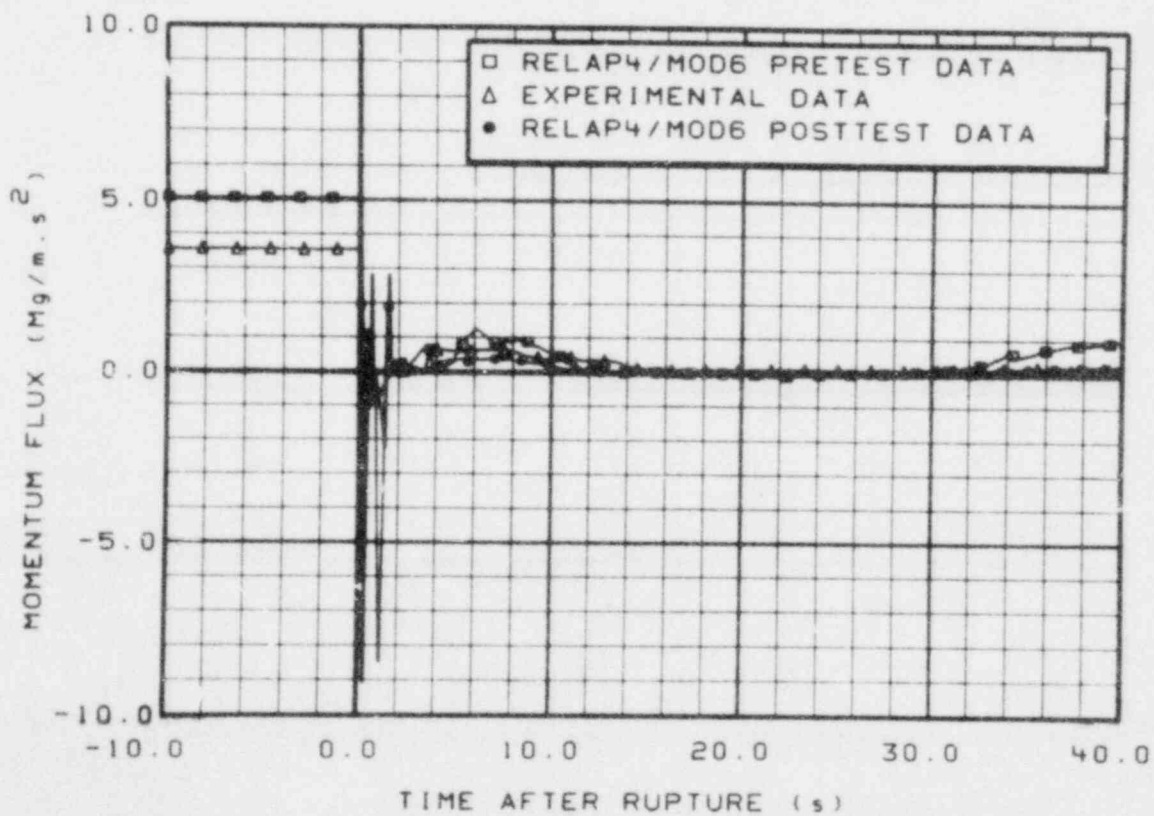


Figure A-26. Comparison of momentum flux in upper end box for prediction, posttest, and experimental data.

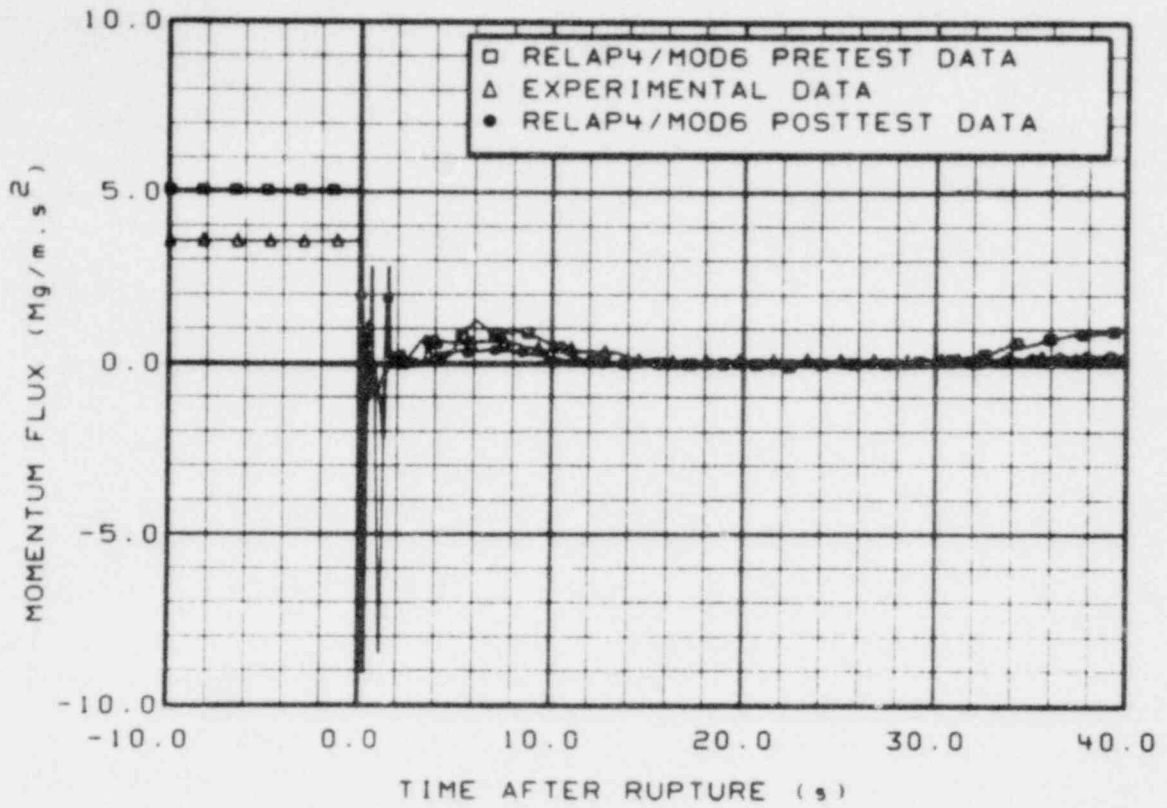


Figure A-27. Comparison of momentum flux in upper end box for prediction, posttest, and experimental data.

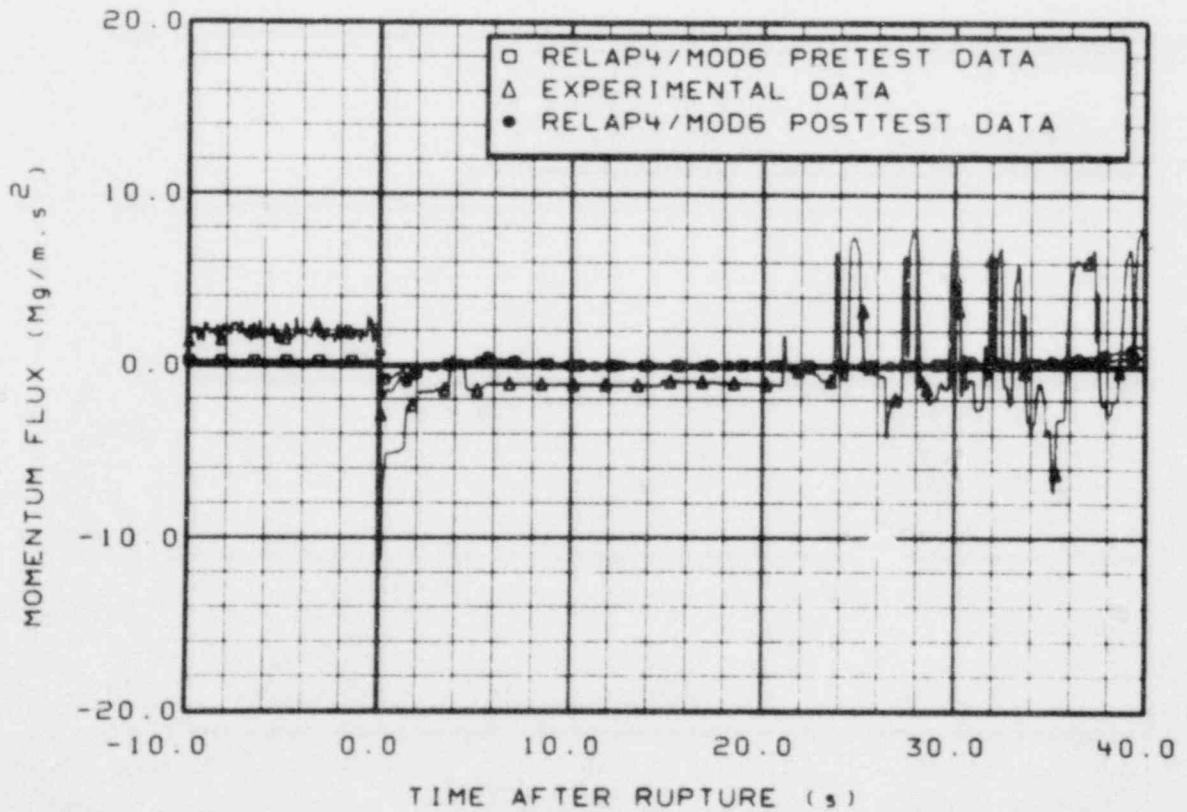


Figure A-28. Comparison of momentum flux at instrument Stalk 2 for prediction, posttest, and experimental data.

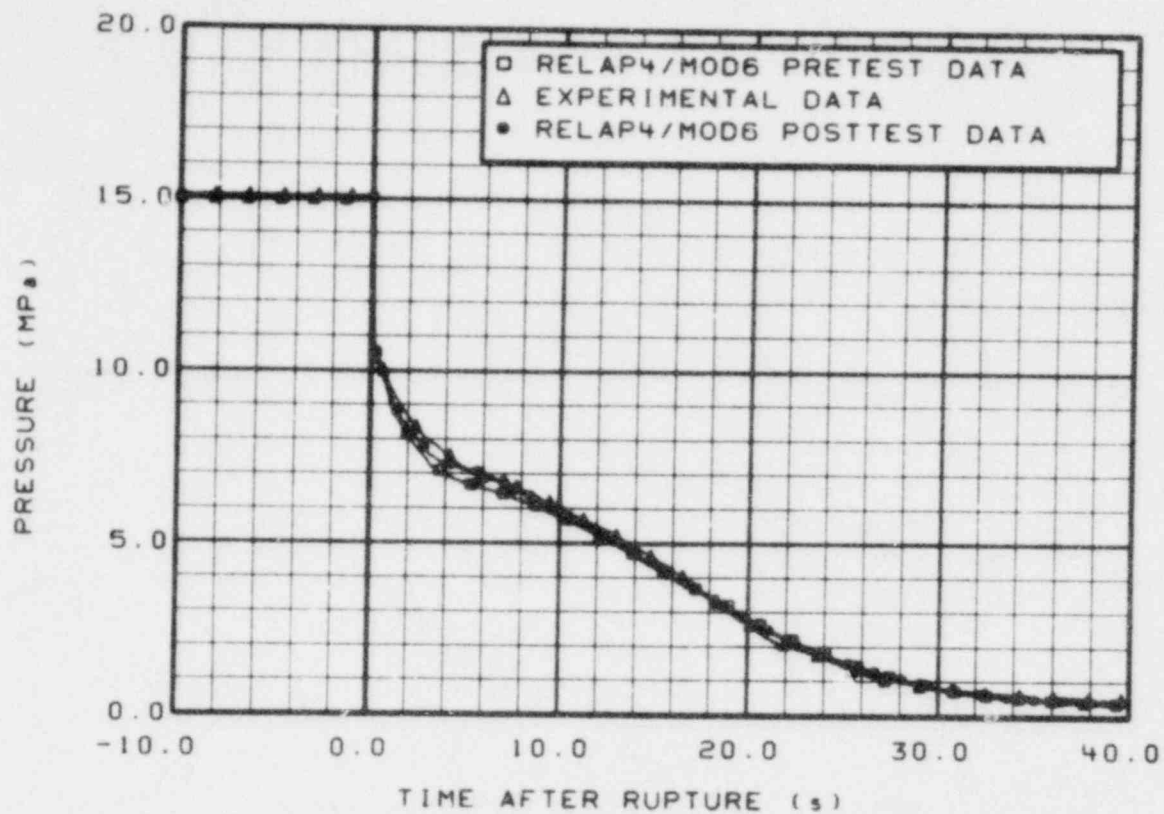


Figure A-29. Comparison of pressure in broken loop cold leg for prediction, posttest, and experimental data.

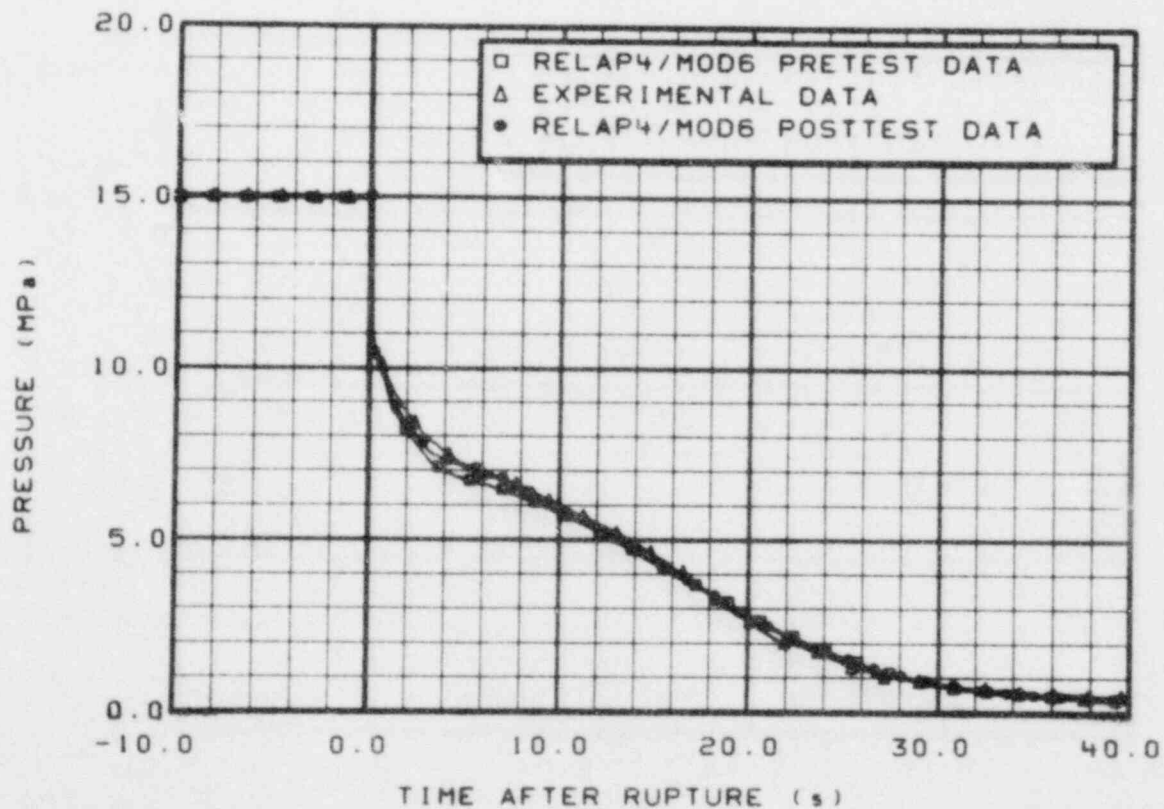


Figure A-30. Comparison of pressure in broken loop hot leg for prediction, posttest, and experimental data.

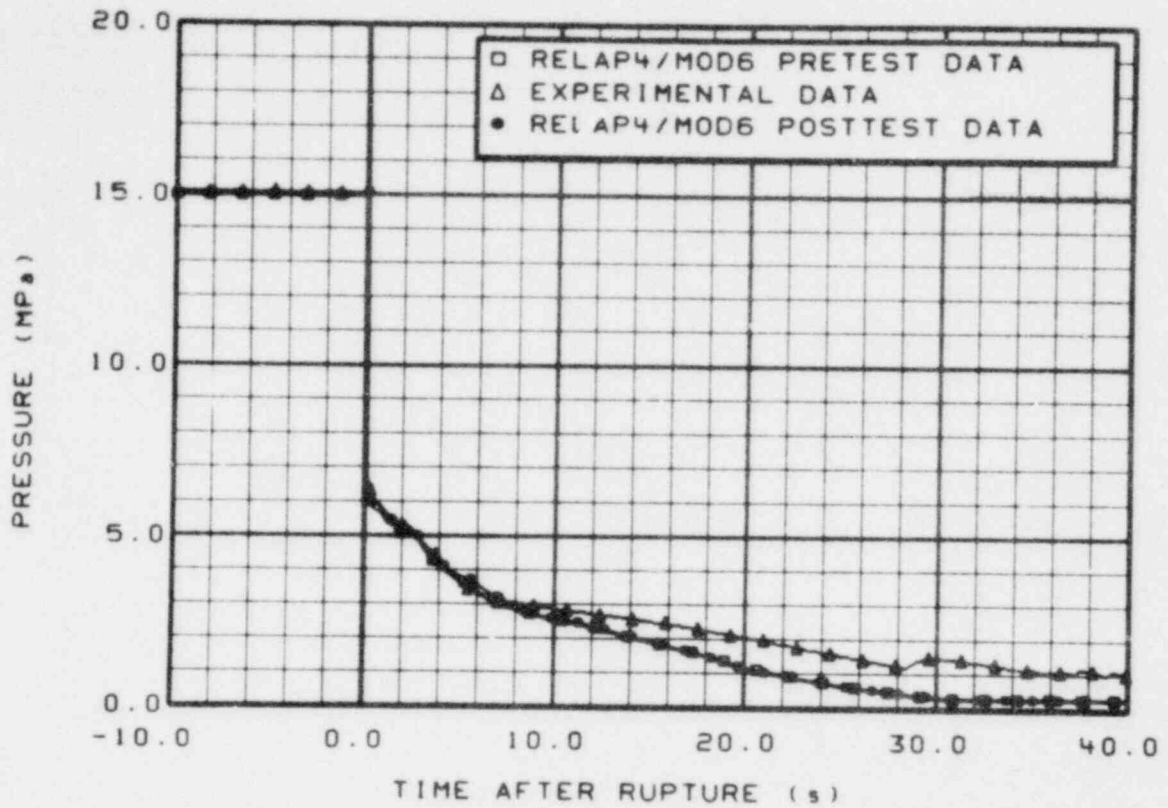


Figure A-31. Comparison of pressure in broken loop hot leg pump simulator outlet for prediction, posttest, and experimental data.

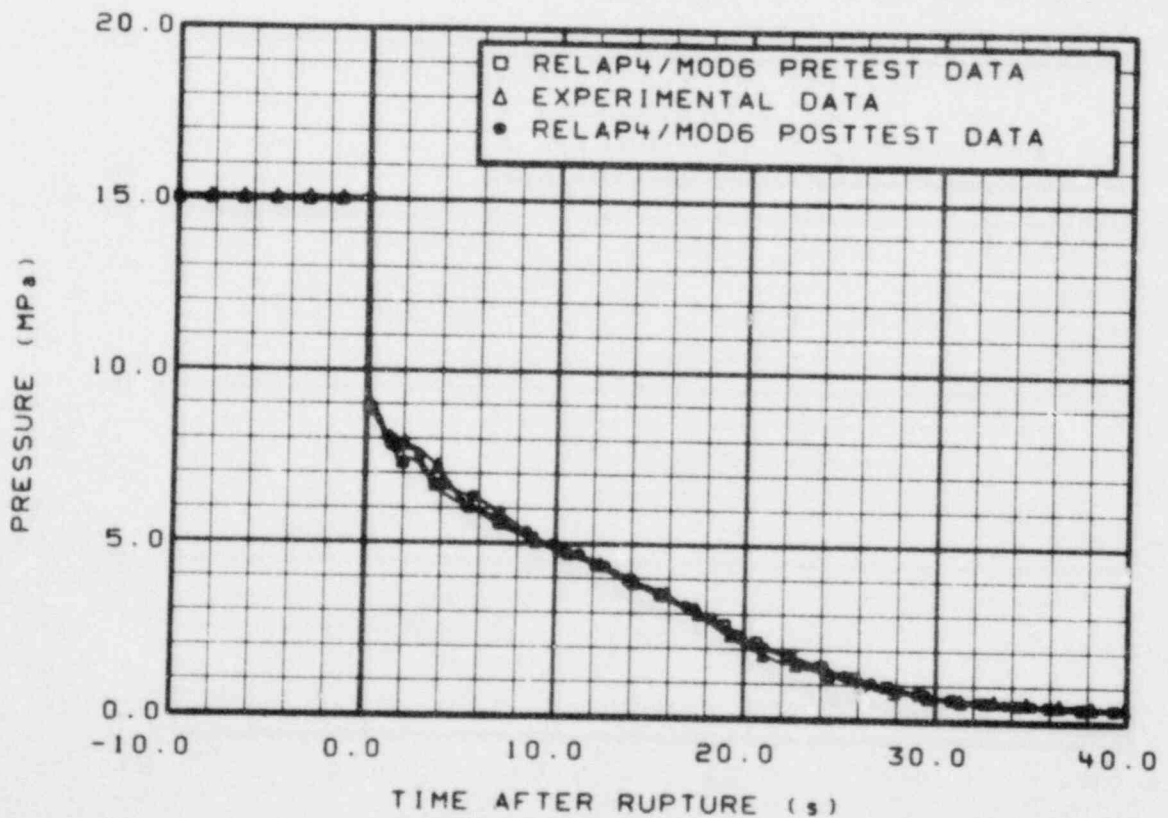


Figure A-32. Comparison of pressure in steam generator simulator outlet for prediction, posttest, and experimental data.

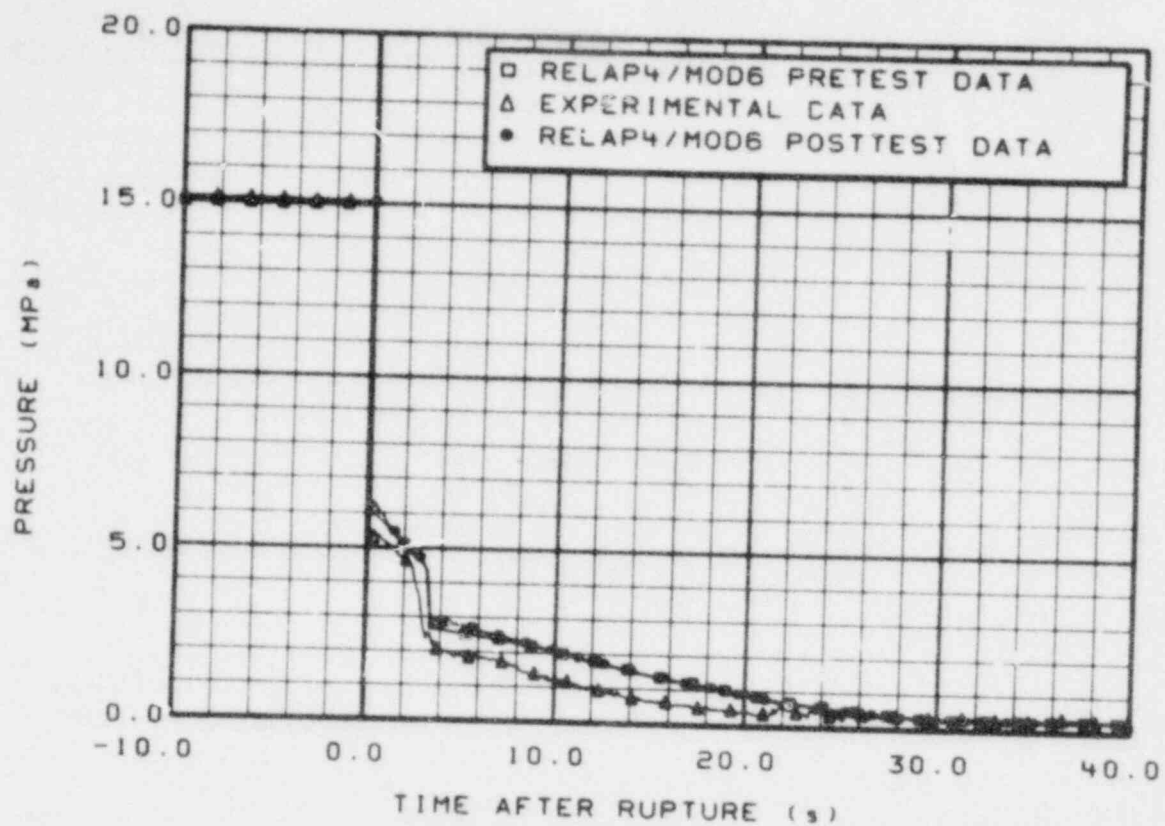


Figure A-33. Comparison of pressure in broken loop cold leg spool piece midpoint for prediction, posttest, and experimental data.

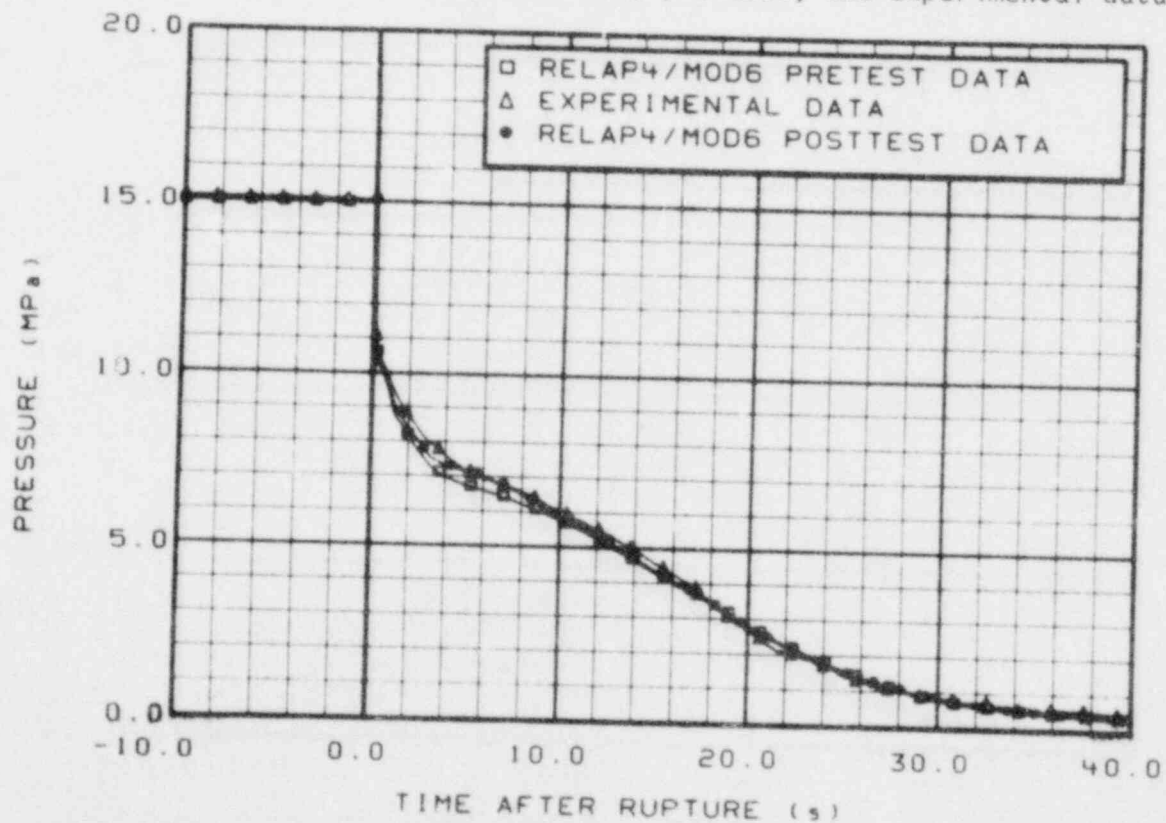


Figure A-34. Comparison of pressure in intact loop cold leg for prediction, posttest, and experimental data.

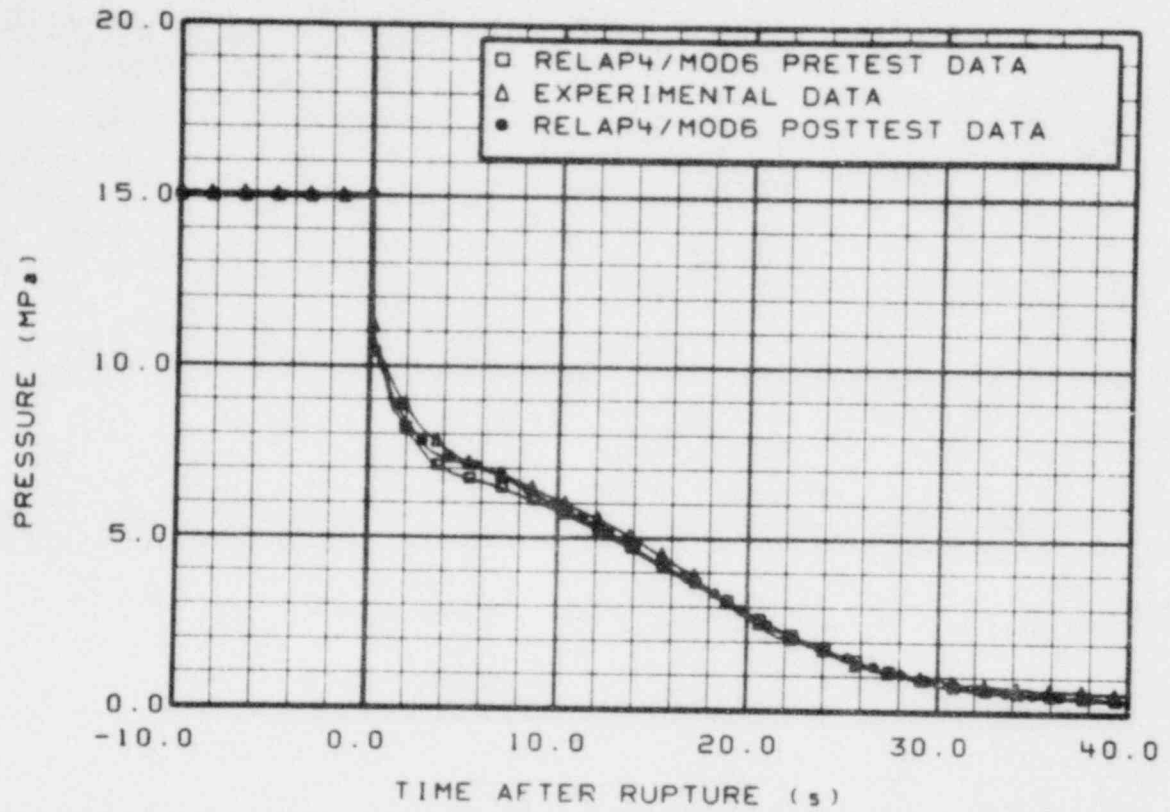


Figure A-35. Comparison of pressure in intact loop hot leg for prediction, posttest, and experimental data.

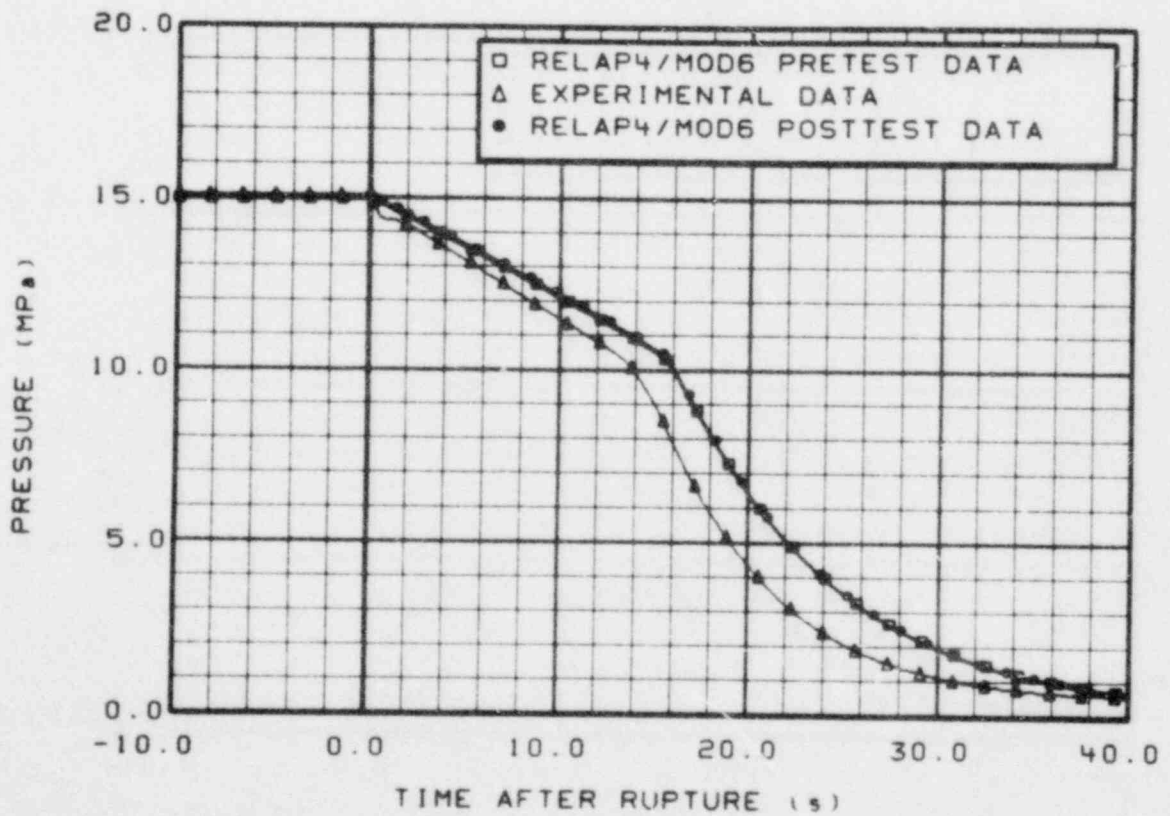


Figure A-36. Comparison of pressure in intact loop pressurizer for prediction, posttest, and experimental data.

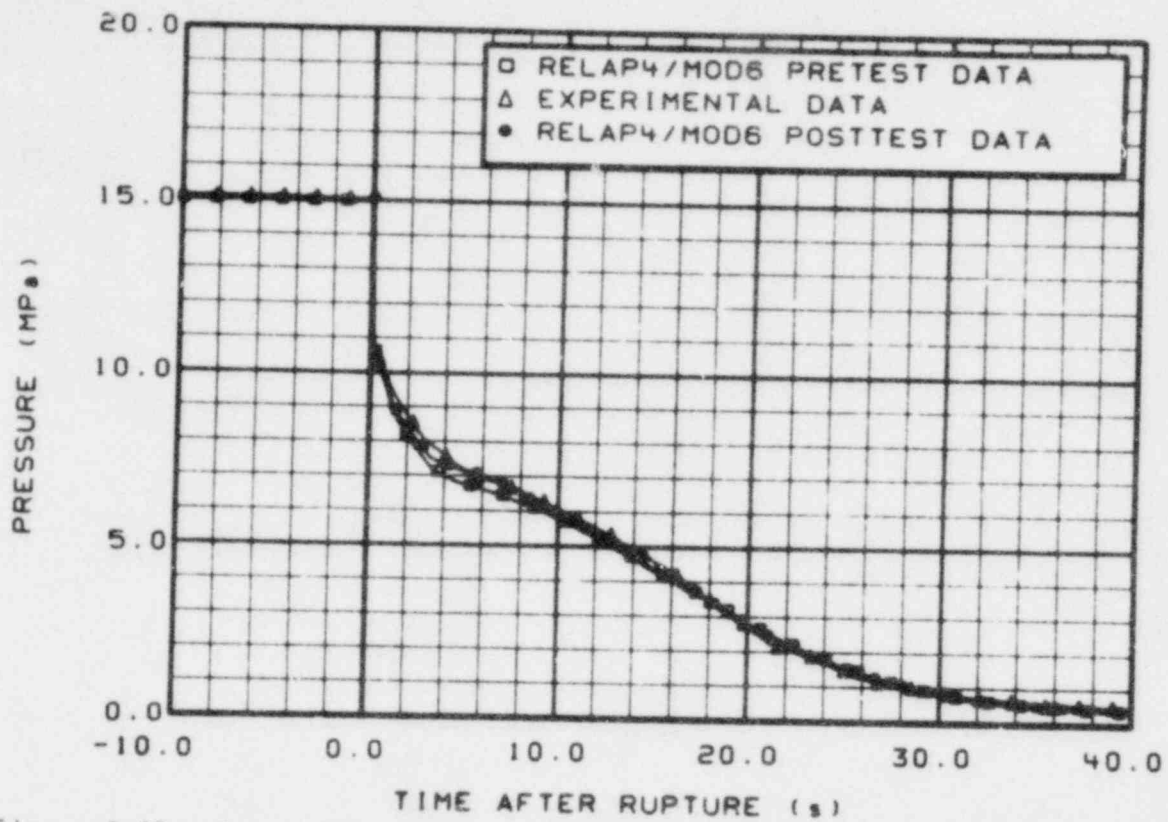


Figure A-37. Comparison of pressure at instrument Stalk 1 at 0.631 m above reactor vessel bottom for prediction, posttest, and experimental data.

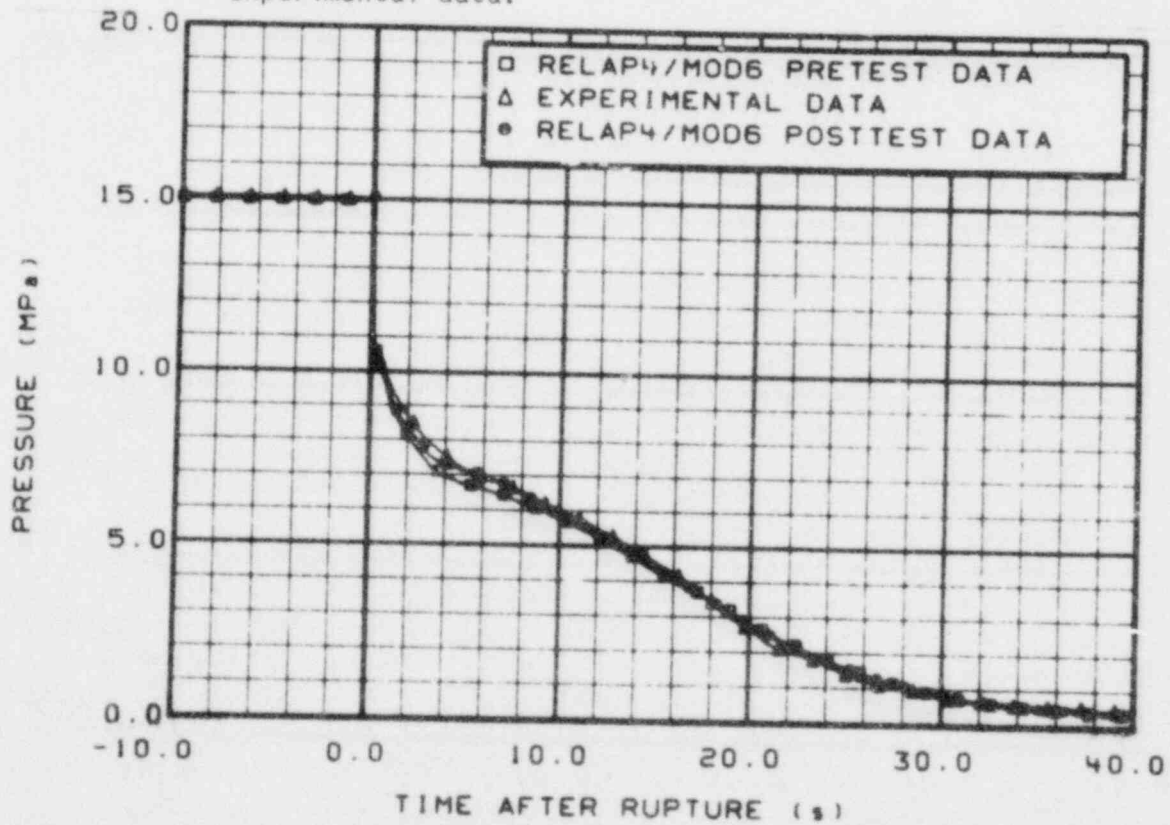


Figure A-38. Comparison of pressure at instrument Stalk 1 at 5.319 m above reactor vessel bottom for prediction, posttest, and experimental data.

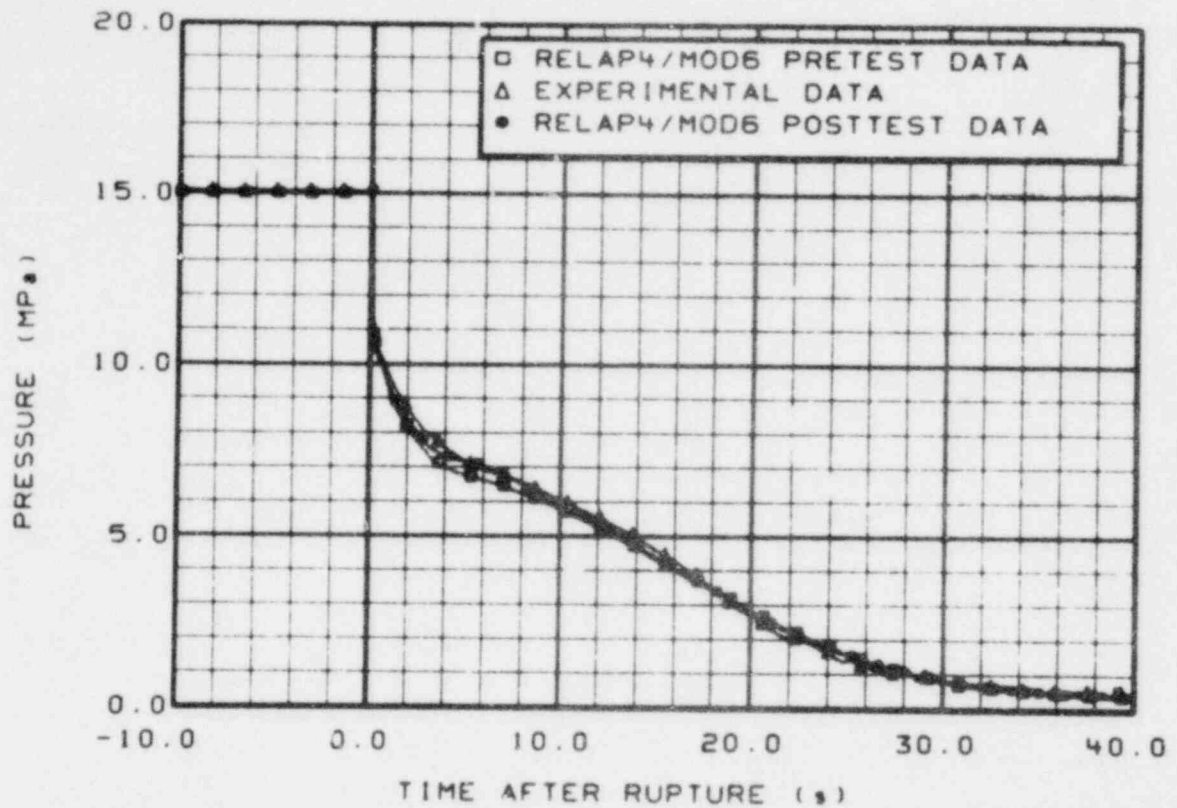


Figure A-39. Comparison of pressure at instrument Stalk 2 at 0.631 m above reactor vessel bottom for prediction, posttest, and experimental data.

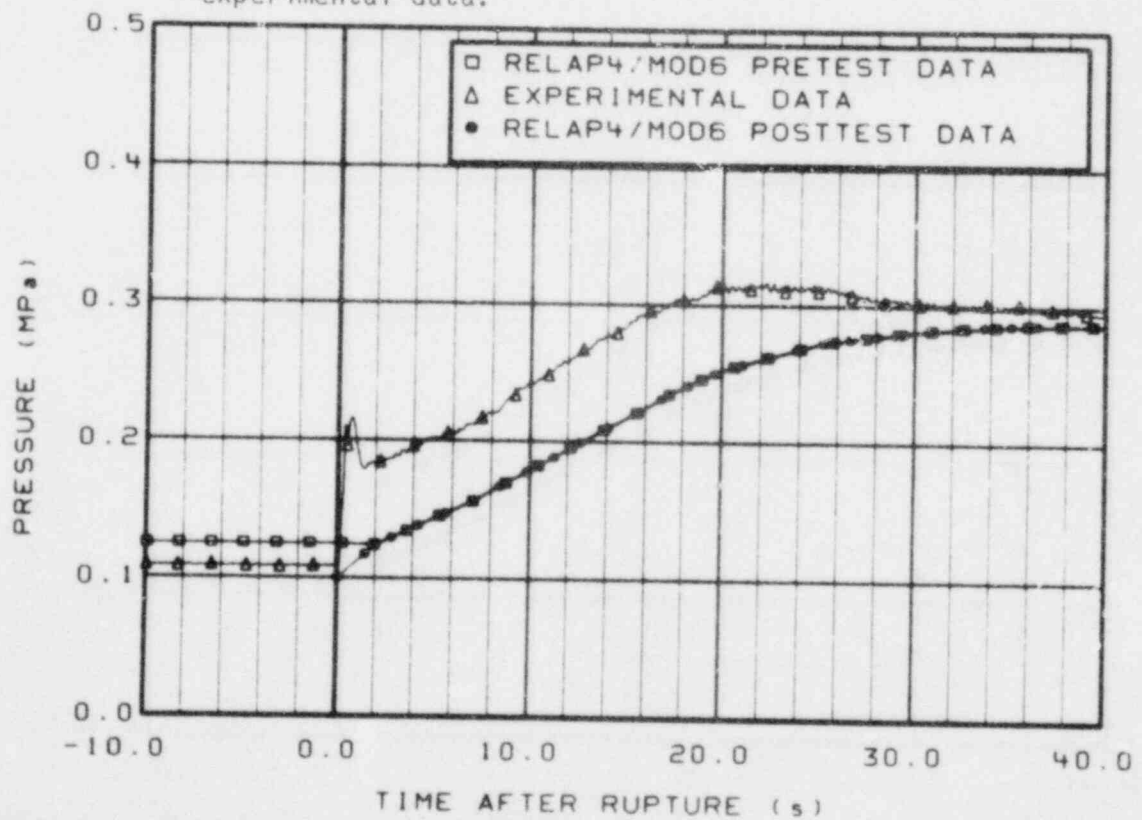


Figure A-40. Comparison of pressure in blowdown suppression tank for prediction, posttest, and experimental data.

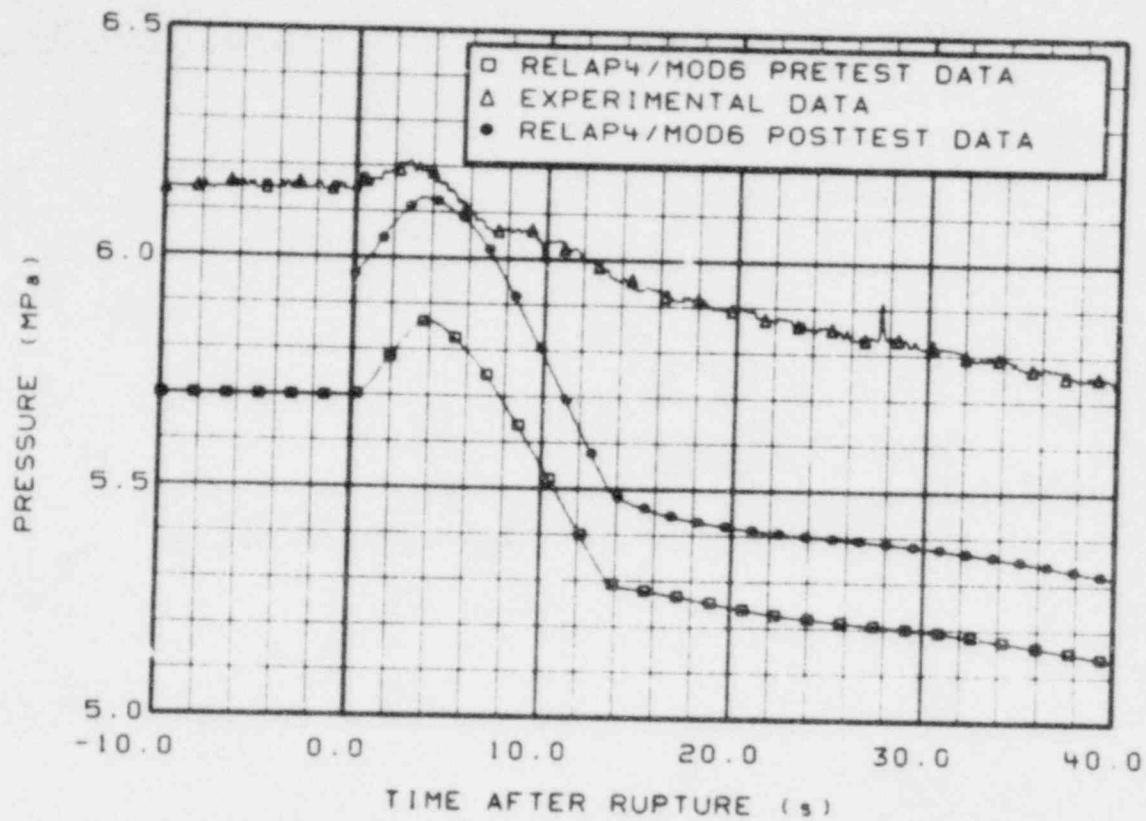


Figure A-41. Comparison of pressure in steam generator secondary side for prediction, posttest, and experimental data.

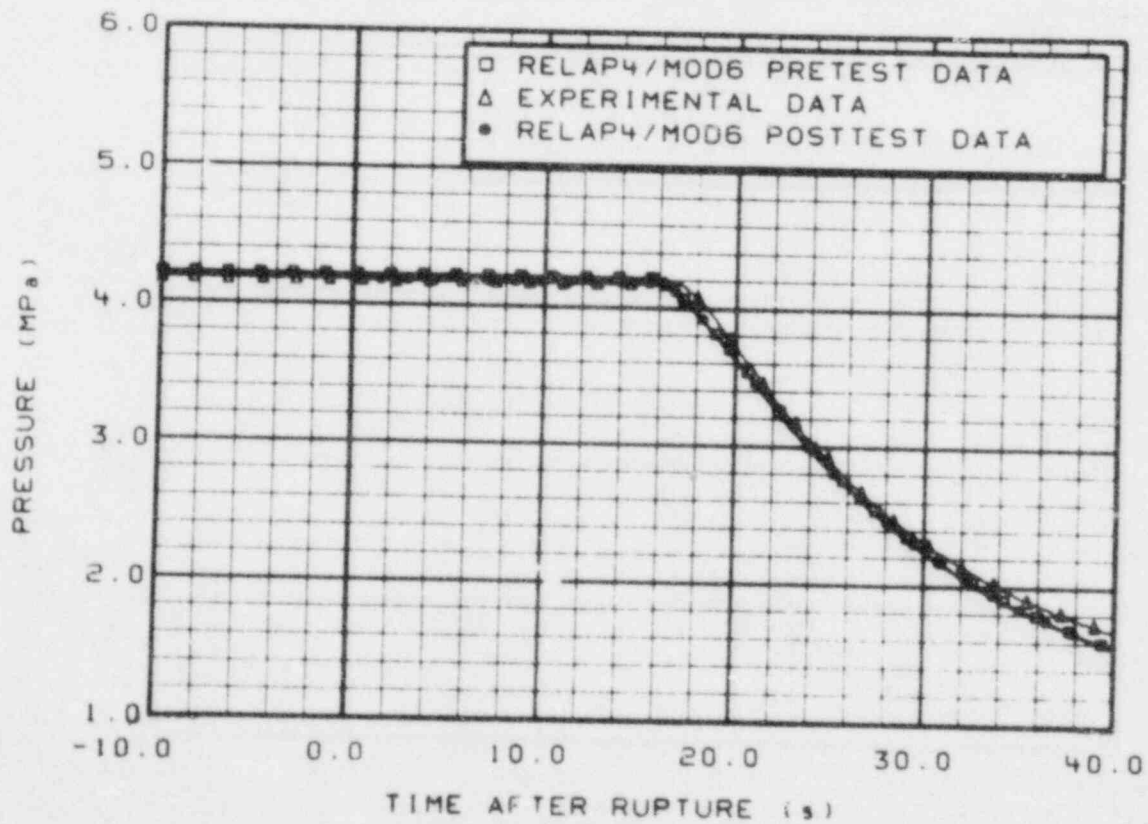


Figure A-42. Comparison of pressure in accumulator for prediction, posttest, and experimental data.

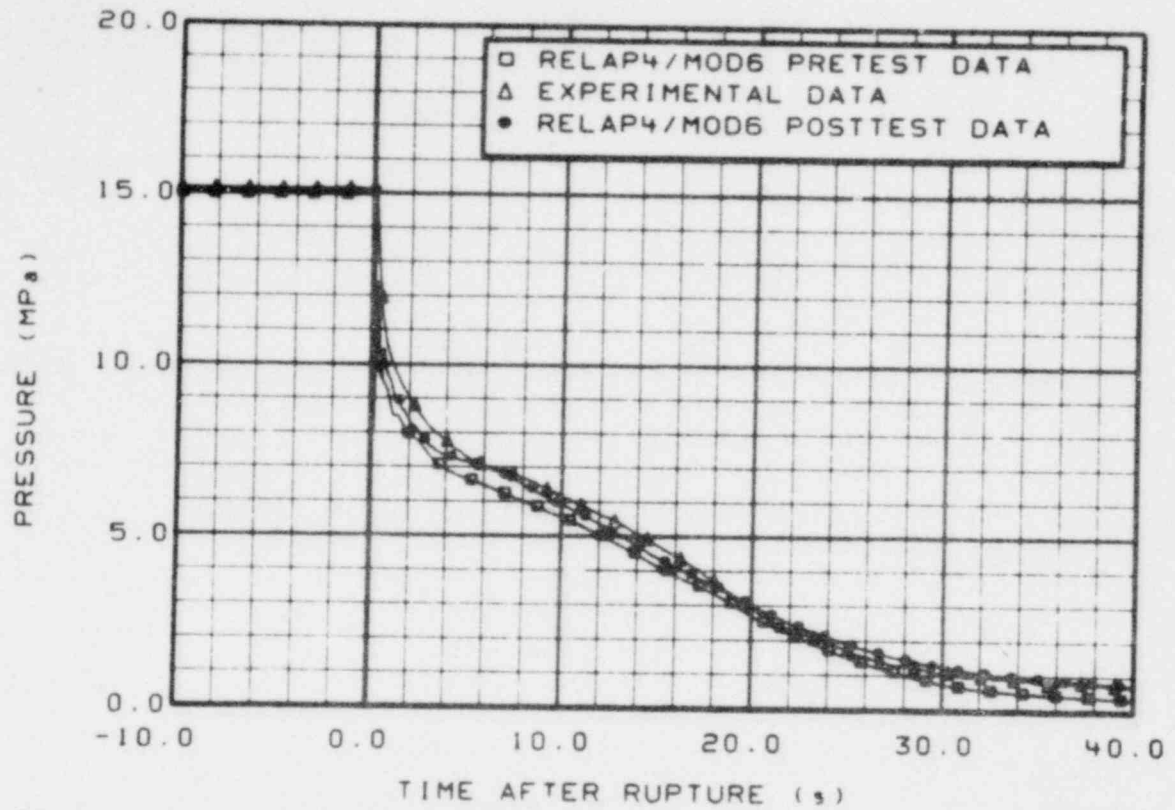


Figure A-43. Comparison of pressure at emergency core coolant cold leg injection point for prediction, posttest, and experimental data.

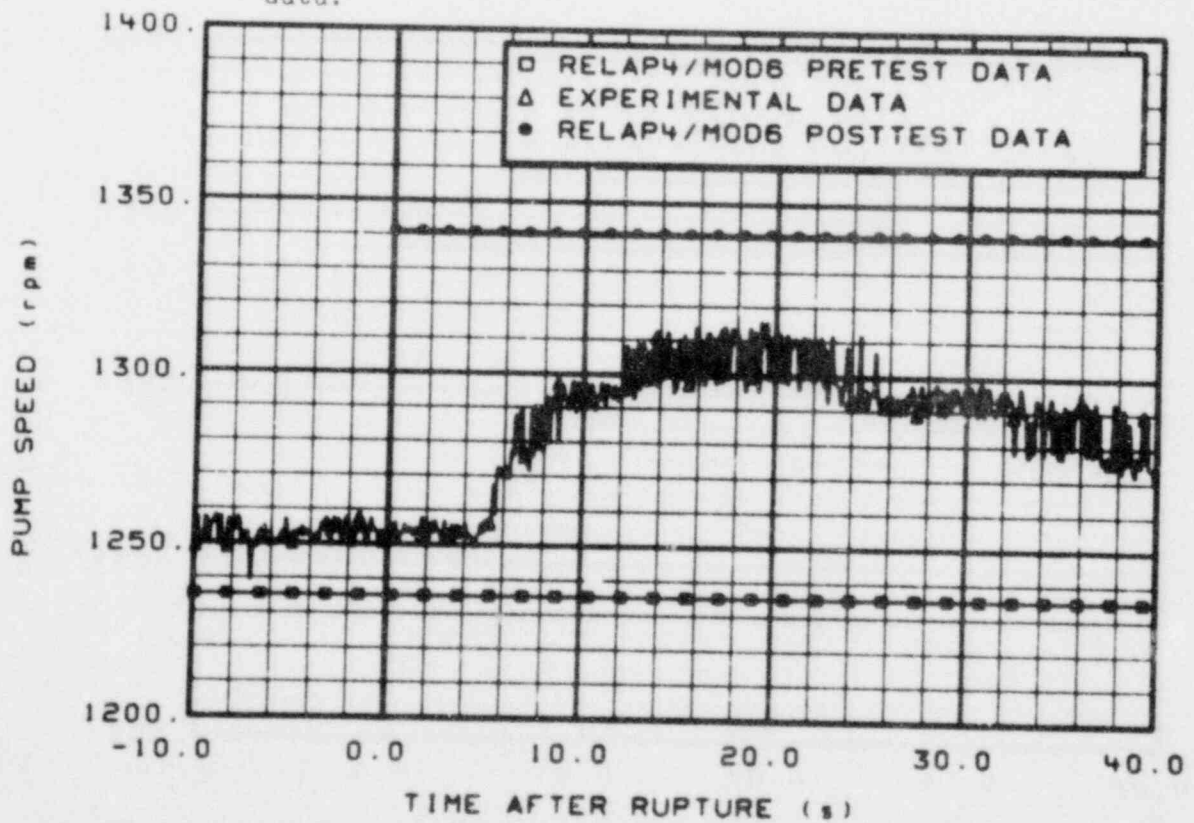


Figure A-44. Comparison of Pump 1 speed for prediction, posttest, and experimental data.

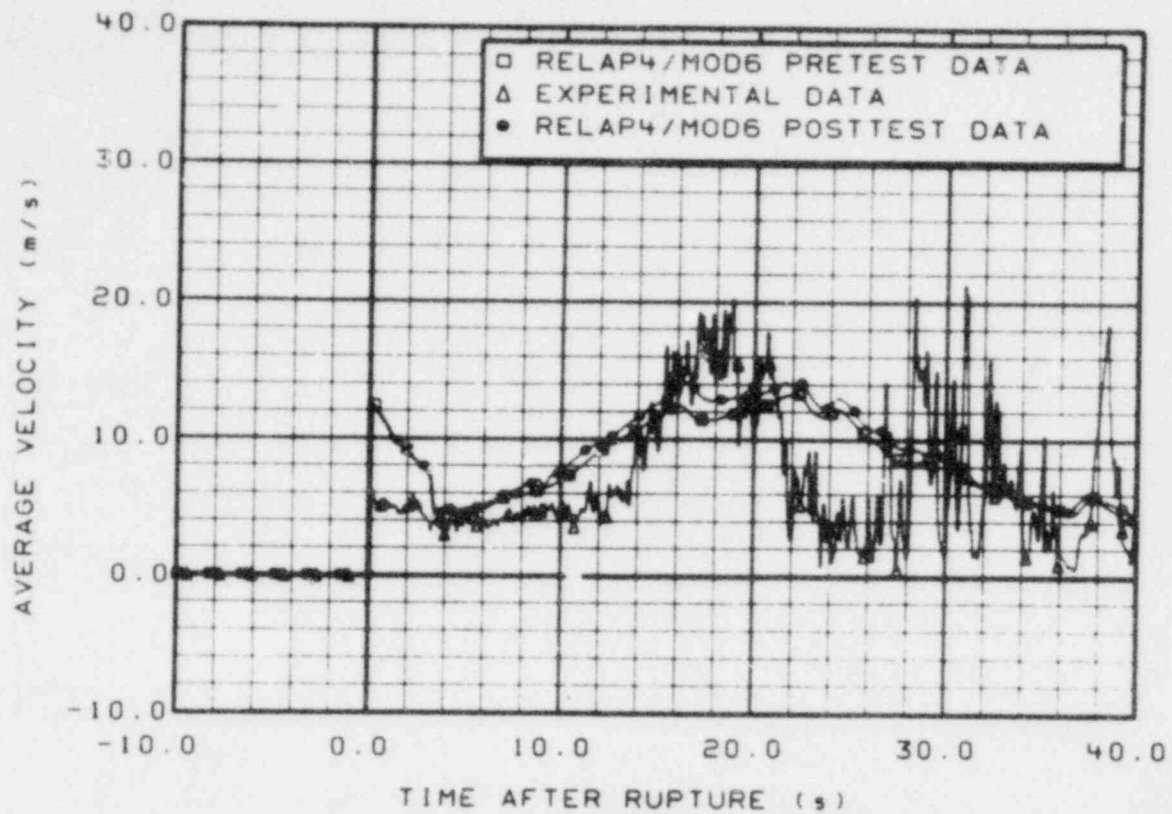


Figure A-45. Comparison of average fluid velocity in broken loop cold leg for prediction, posttest, and experimental data.

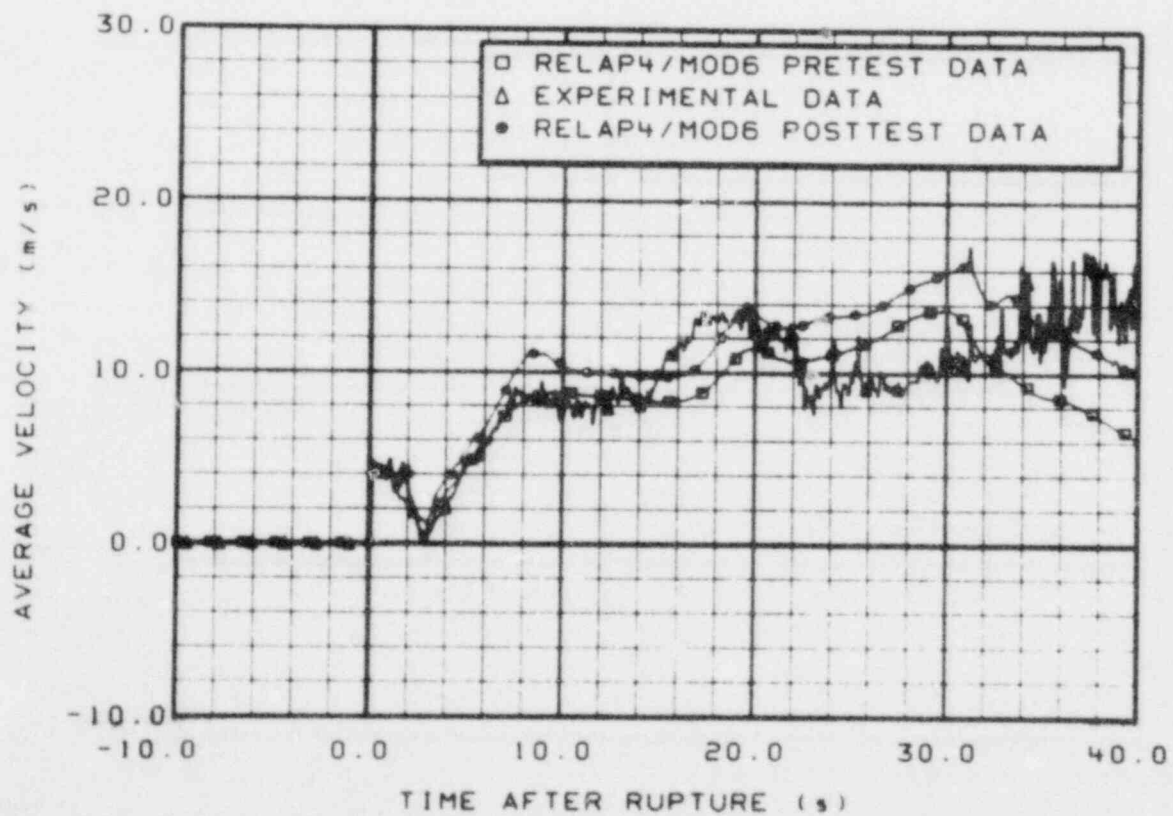


Figure A-46. Comparison of average fluid velocity in broken loop hot leg for prediction, posttest, and experimental data.

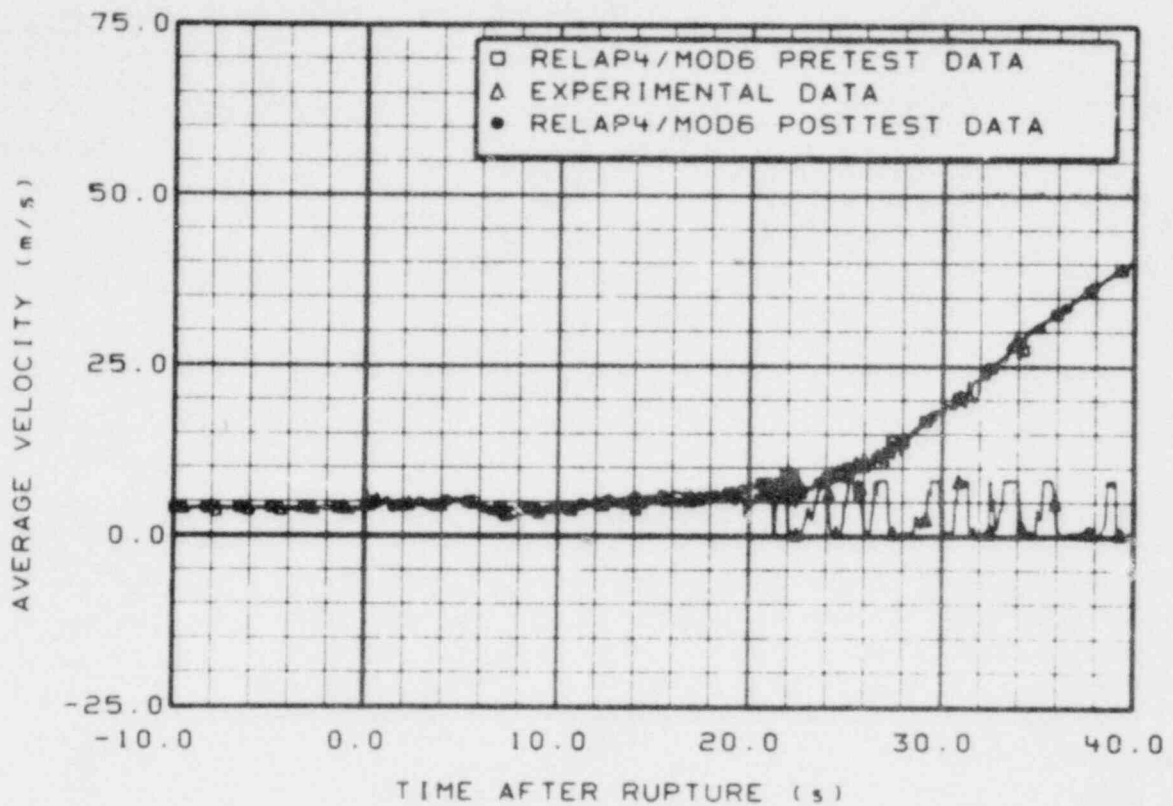


Figure A-47. Comparison of average fluid velocity in intact loop cold leg for prediction, posttest, and experimental data.

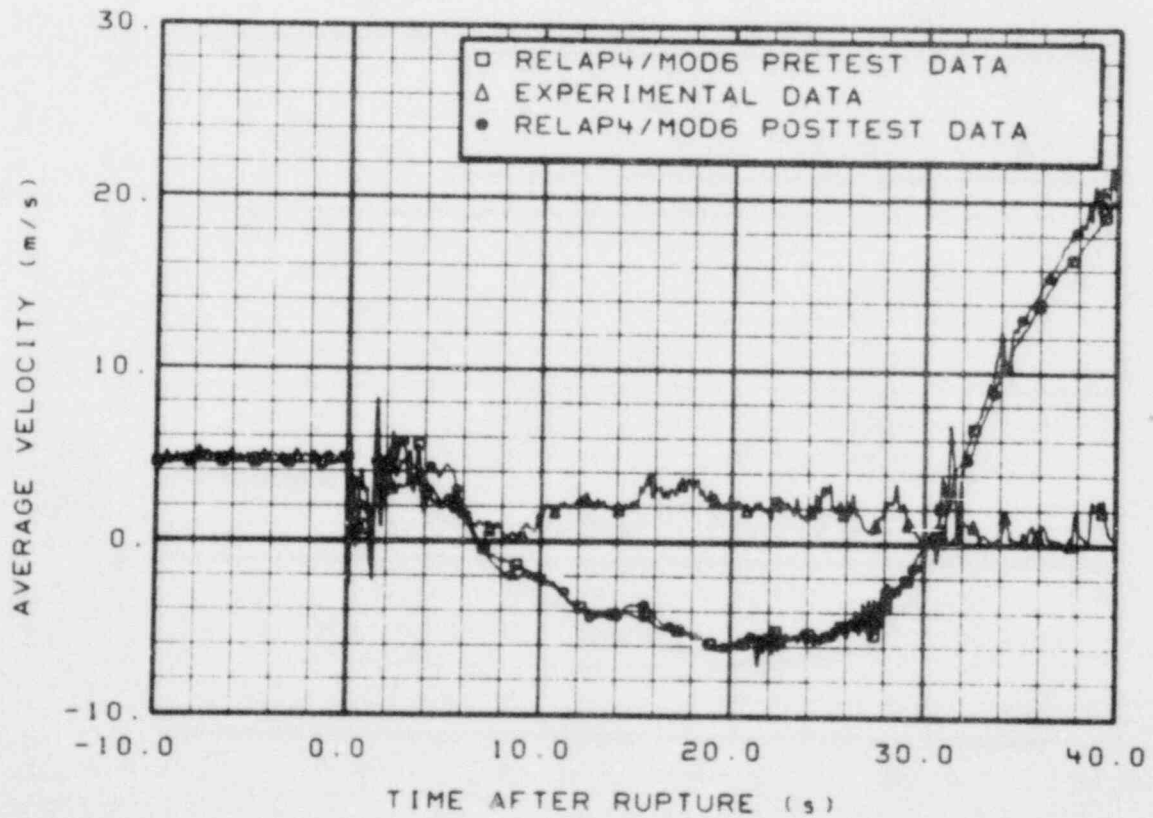


Figure A-48. Comparison of average fluid velocity in intact loop hot leg for prediction, posttest, and experimental data.

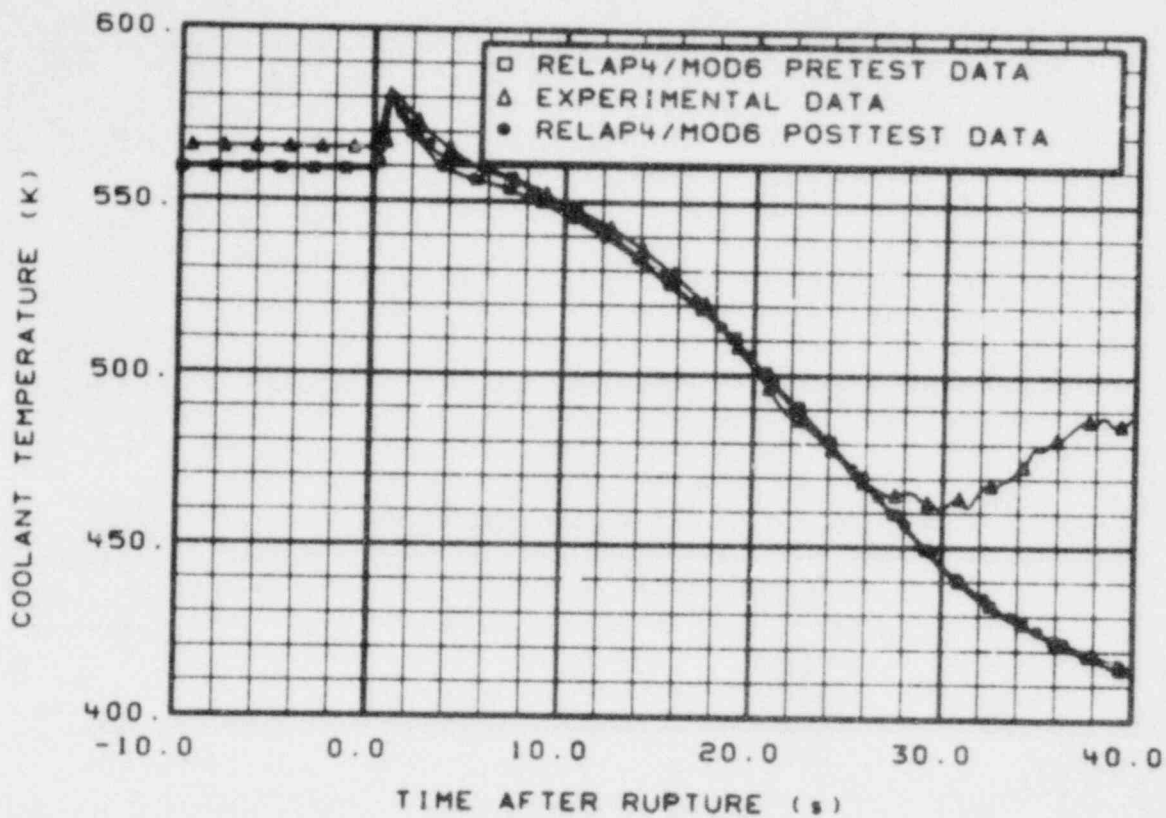


Figure A-49. Comparison of average coolant temperature in broken loop hot leg for prediction, posttest, and experimental data.

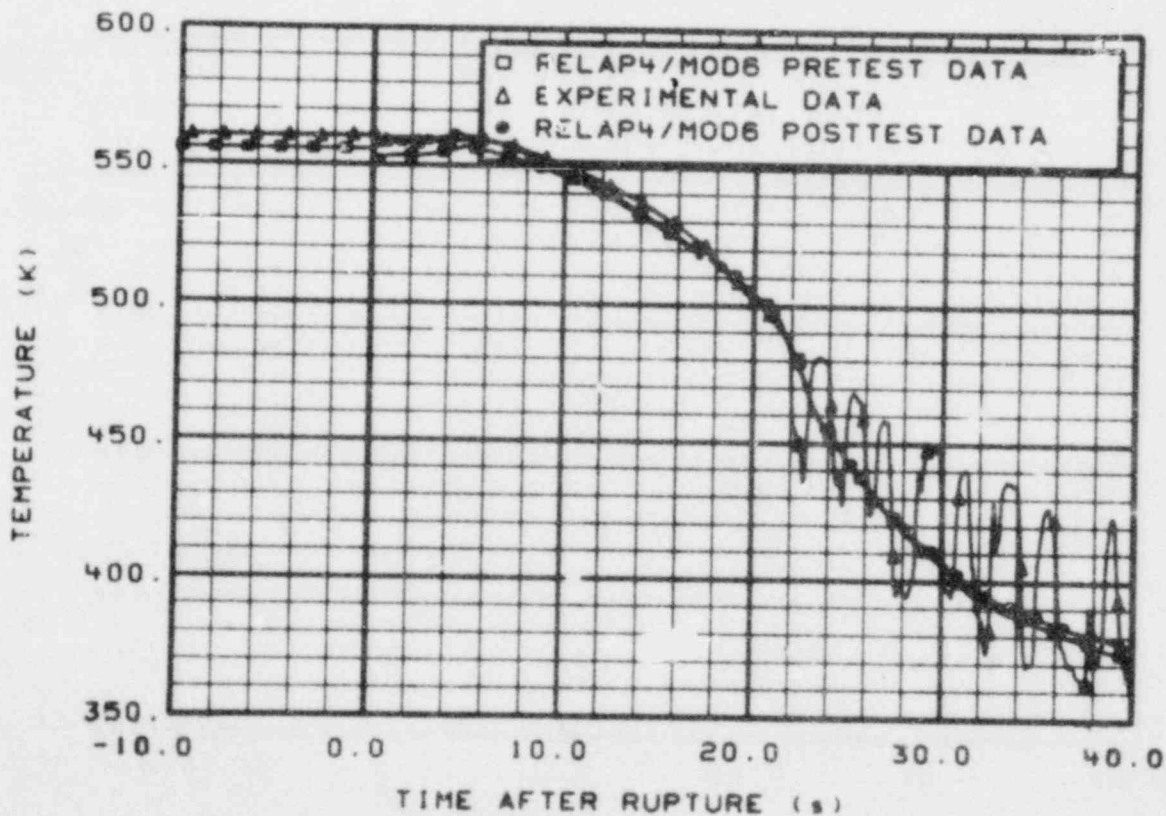


Figure A-50. Comparison of average coolant temperature in intact loop cold leg for prediction, posttest, and experimental data.

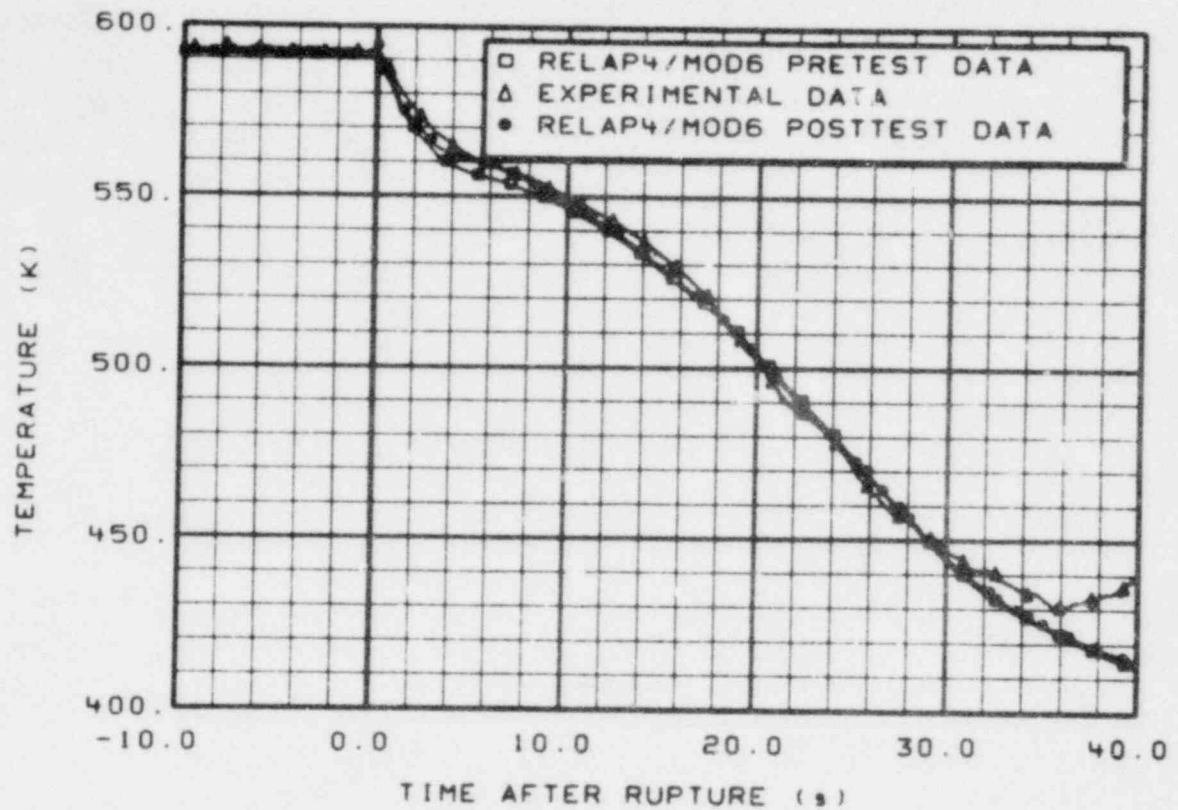


Figure A-51. Comparison of average coolant temperature in intact loop hot leg for prediction, posttest, and experimental data.

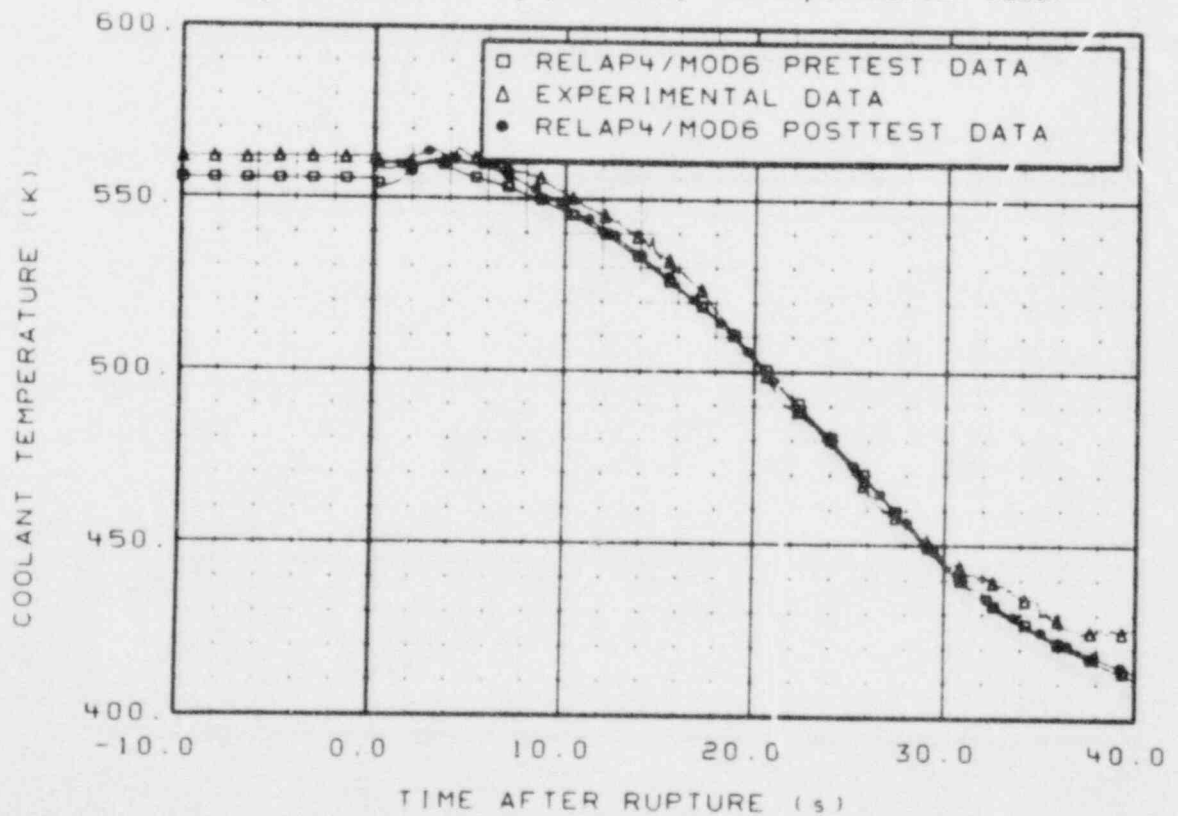


Figure A-52. Comparison of coolant temperature on instrument Stalk 1 at 4.808 m above reactor vessel bottom for prediction, posttest, and experimental data.

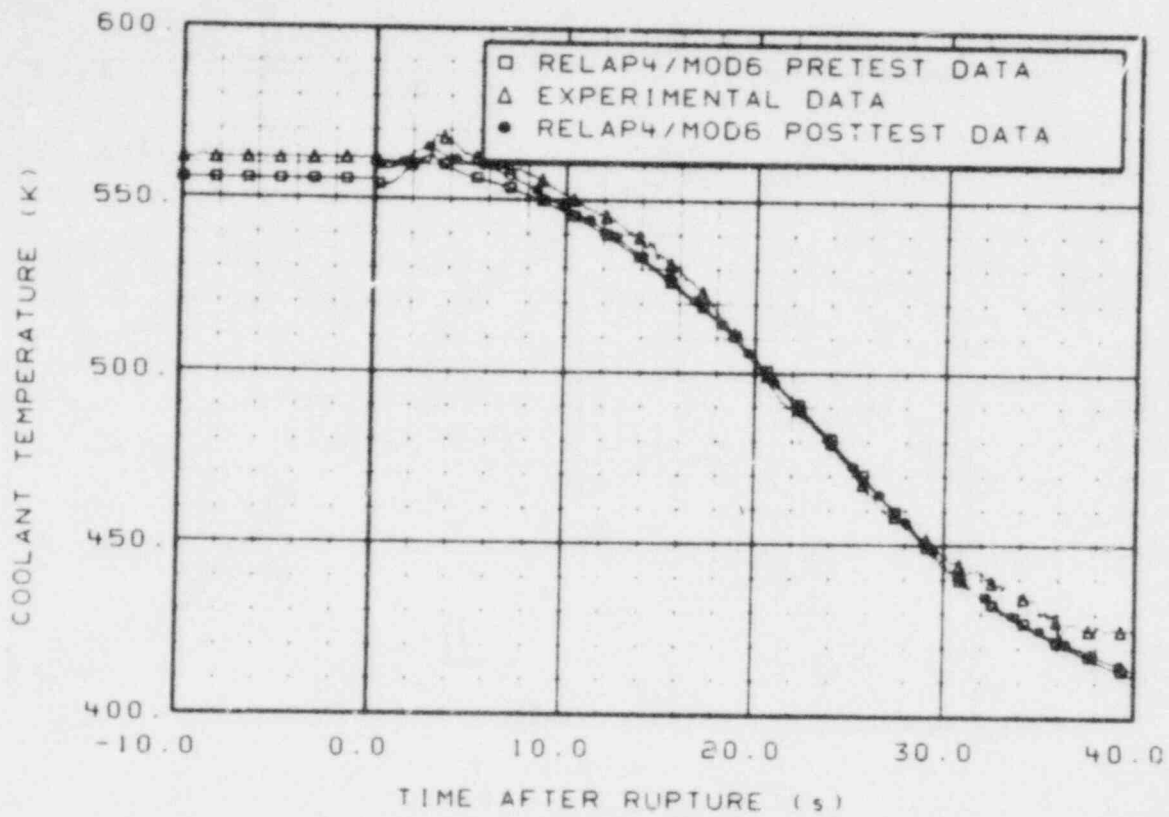


Figure A-53. Comparison of coolant temperature on instrument Stalk 1 at 4.199 m above reactor vessel bottom for prediction, posttest, and experimental data.

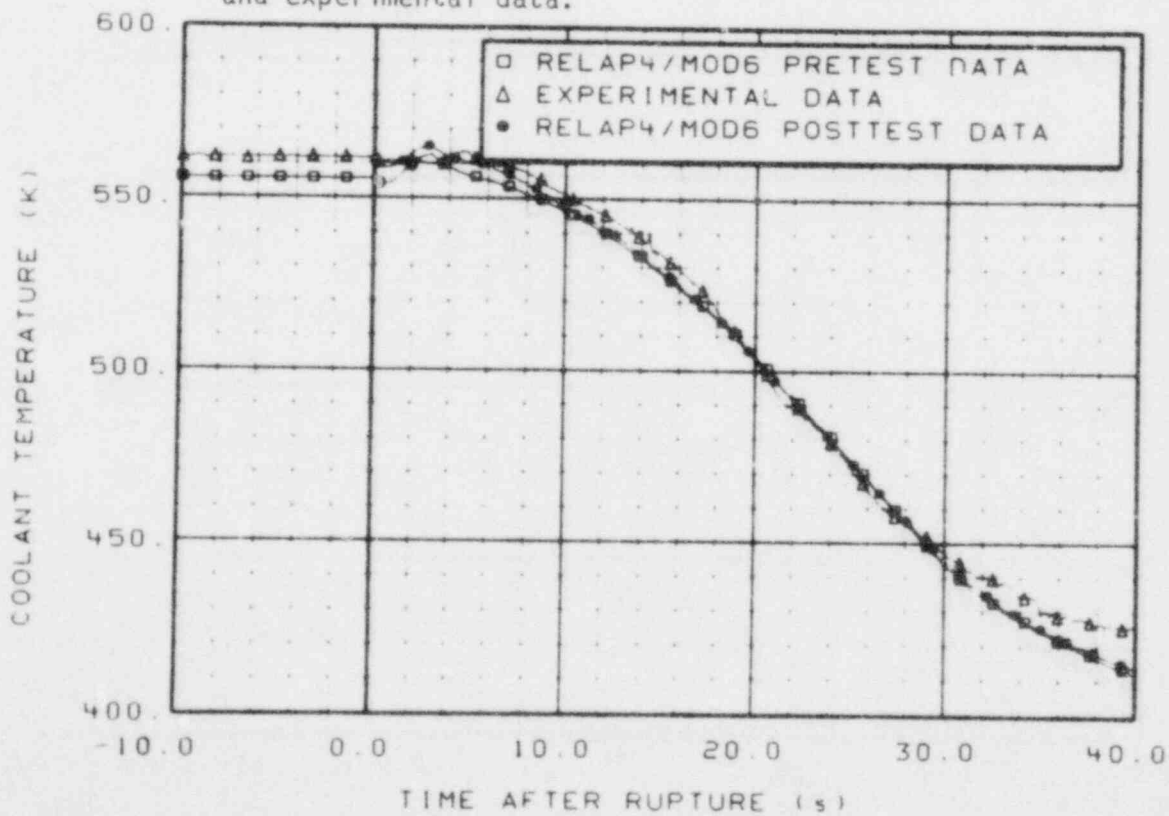


Figure A-54. Comparison of coolant temperature on instrument Stalk 1 at 3.589 m above reactor vessel bottom for prediction, posttest, and experimental data.

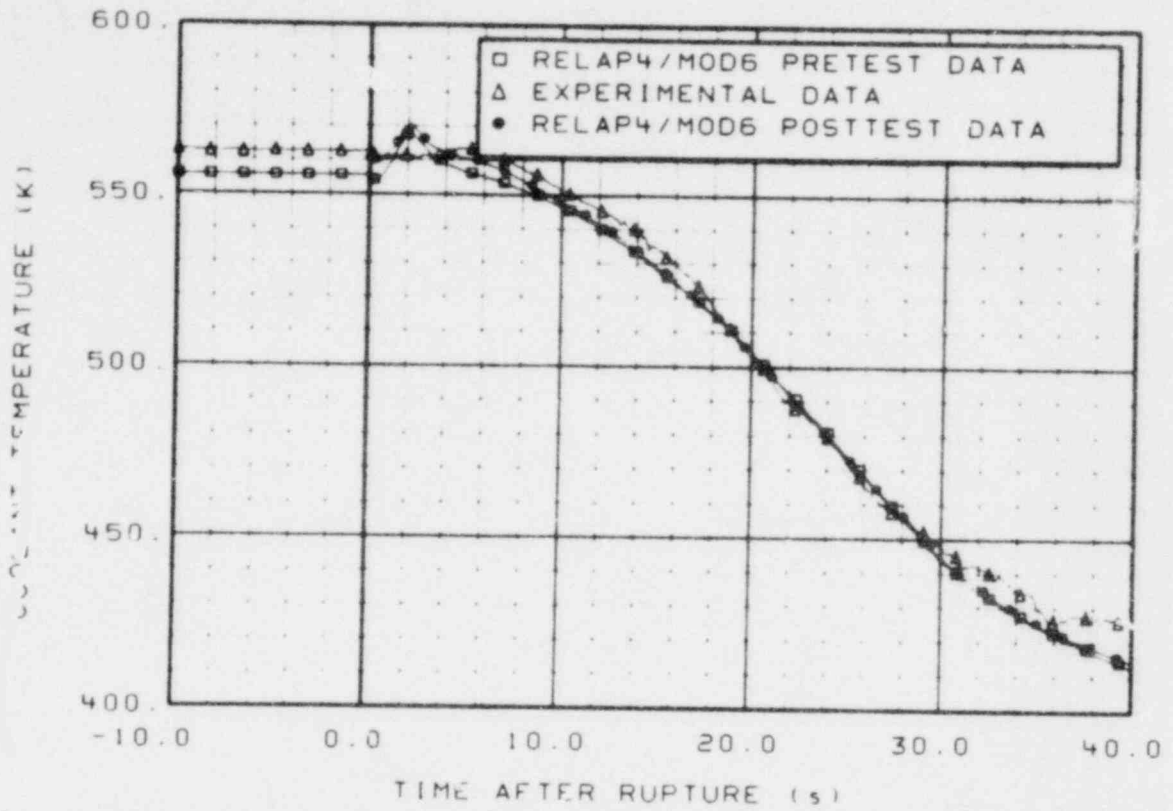


Figure A-55. Comparison of coolant temperature on instrument Stalk 1 at 2.979 m above reactor vessel bottom for prediction, posttest, and experimental data.

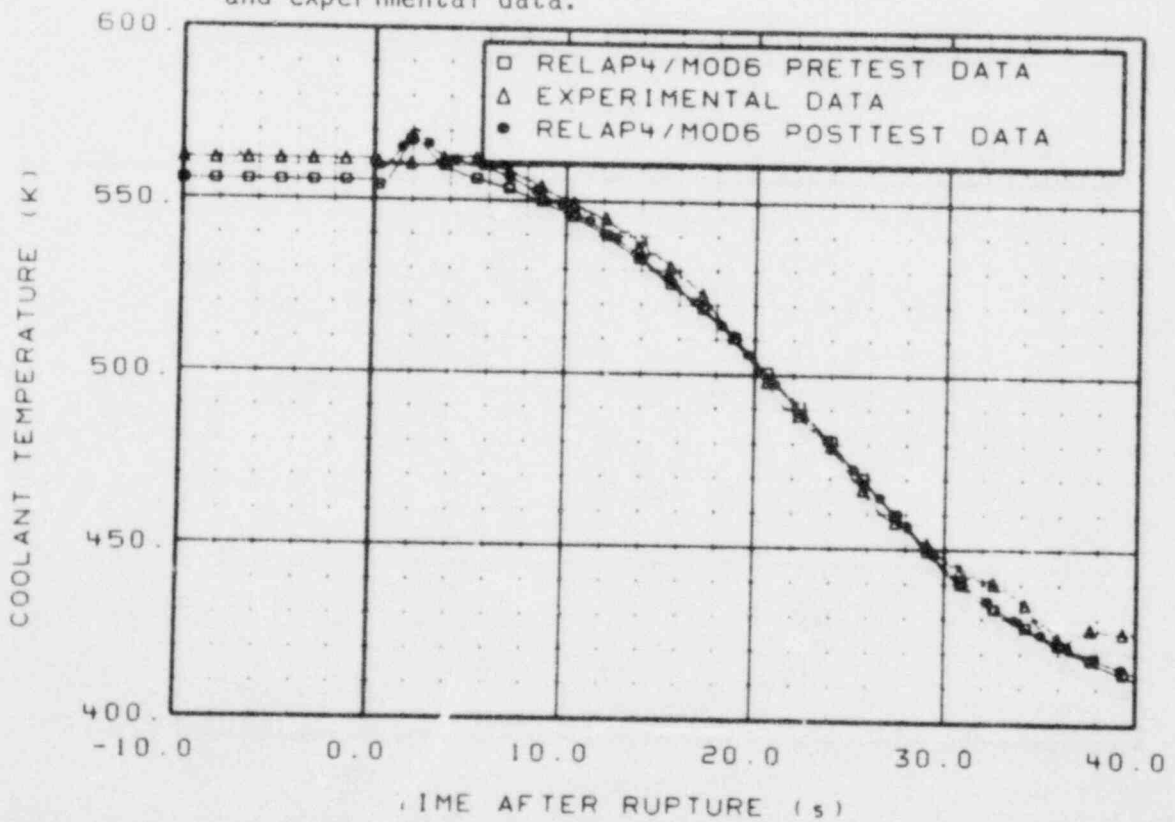


Figure A-56. Comparison of coolant temperature on instrument Stalk 1 at 2.370 m above reactor vessel bottom for prediction, posttest, and experimental data.

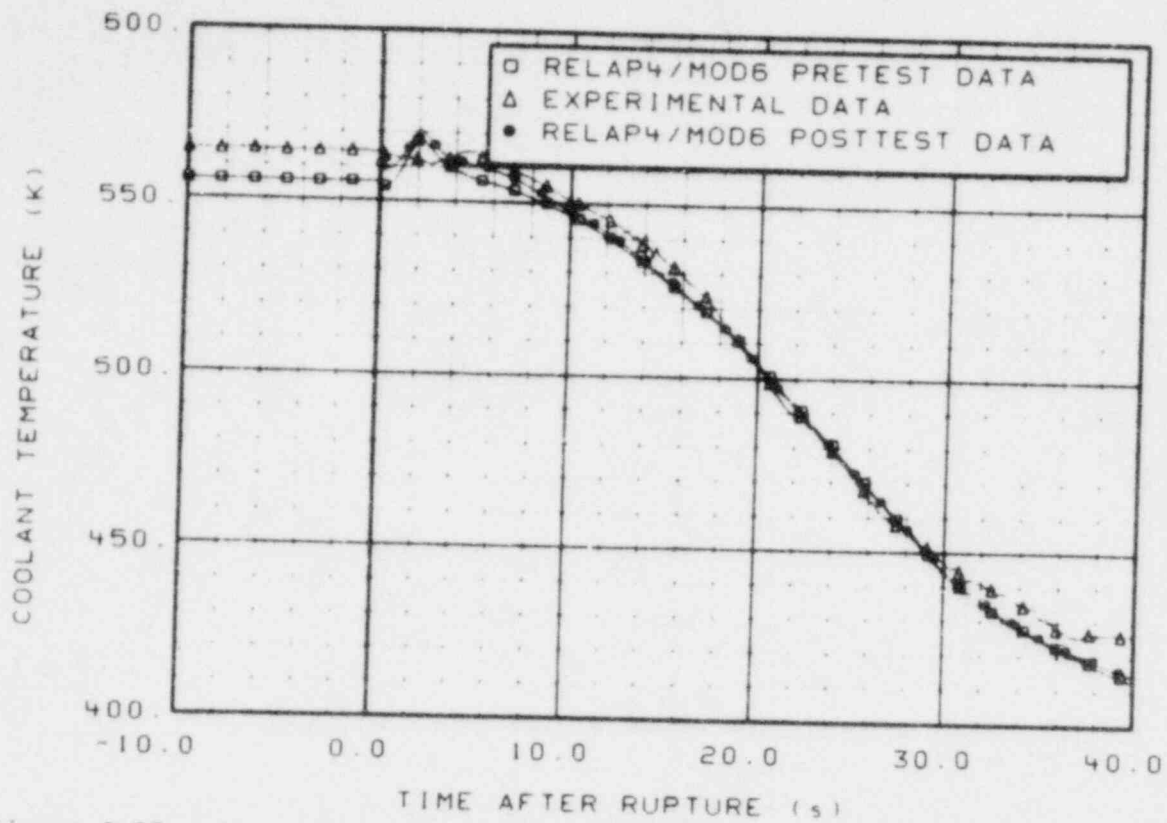


Figure A-57. Comparison of coolant temperature on instrument Stalk 1 at 1.760 m above reactor vessel bottom for prediction, posttest, and experimental data.

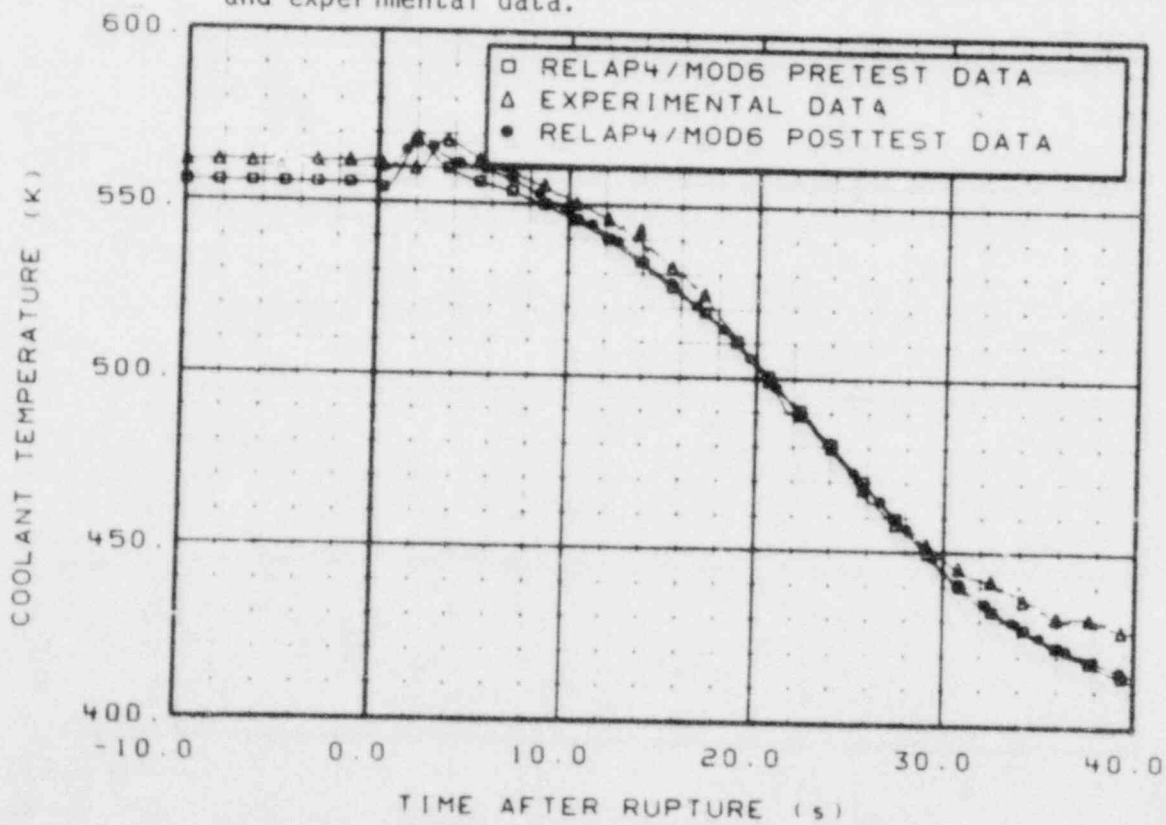


Figure A-58. Comparison of coolant temperature on instrument Stalk 1 at 0.744 m above reactor vessel bottom for prediction, posttest, and experimental data.

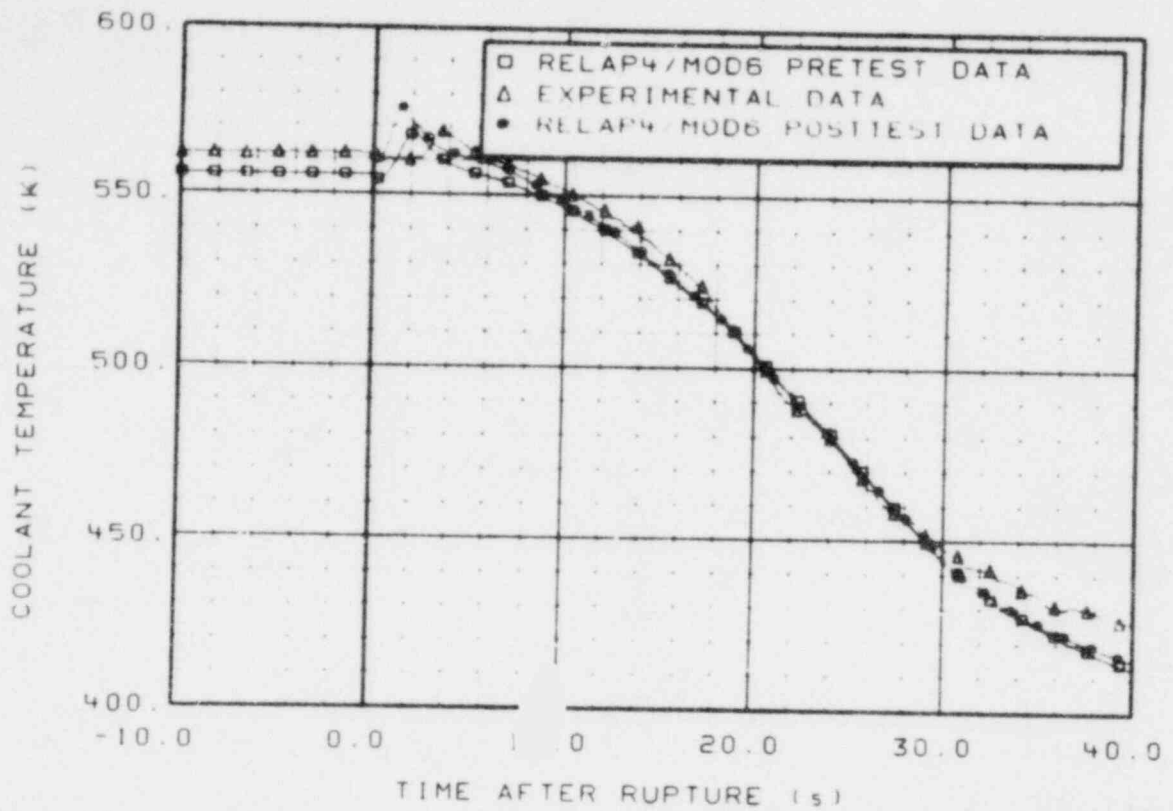


Figure A-59. Comparison of coolant temperature on instrument Stalk 1 at 0.643 m above reactor vessel bottom for prediction, posttest, and experimental data.

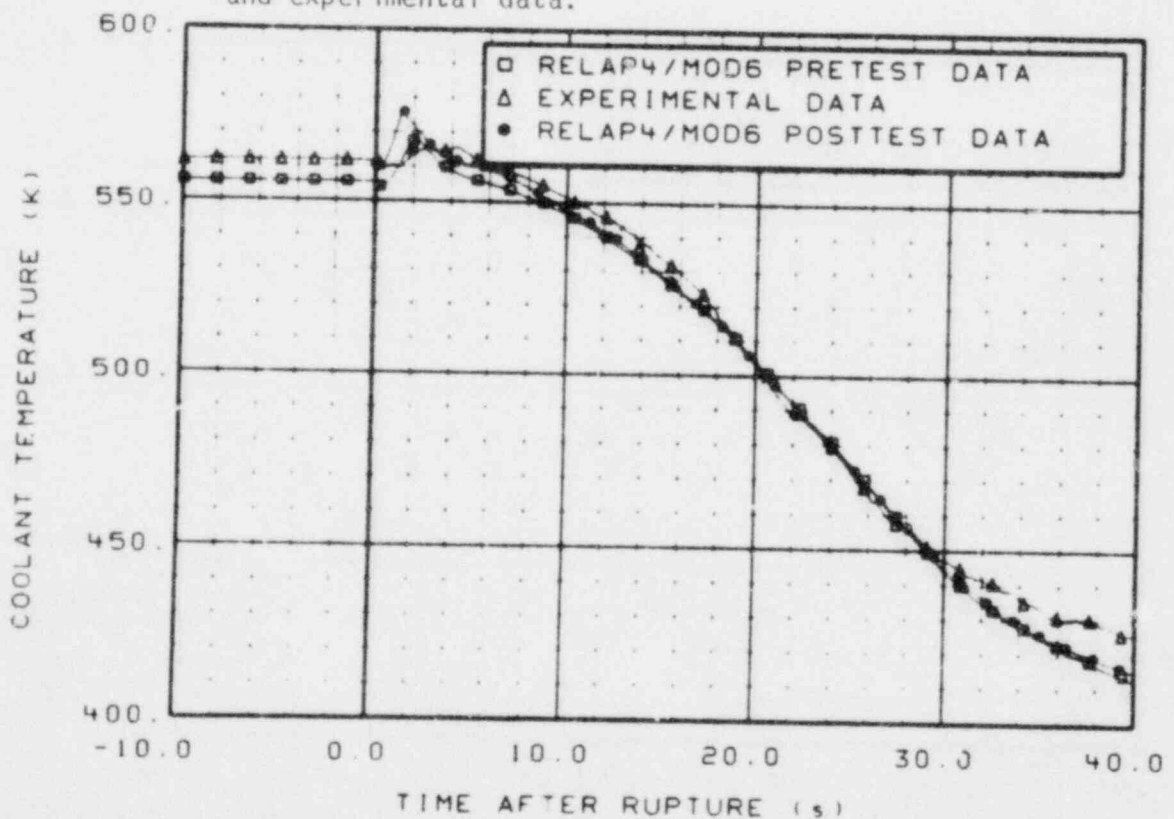


Figure A-60. Comparison of coolant temperature on instrument Stalk 1 at 0.439 m above reactor vessel bottom for prediction, posttest, and experimental data.

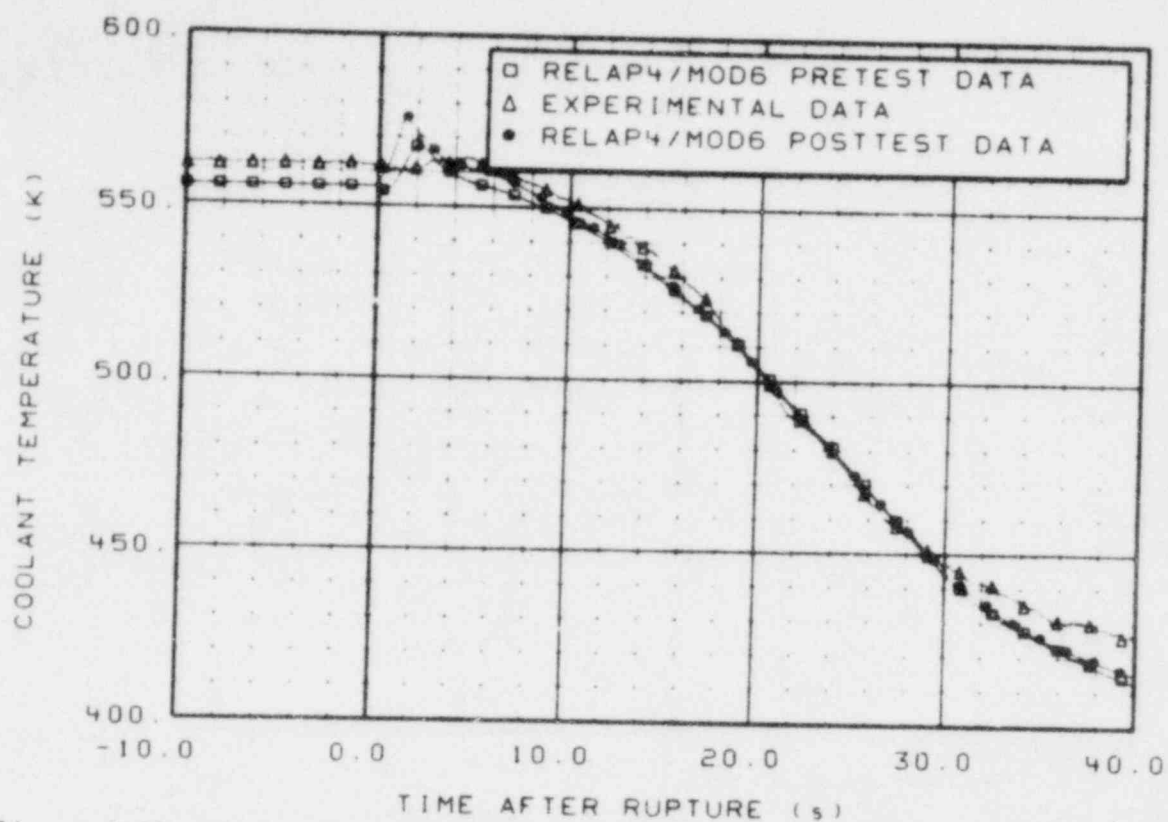


Figure A-61. Comparison of coolant temperature on instrument Stalk 1 at 0.338 m above reactor vessel bottom for prediction, posttest, and experimental data.

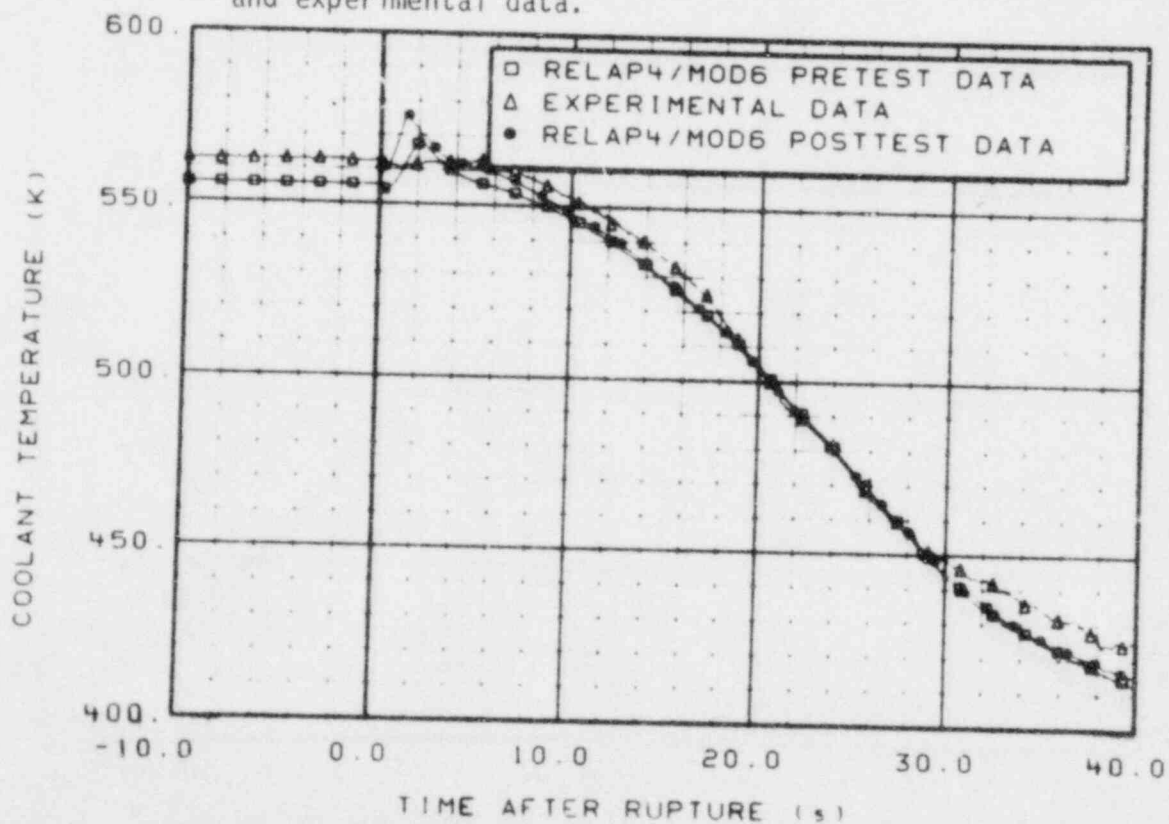


Figure A-62. Comparison of coolant temperature on instrument Stalk 1 at 0.236 m above reactor vessel bottom for prediction, posttest, and experimental data.

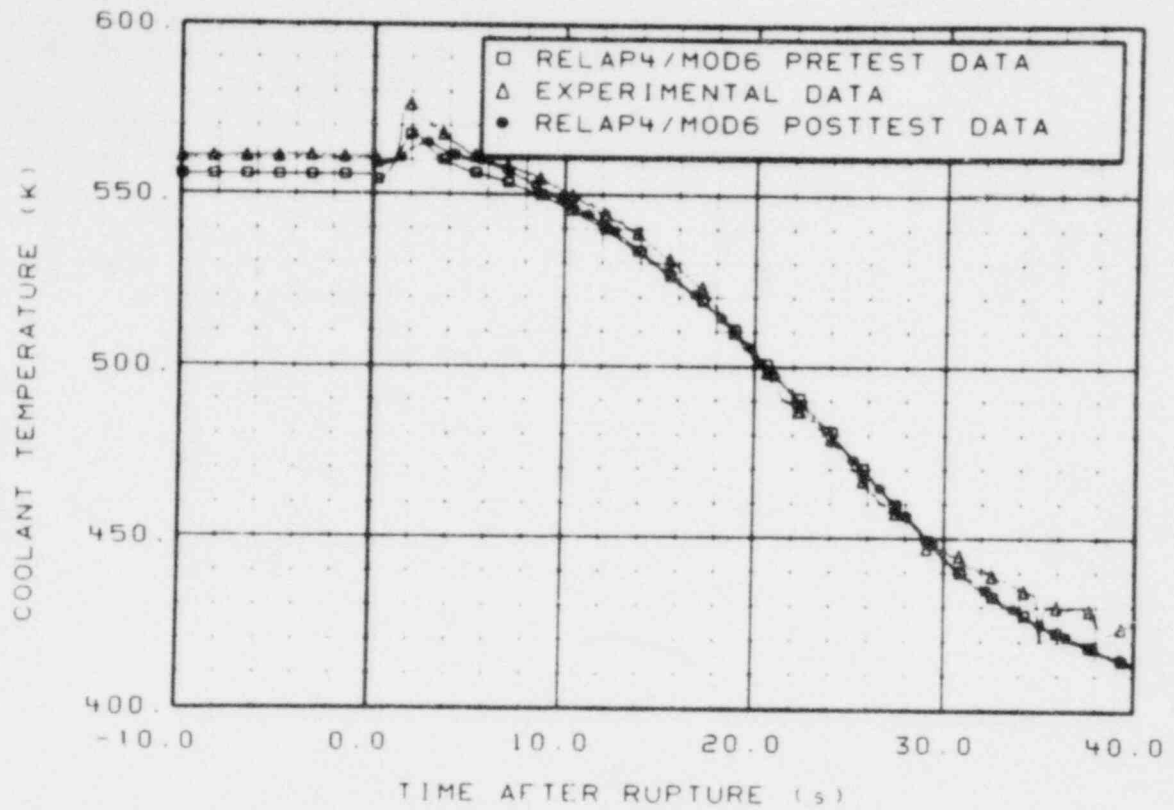


Figure A-63. Comparison of coolant temperature on instrument Stalk 1 at 1.166 m above reactor vessel bottom for prediction, posttest, and experimental data.

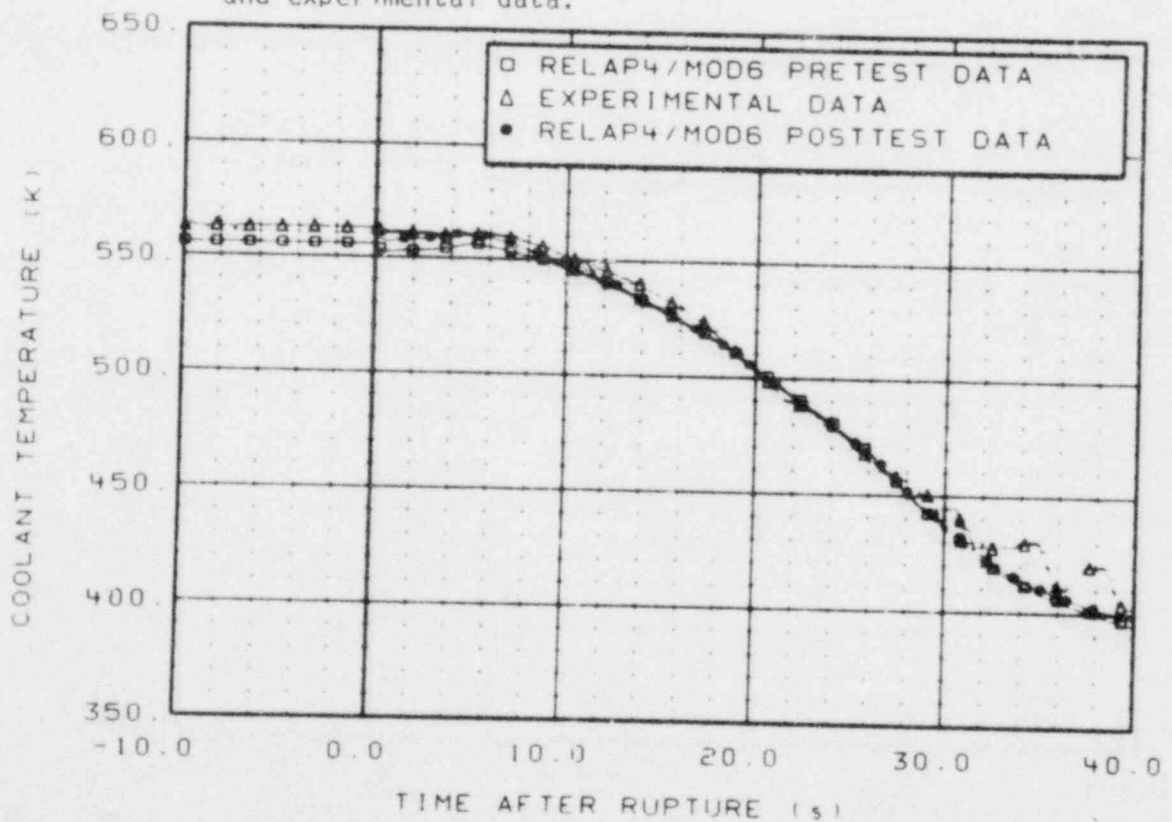


Figure A-64. Comparison of coolant temperature on instrument Stalk 2 at 4.808 m above reactor vessel bottom for prediction, posttest, and experimental data.

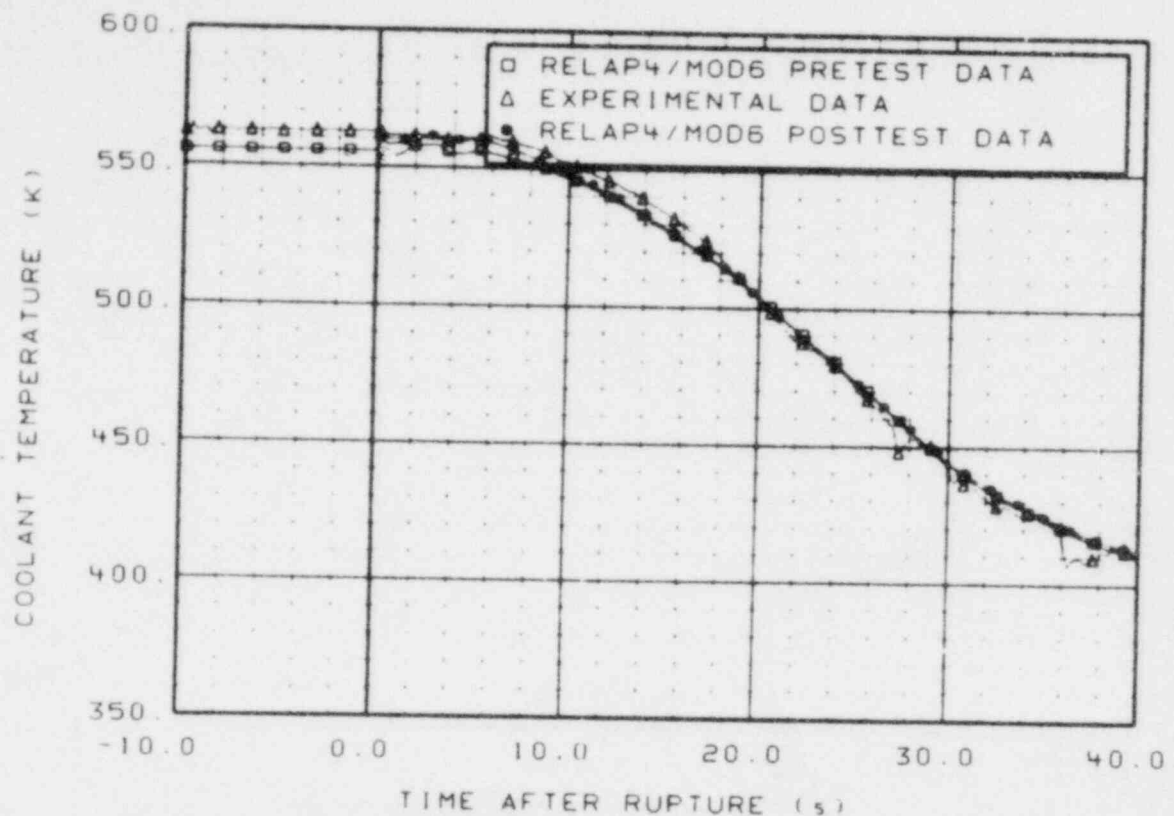


Figure A-65. Comparison of coolant temperature on instrument Stalk 2 at 4.199 m above reactor vessel bottom for prediction, posttest, and experimental data.

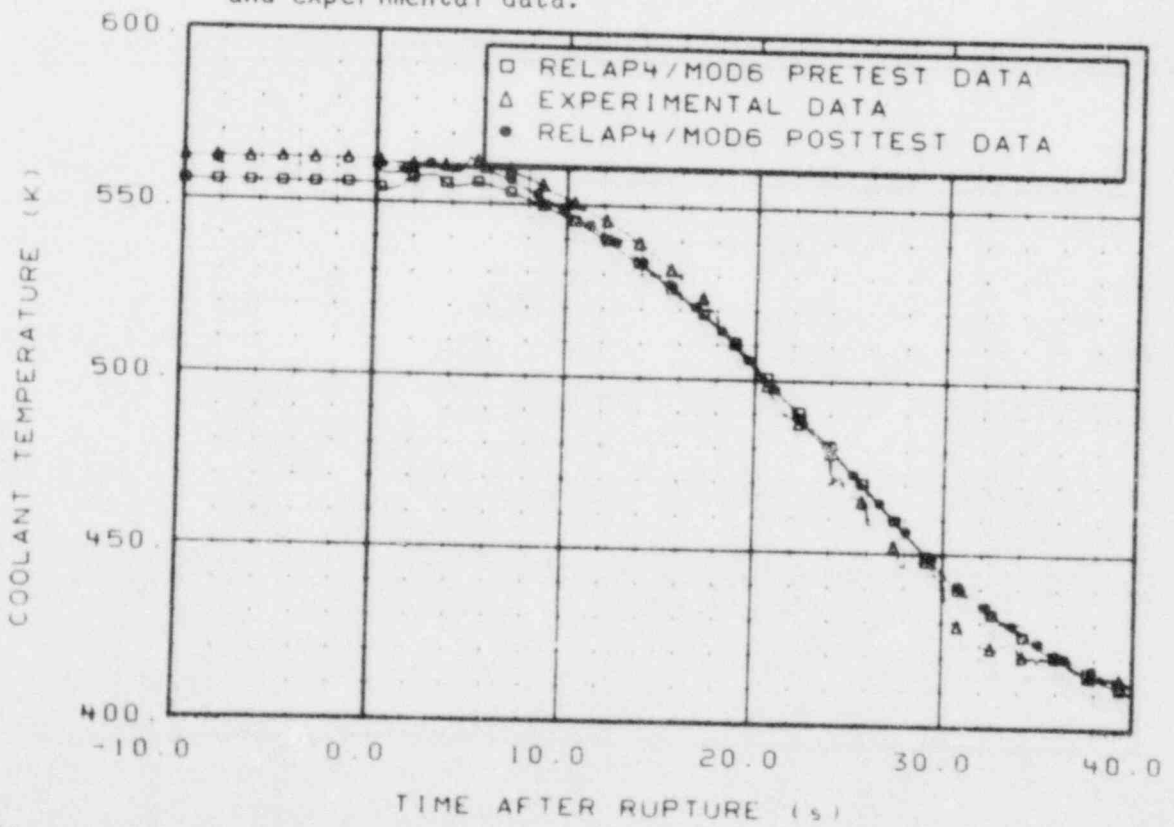


Figure A-66. Comparison of coolant temperature on instrument Stalk 2 at 3.589 m above reactor vessel bottom for prediction, posttest, and experimental data.

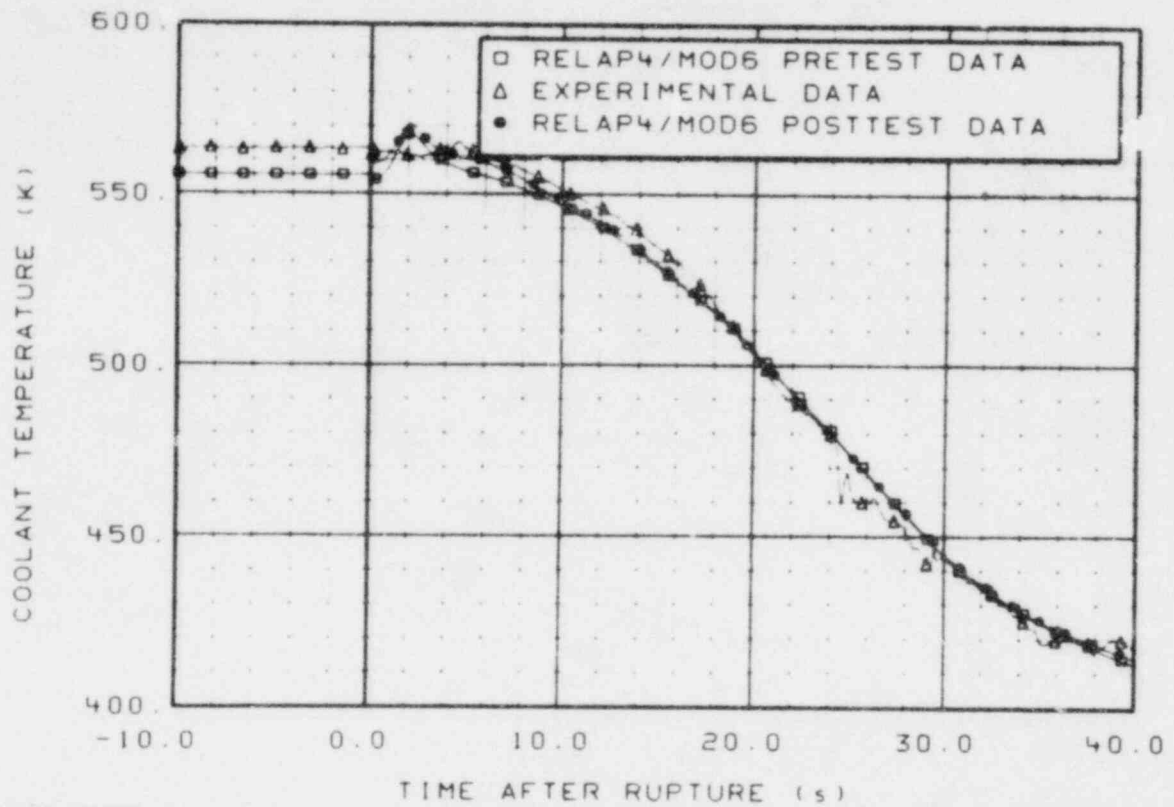


Figure A-67. Comparison of coolant temperature on instrument Stalk 2 at 2.370 m above reactor vessel bottom for prediction, posttest, and experimental data.

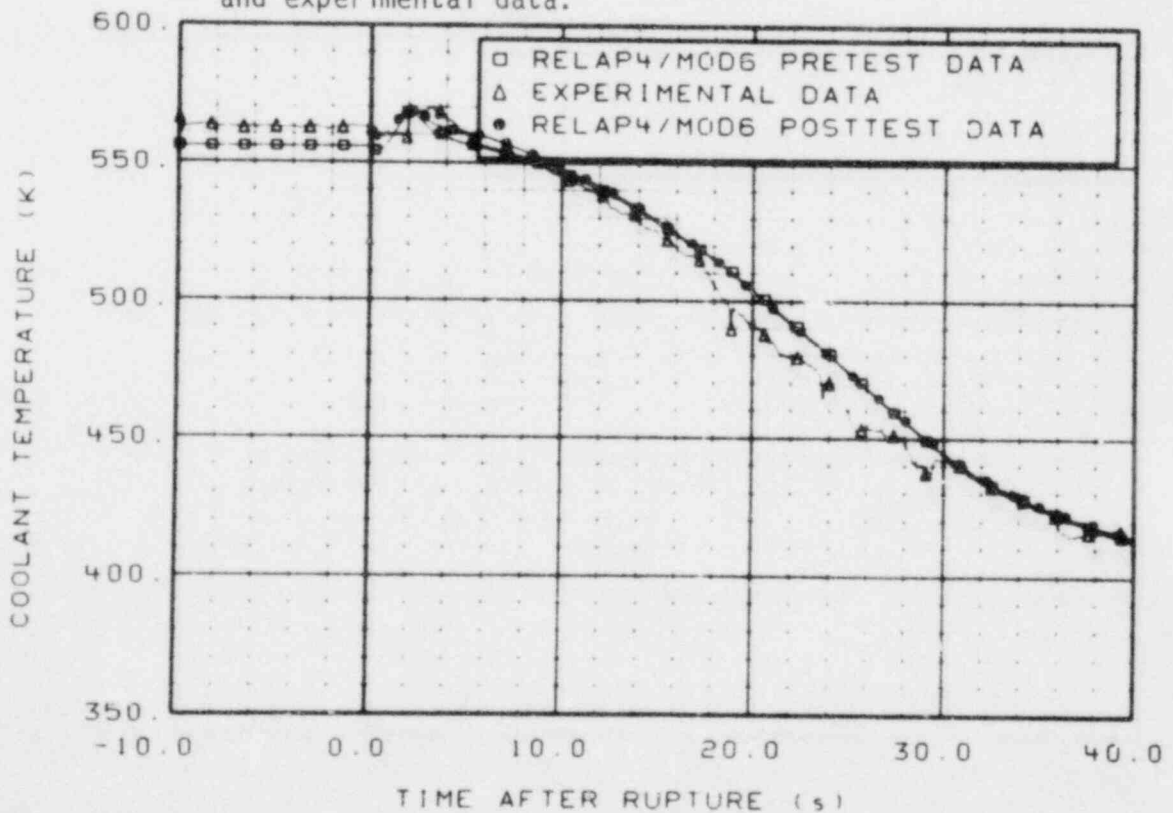


Figure A-68. Comparison of coolant temperature on instrument Stalk 2 at 0.846 m above reactor vessel bottom for prediction, posttest, and experimental data.

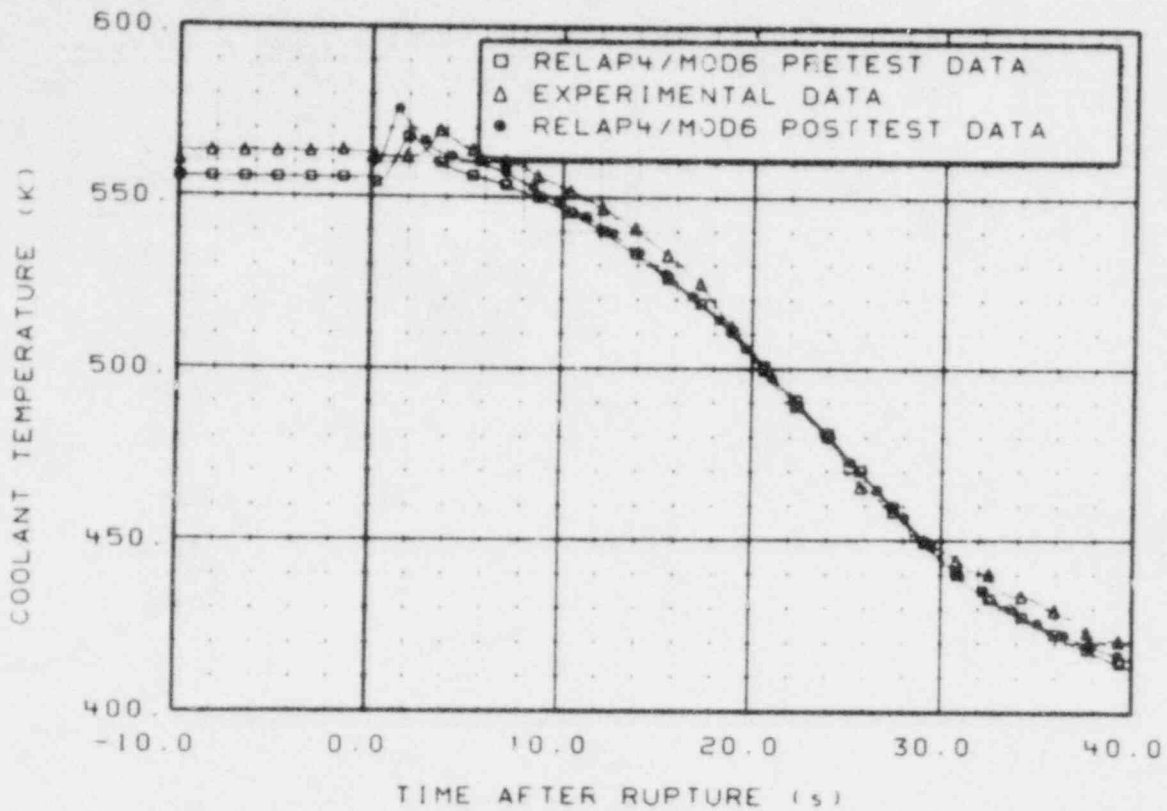


Figure A-69. Comparison of coolant temperature on instrument Stalk 2 at 0.643 m above reactor vessel bottom for prediction, posttest, and experimental data.

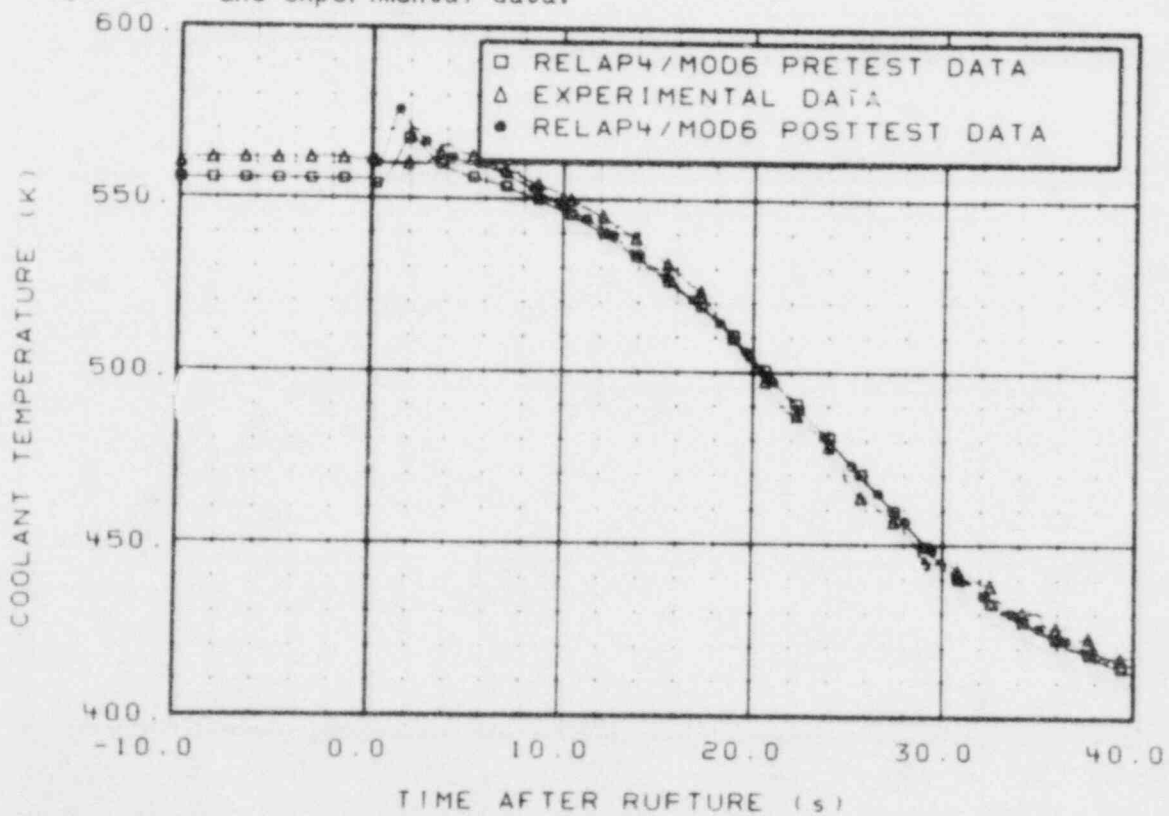


Figure A-70. Comparison of coolant temperature on instrument Stalk 2 at 0.541 m above reactor vessel bottom for prediction, posttest, and experimental data.

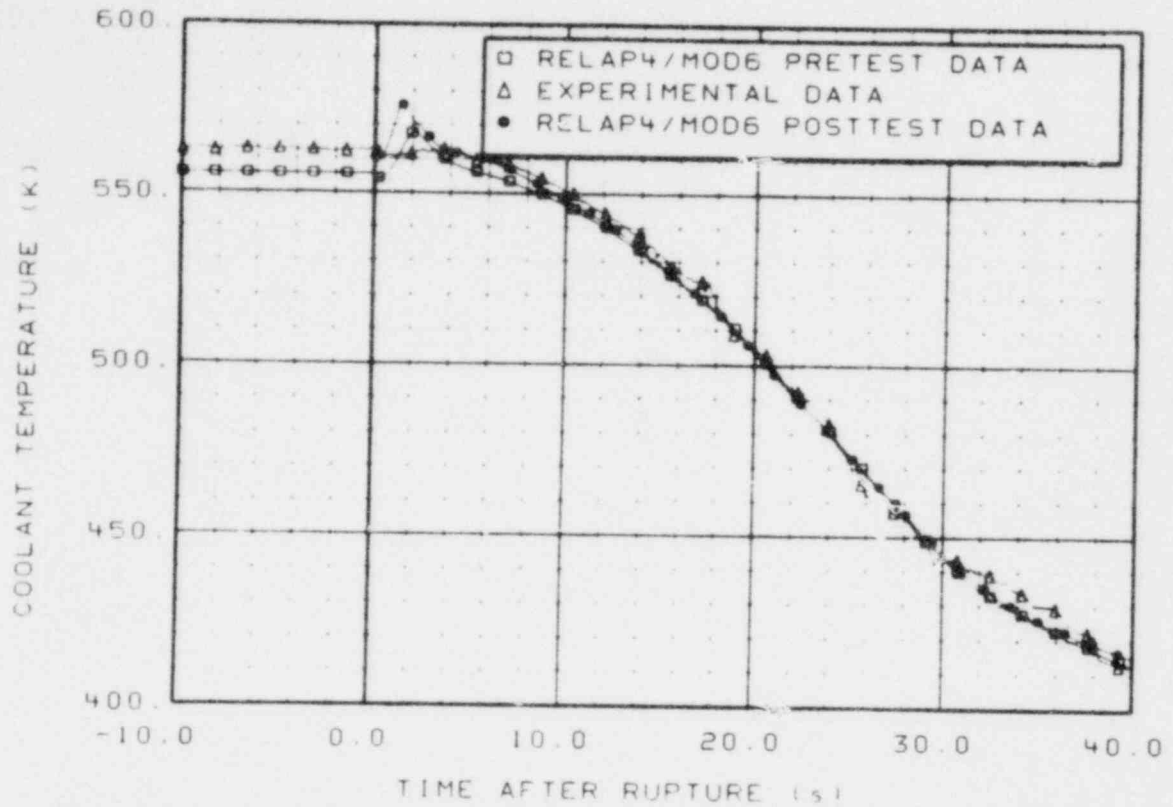


Figure A-71. Comparison of coolant temperature on instrument Stalk 2 at 0.236 m above reactor vessel bottom for prediction, posttest, and experimental data.

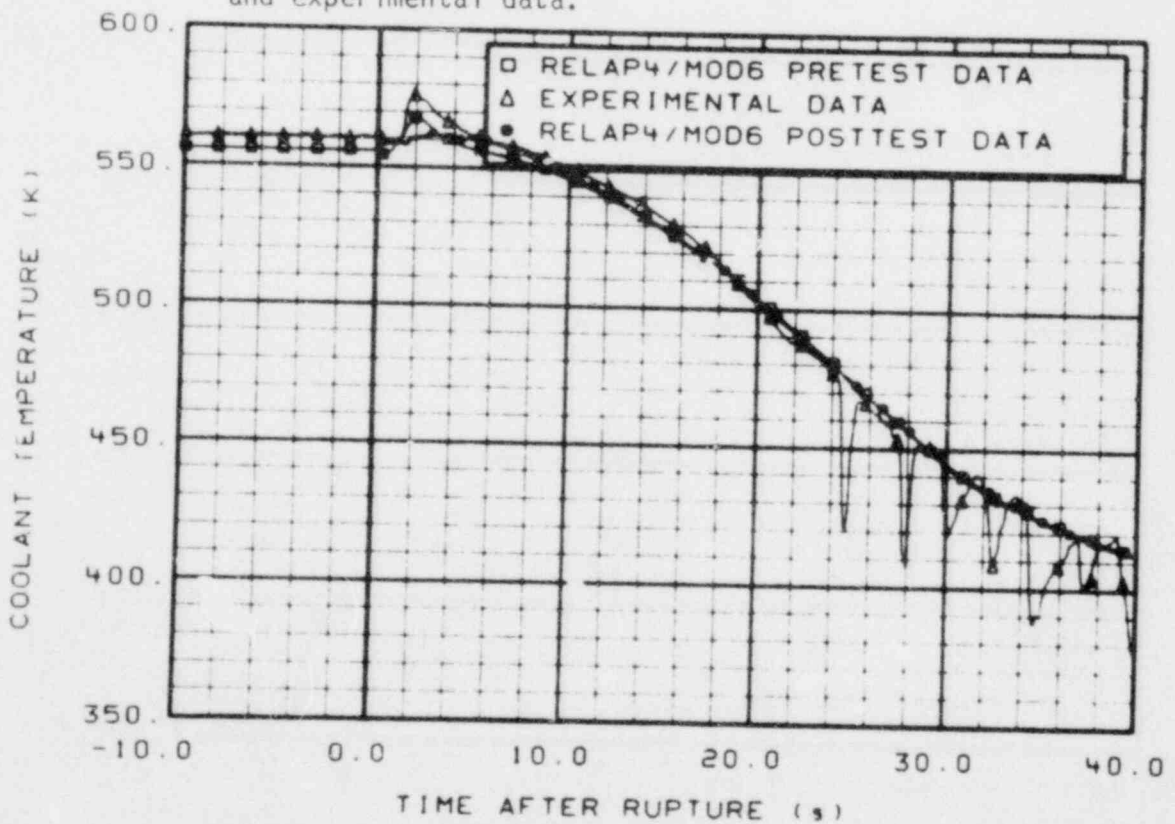


Figure A-72. Comparison of coolant temperature on instrument Stalk 2 at 1.166 m above reactor vessel bottom for prediction, posttest, and experimental data.

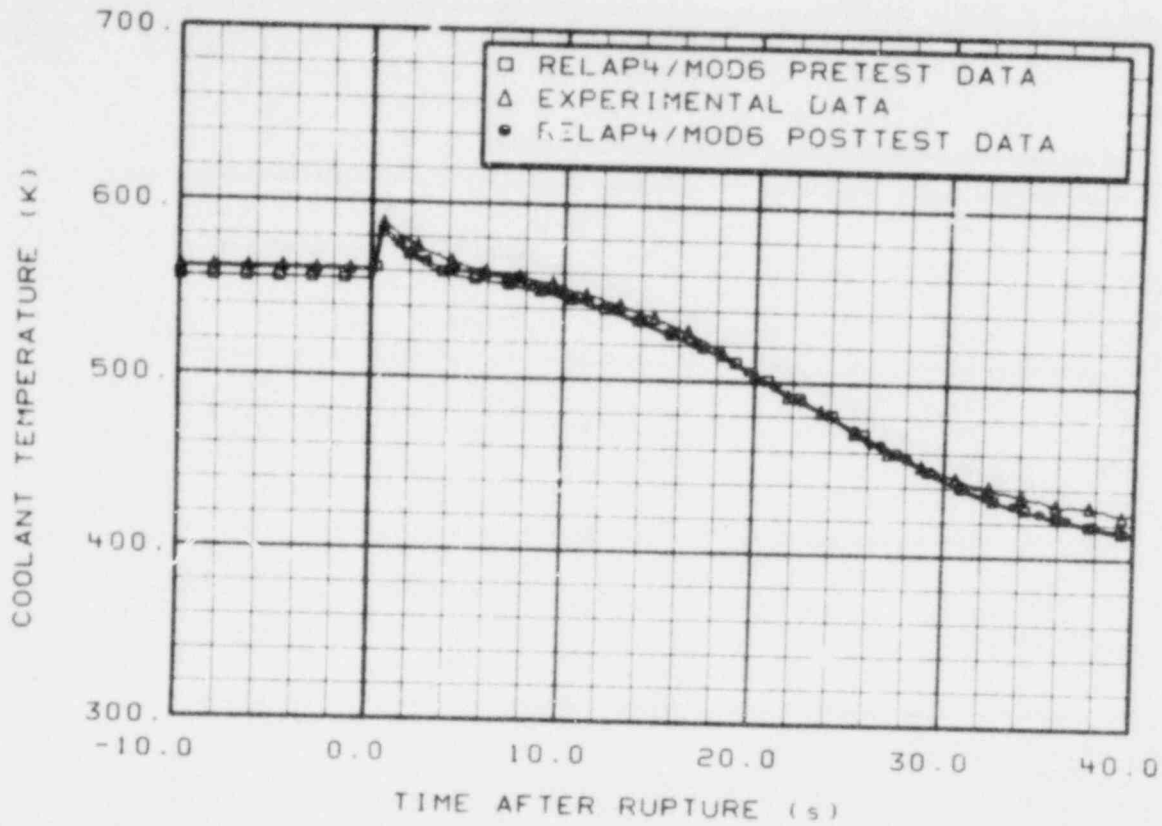


Figure A-73. Comparison of coolant temperature in fuel Module 1 lower end box for prediction, posttest, and experimental data.

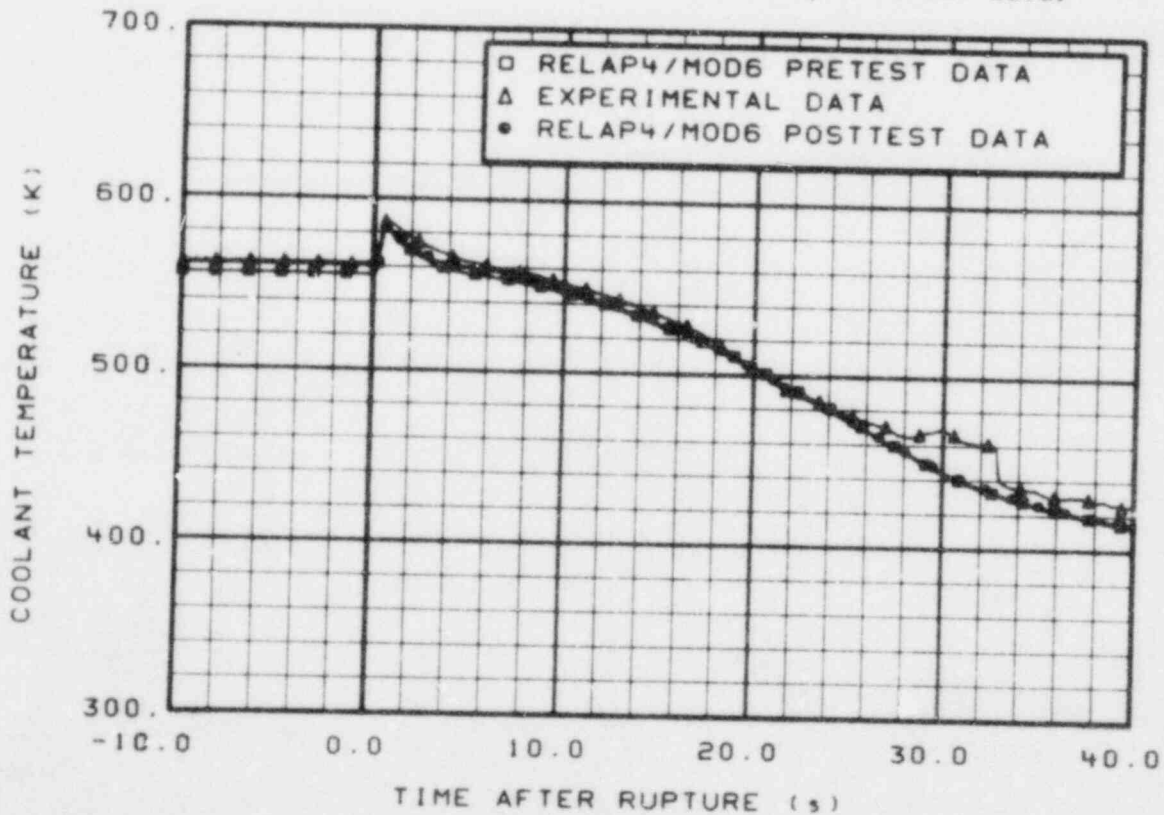


Figure A-74. Comparison of coolant temperature in fuel Module 2 lower end box for prediction, posttest, and experimental data.

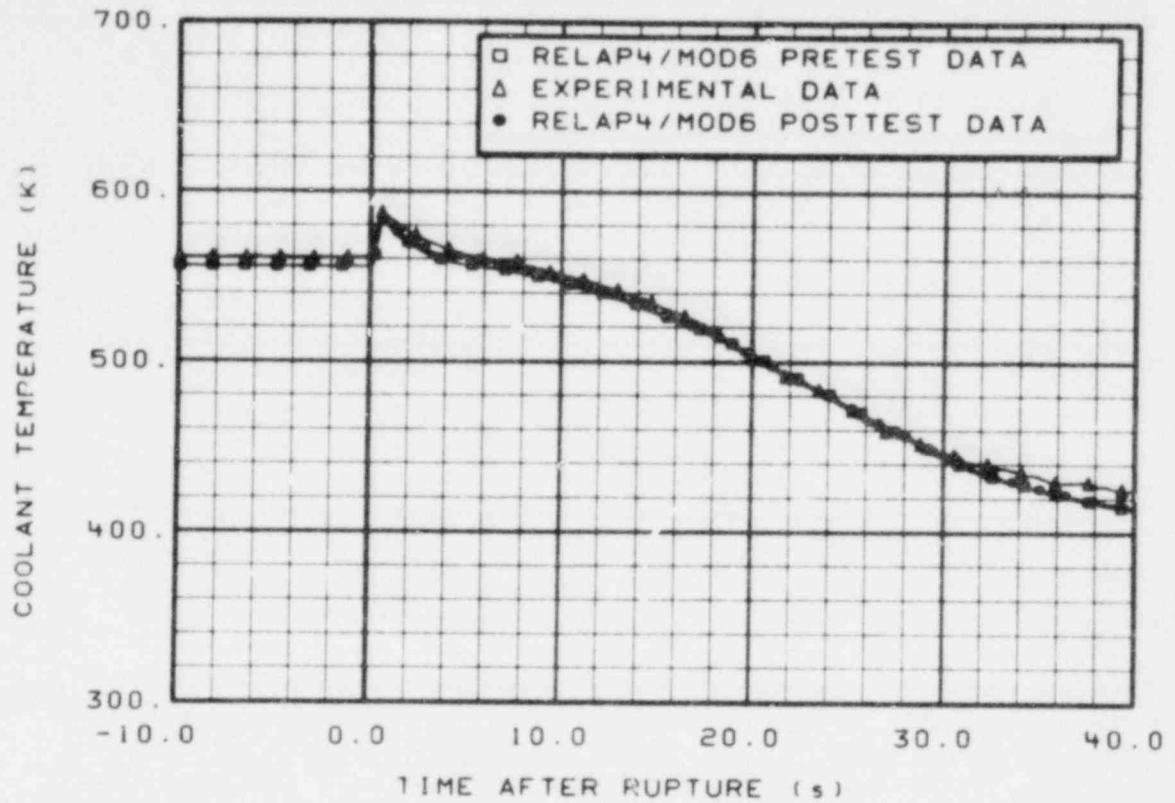


Figure A-75. Comparison of coolant temperature in fuel Module 3 lower end box for prediction, posttest, and experimental data.

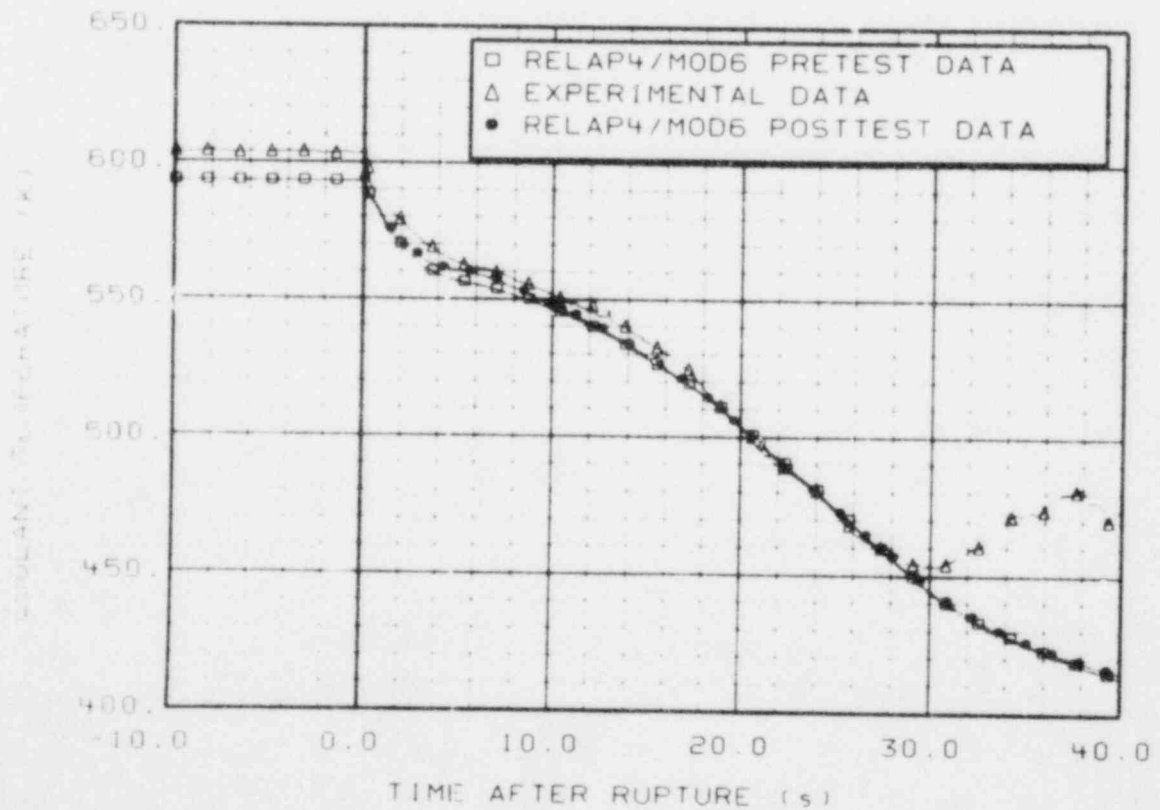


Figure A-76. Comparison of coolant temperature in fuel Module 1 upper end box for prediction, posttest, and experimental data.

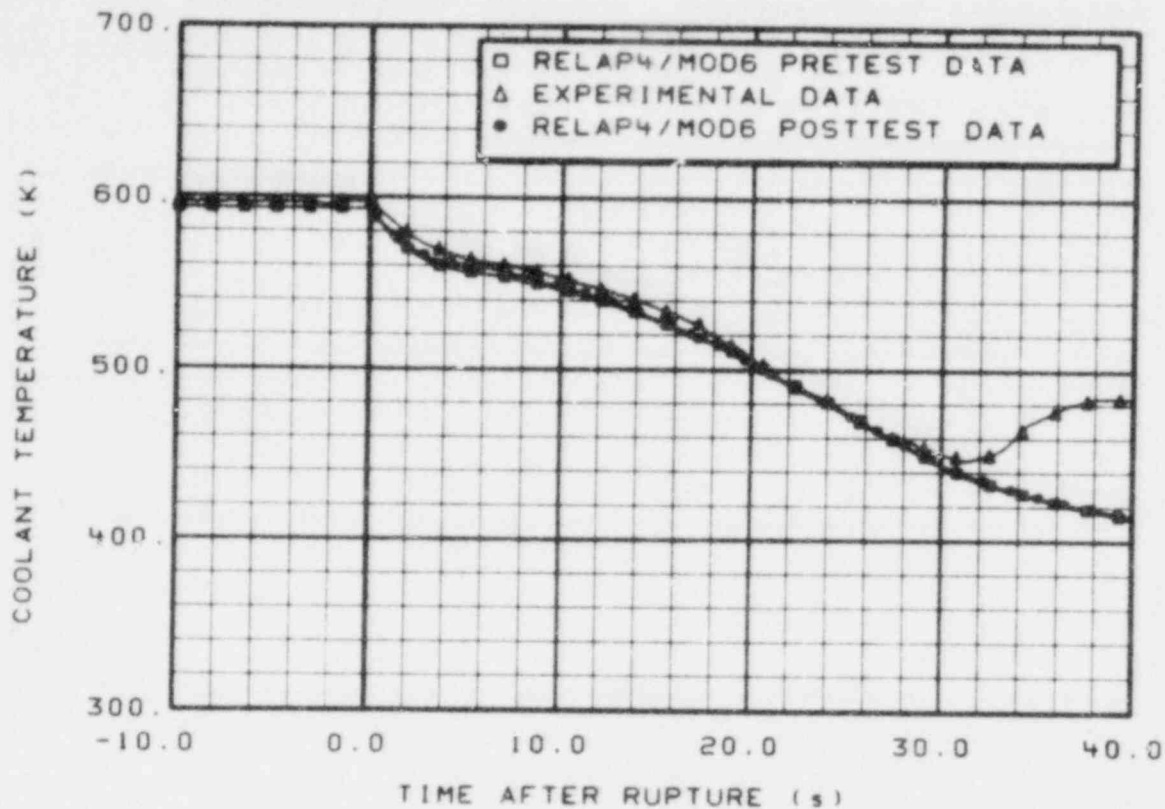


Figure A-77. Comparison of coolant temperature in fuel Module 1 upper end box at drag disc-turbine transducer for prediction, posttest, and experimental data.

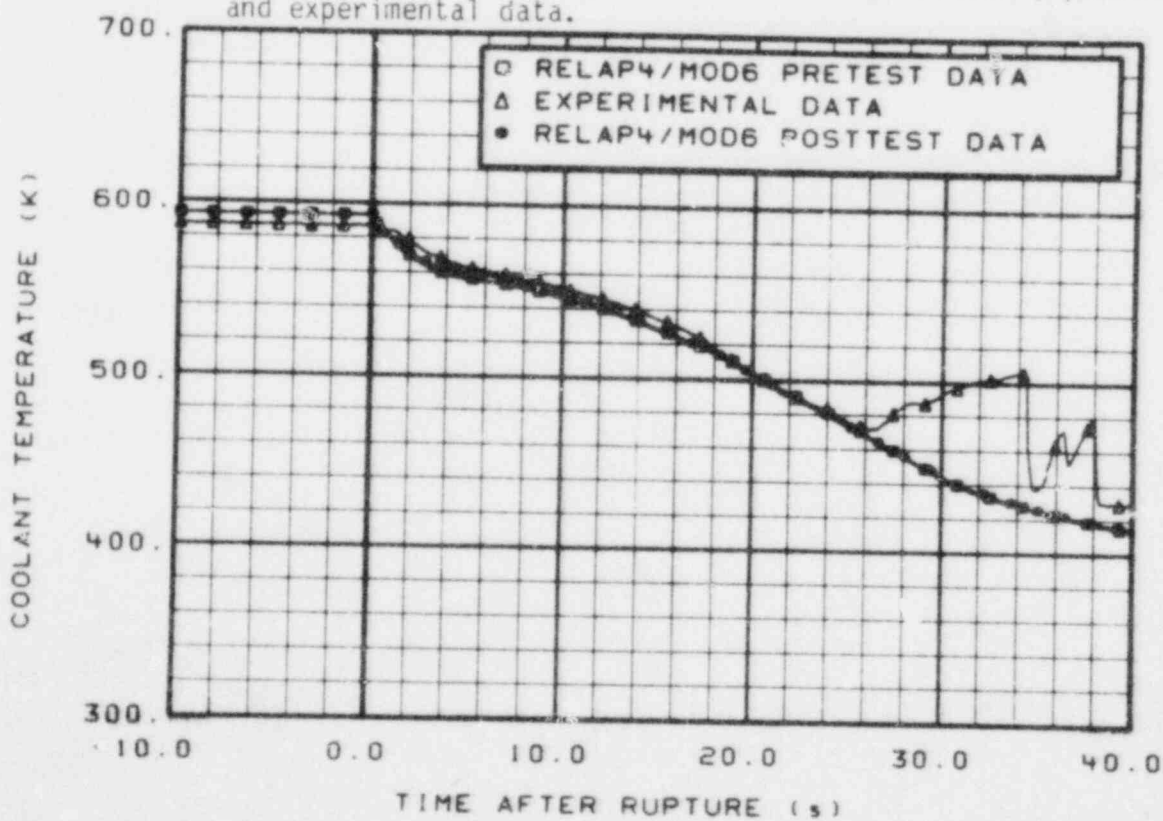


Figure A-78. Comparison of coolant temperature in fuel Module 2 upper end box for prediction, posttest, and experimental data.

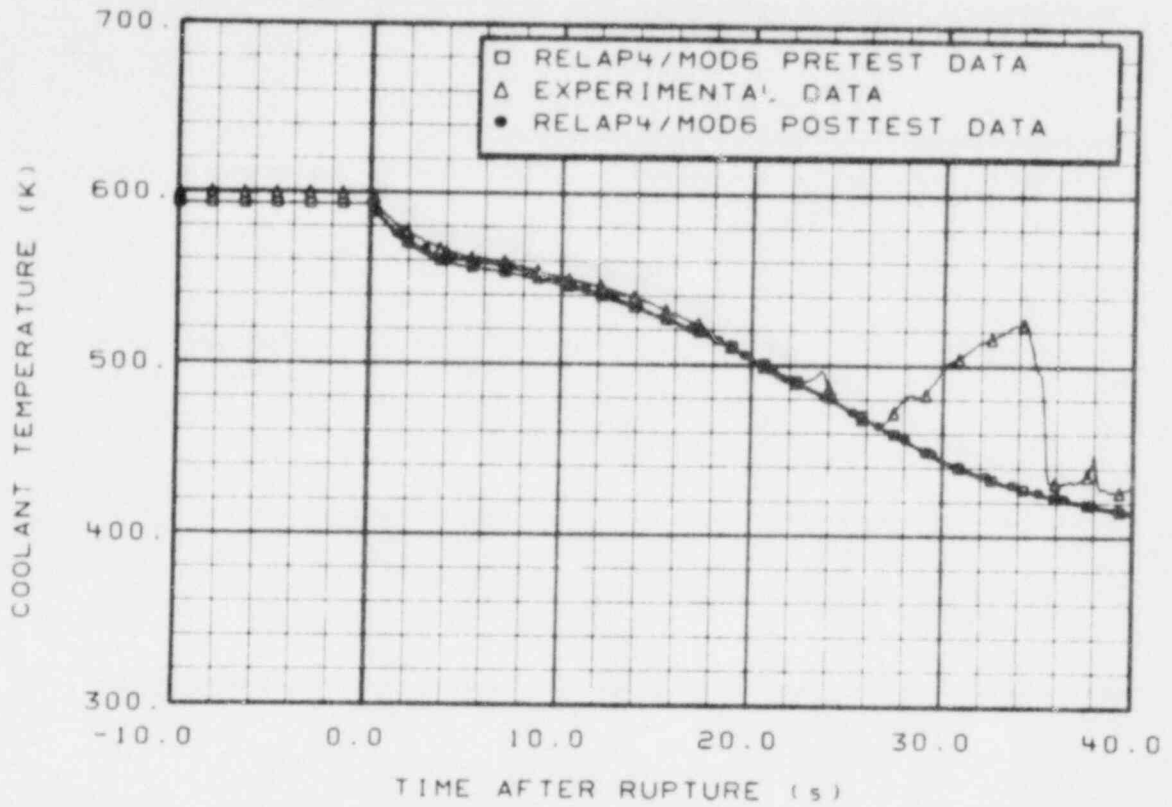


Figure A-79. Comparison of coolant temperature in fuel Module 3 upper end box for prediction, posttest, and experimental data.

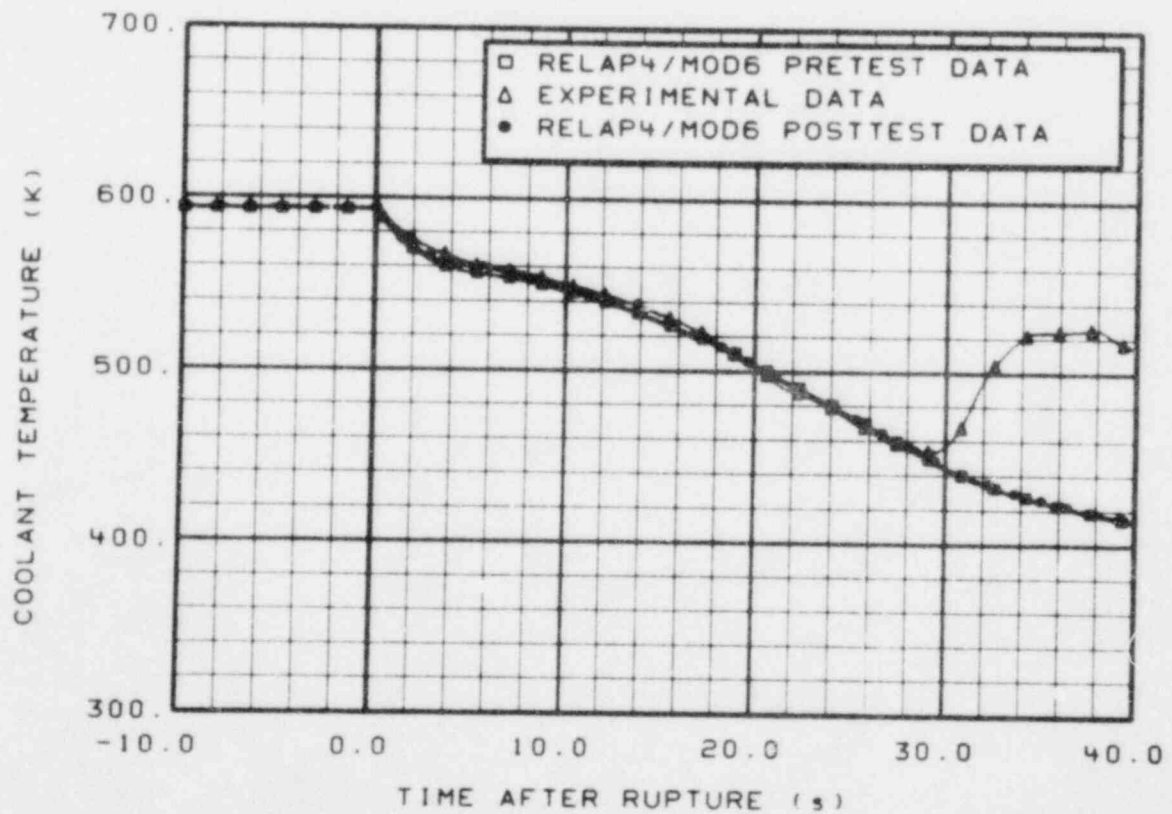


Figure A-80. Comparison of coolant temperature in fuel Module 3 upper end box at drag disc-turbine transducer for prediction, posttest, and experimental data.

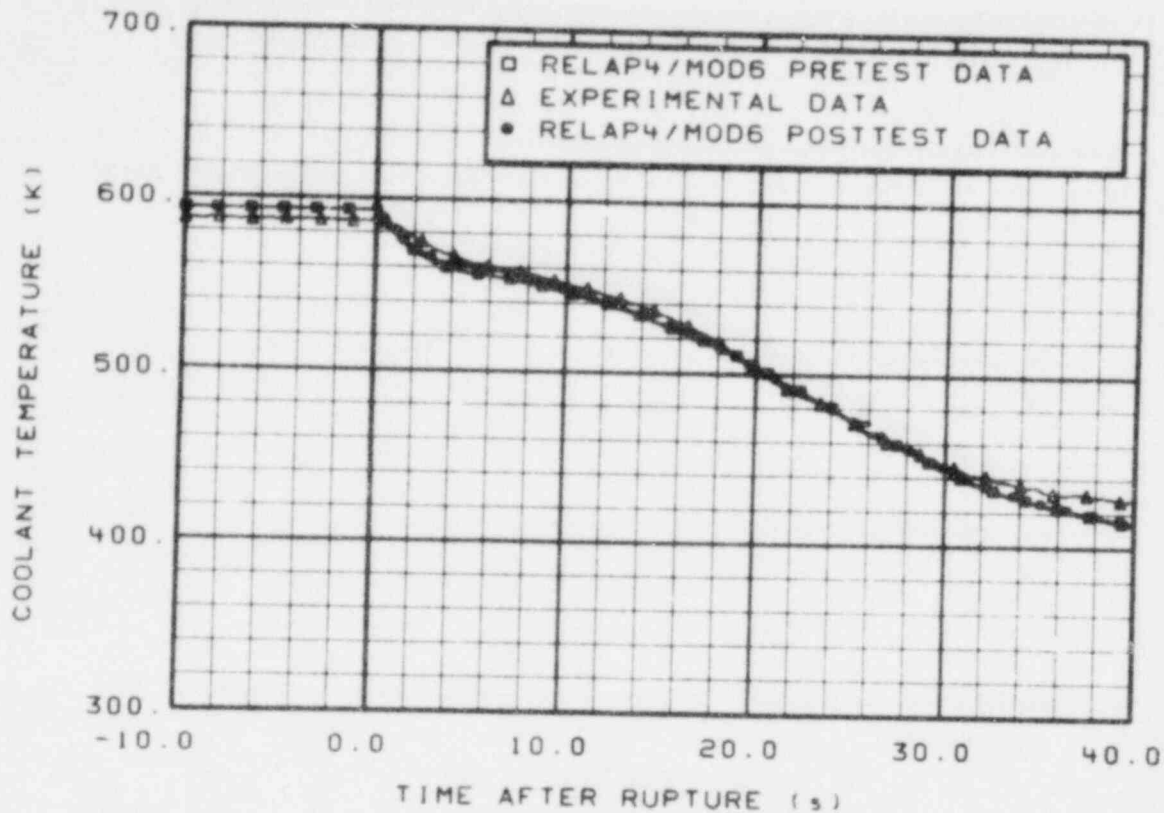


Figure A-81. Comparison of coolant temperature in fuel Module 4 upper end box for prediction, posttest, and experimental data.

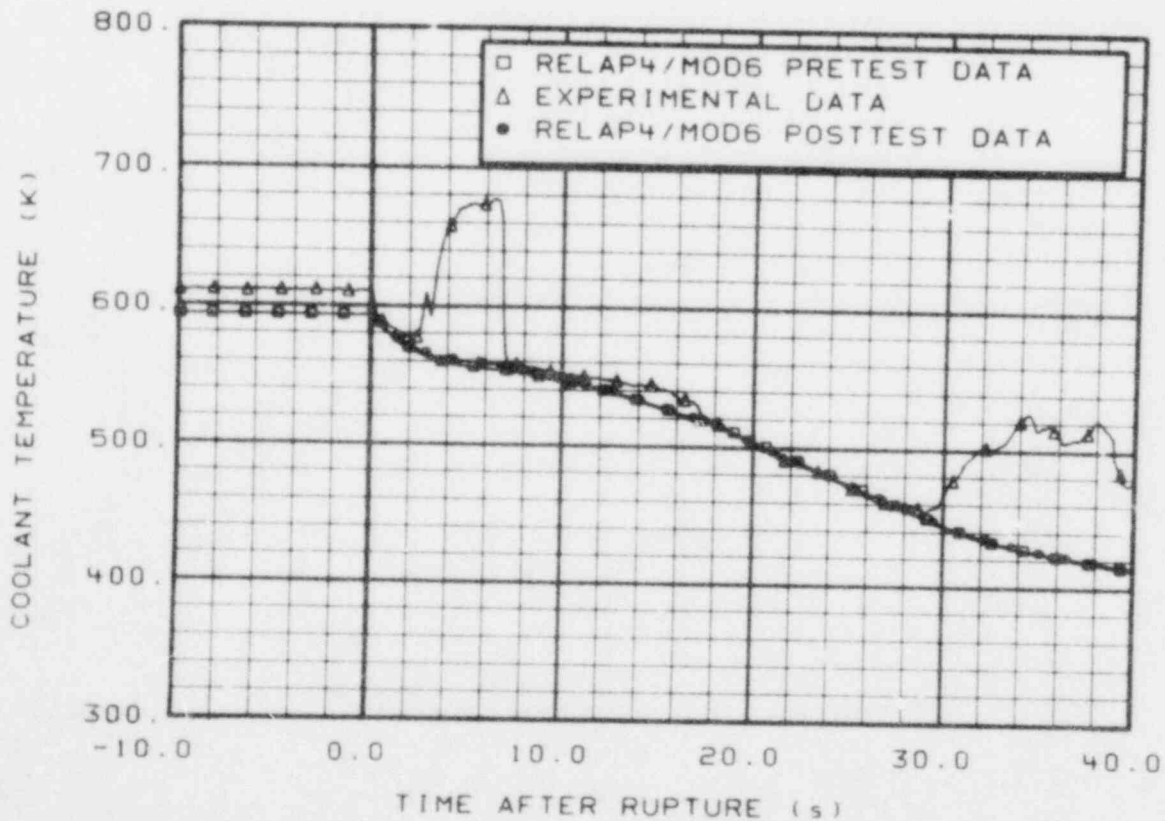


Figure A-82. Comparison of coolant temperature in fuel Module 5 upper end box for prediction, posttest, and experimental data.

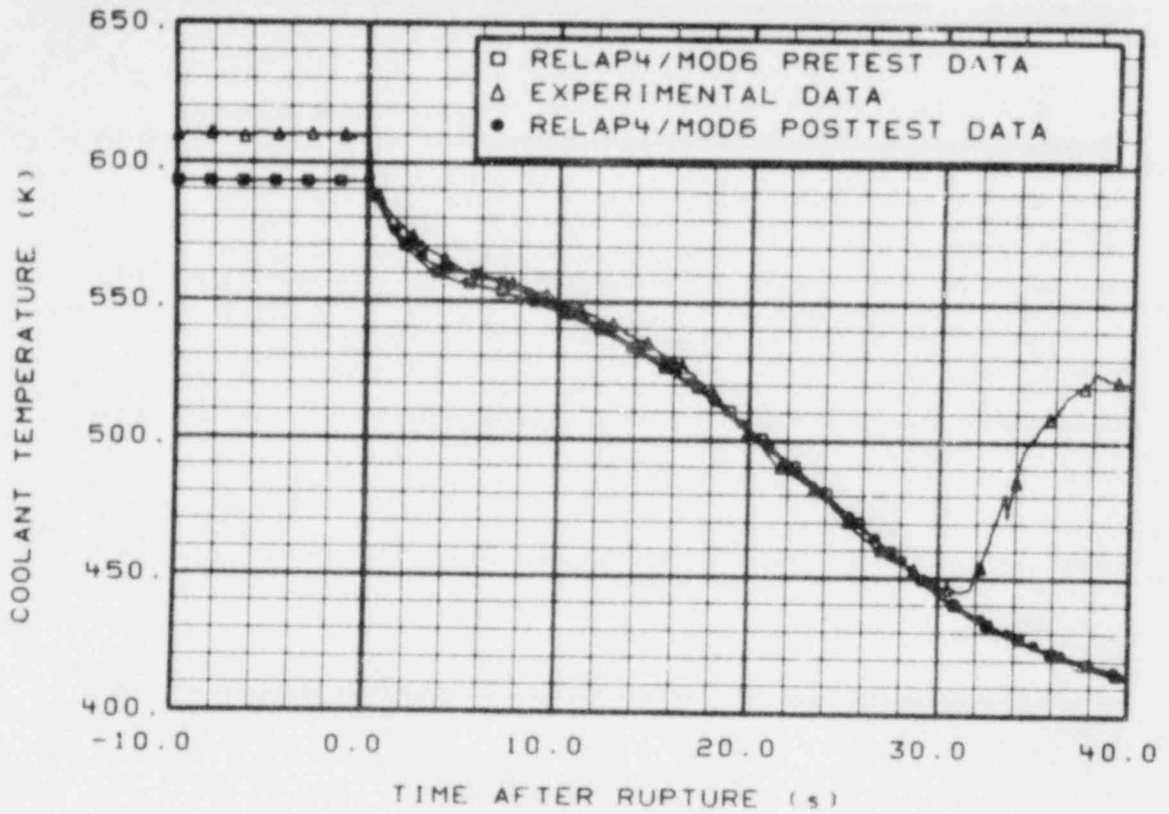


Figure A-83. Comparison of coolant temperature in fuel Module 5 upper end box at drag disc-turbine transducer for prediction, posttest, and experimental data.

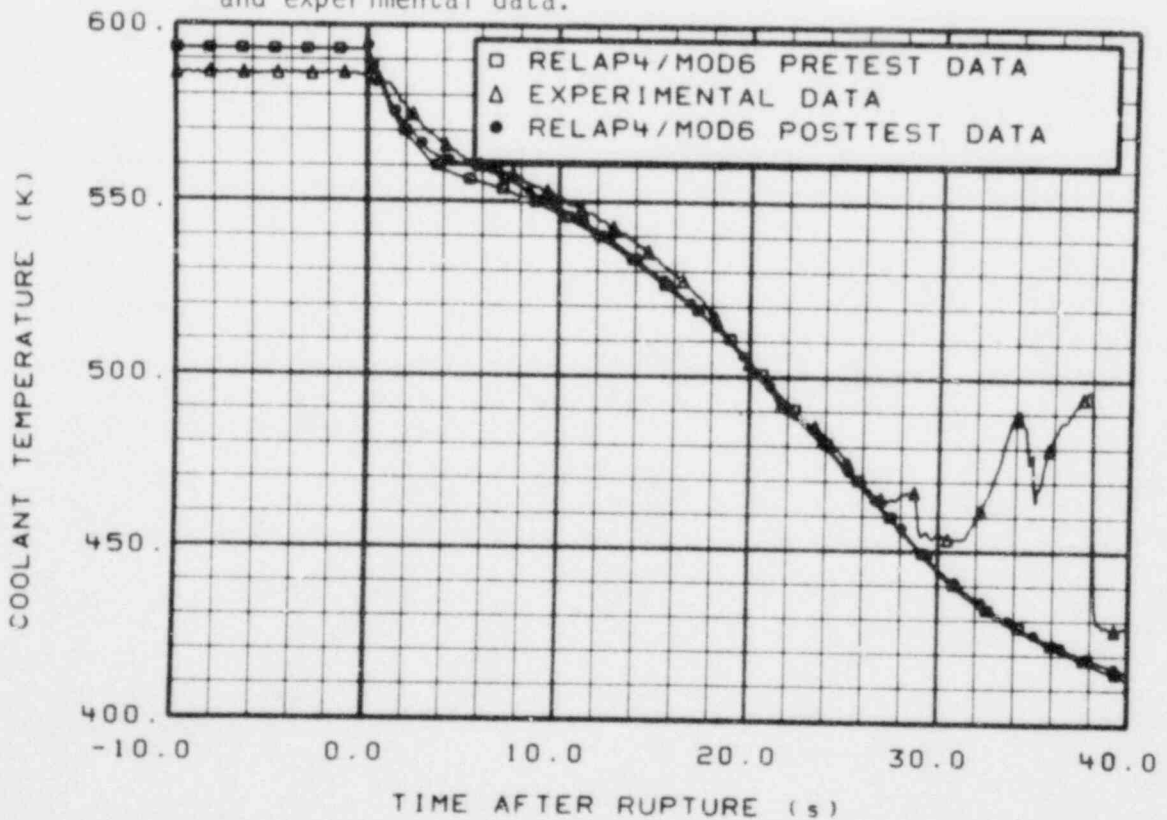


Figure A-84. Comparison of coolant temperature in fuel Module 6 upper end box for prediction, posttest, and experimental data.

APPENDIX B

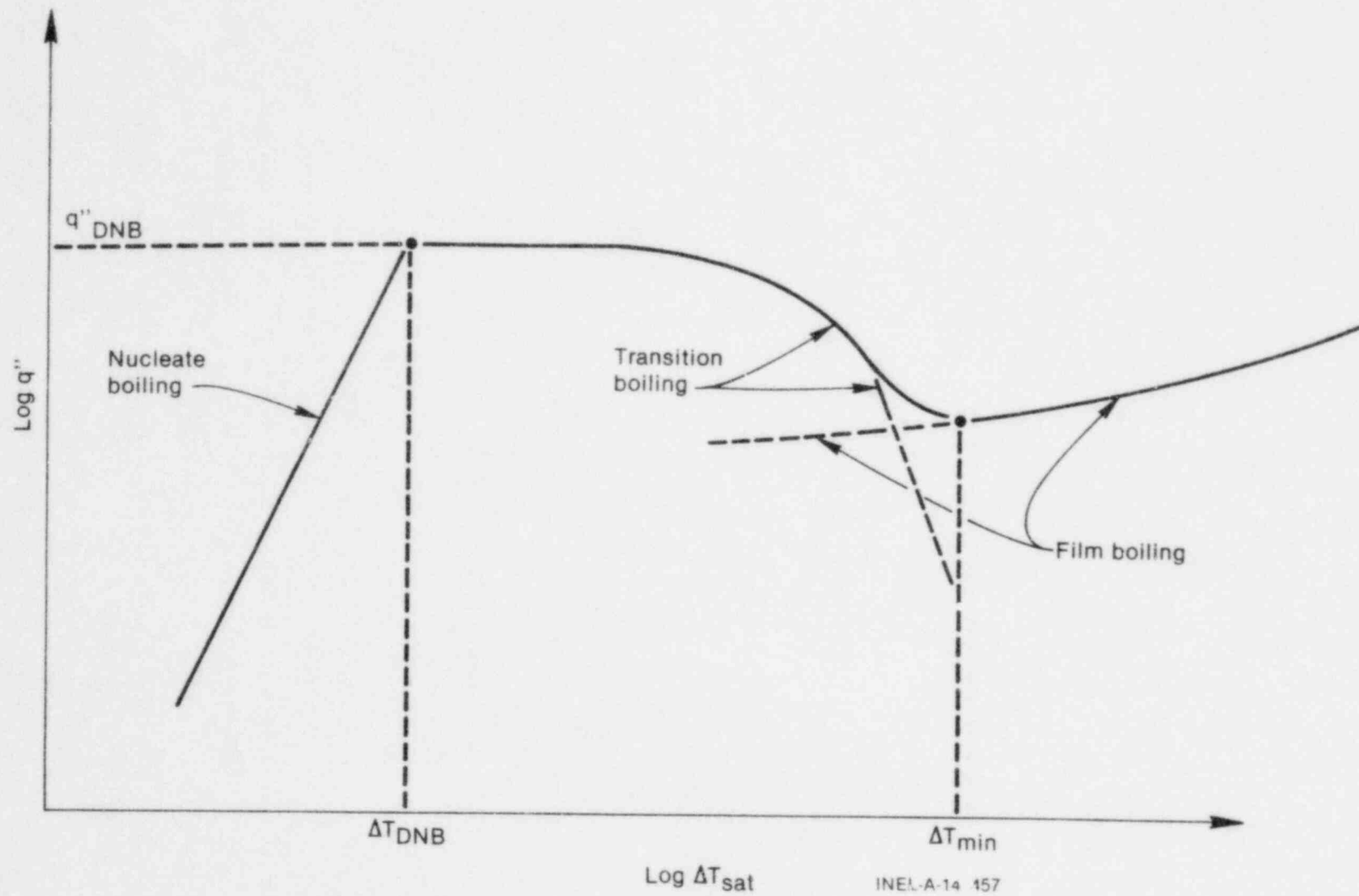
RELAP4/MOD6 HEAT TRANSFER SURFACE

APPENDIX B

RELAP4/MOD6 HEAT TRANSFER SURFACE

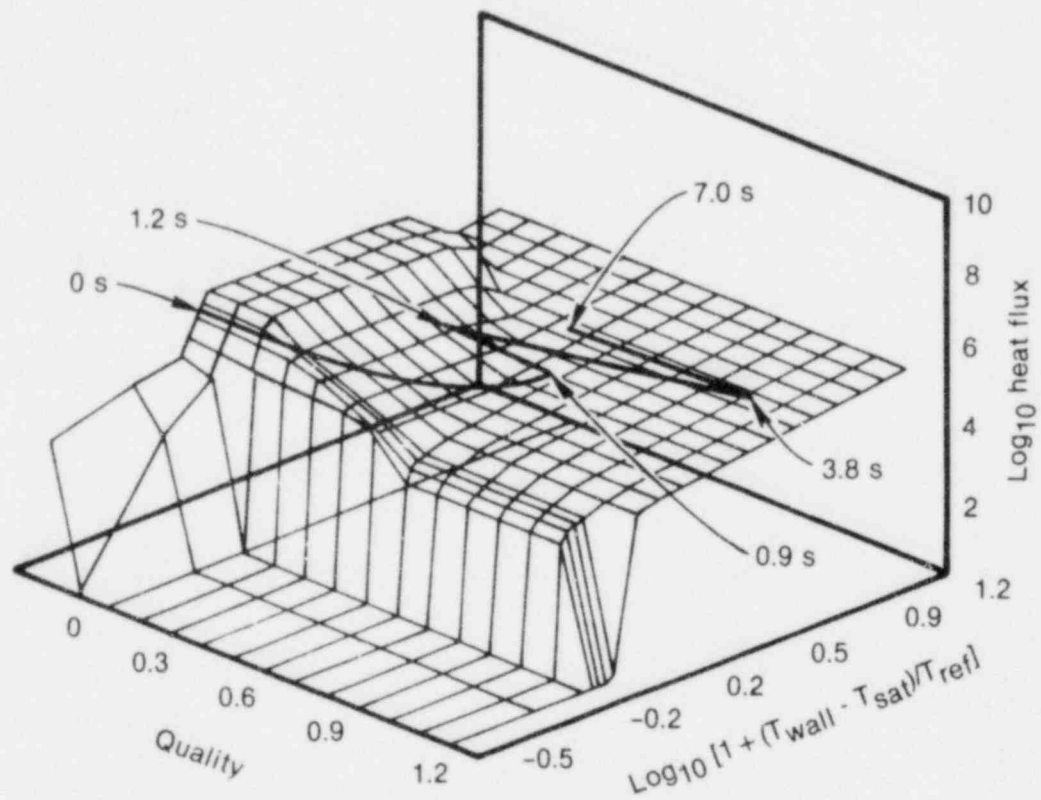
An essential element of calculating rewet behavior using RELAP4/MOD6 is in the proper prediction of post-critical heat flux (CHF) heat transfer as reflected in the calculated boiling curve. The RELAP4/MOD6 post-CHF portion of the boiling curve is constructed by summing the transition and the film boiling correlations, as shown in Figure B-1. Although a minimum wall superheat, ΔT_{\min} , can be calculated, it is not generally. For a given pressure, mass flux, and equivalent diameter, a family of boiling curves is obtained by varying the quality parameter of the post-CHF heat transfer correlation in RELAP4/MOD6 generating a heat transfer surface, as shown in Figure B-2. The locus represents the instantaneous fuel rod surface condition. The trajectory of the loci shows the fuel rod surface condition during the transient.

The failure of RELAP4/MOD6 to predict rewet can now be explained. Since the RELAP4/MOD6 post-CHF heat transfer correlation is related to the heat flux at the CHF point, different CHF correlations will result in different boiling curves as shown in Figure B-3. For medium mass flow rates, the Biasi CHF correlation will calculate higher q''_{CHF} than will the Hsu-Buckner CHF correlation and the ΔT_{\min} calculated by the code will be larger for the Biasi CHF correlation than for the Hsu-Buckner CHF correlation. For example, at the same ΔT_w , the Biasi CHF correlation will reduce the rod surface temperature below rewet temperature, while the rod surface temperature calculated by the Hsu-Buckner CHF correlation will still be above the rewet temperature. This does not mean that an arbitrary CHF correlation can be used. The CHF correlation should cover a large range of test parameters, and the ΔT_{\min} calculated by RELAP4/MOD6 should compare with the experimental data.



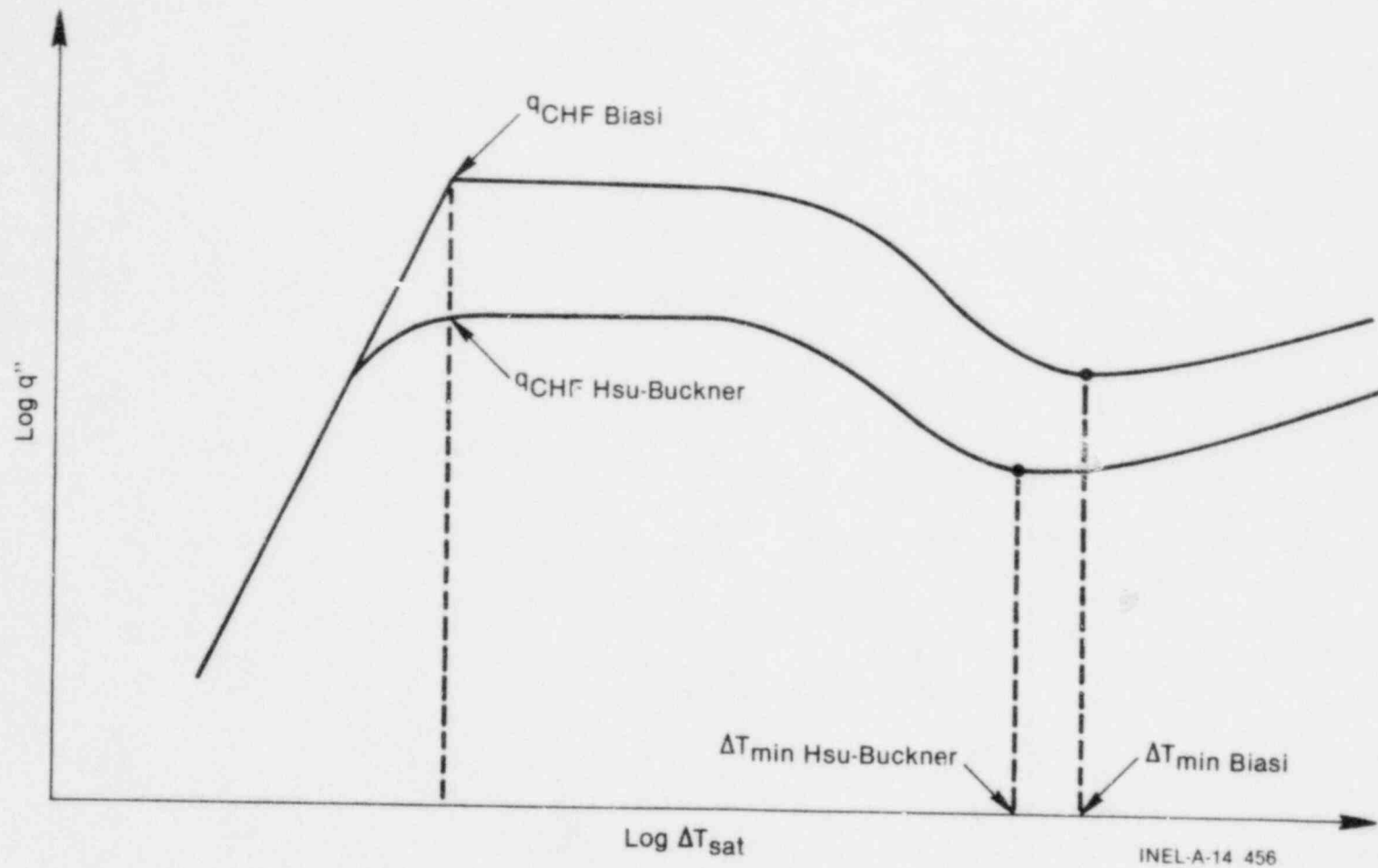
INEL-A-14 157

Figure B-1. RELAP4/MOD6 boiling curve.



INEL-A-14 450

Figure B-2. RELAP4/MOD6 blowdown heat transfer surface.



INEL-A-14 456

Figure B-3. Effects of the Biasi critical heat flux correlation on the RELAP4/MOD6 boiling curve

As mentioned in Section 3 of the text, the use of the boiling curve in RELAP4/MOD6 has two variables which can be adjusted to cause fuel rod rewet. The first variable is the CHF, which is discussed in the preceding paragraphs, and the second is ΔT_{\min} . To use the second variable, the manner of generating the boiling curves in RELAP4/MOD6 should be revised in a manner similar to that used in TRAC-P1A^{B-1}. Figure B-4 represents a typical TRAC-P1A boiling curve. The post-CHF region is generated by using the nucleate boiling and the CHF correlations to define q_{DNB} and ΔT_{DNB} . Next, ΔT_{\min} and the film boiling correlation are generated through use of the minimum wall superheat correlation and evaluated at ΔT_{\min} to yield q_{\min} . These two points are then interpolated, with respect to wall superheat, linearly on a log-log basis to produce the transition boiling portion of the boiling curve.

If the temperature at which the rewet should be predicted is now denoted as $\Delta T_{\text{L2-3 rewet}}$, its relative position on the boiling curve is as shown in Figure B-5. If the ΔT_{\min} calculated by RELAP4/MOD6 is less than $\Delta T_{\text{L2-3 rewet}}$, the code will not predict rewet. The second option is to change the ΔT_{\min} such that ΔT_{\min} is larger than $\Delta T_{\text{L2-3 rewet}}$; therefore, transition boiling is introduced instead of film boiling and a rewet is calculated. Using TRAC-P1A for example, the ΔT_{\min} was defined by the Henry correlation^{B-2} and is less than $\Delta T_{\text{L2-3 rewet}}$ as shown in Figure B-5. For this reason, the TRAC-P1A calculation does not predict rewet. However, TRAC-P1A + Iloeje, which used the Iloeje ΔT_{\min} correlation, calculated ΔT_{\min} Iloeje as greater than the $\Delta T_{\text{L2-3 rewet}}$. Therefore, TRAC-P1A + Iloeje predicted rewet.

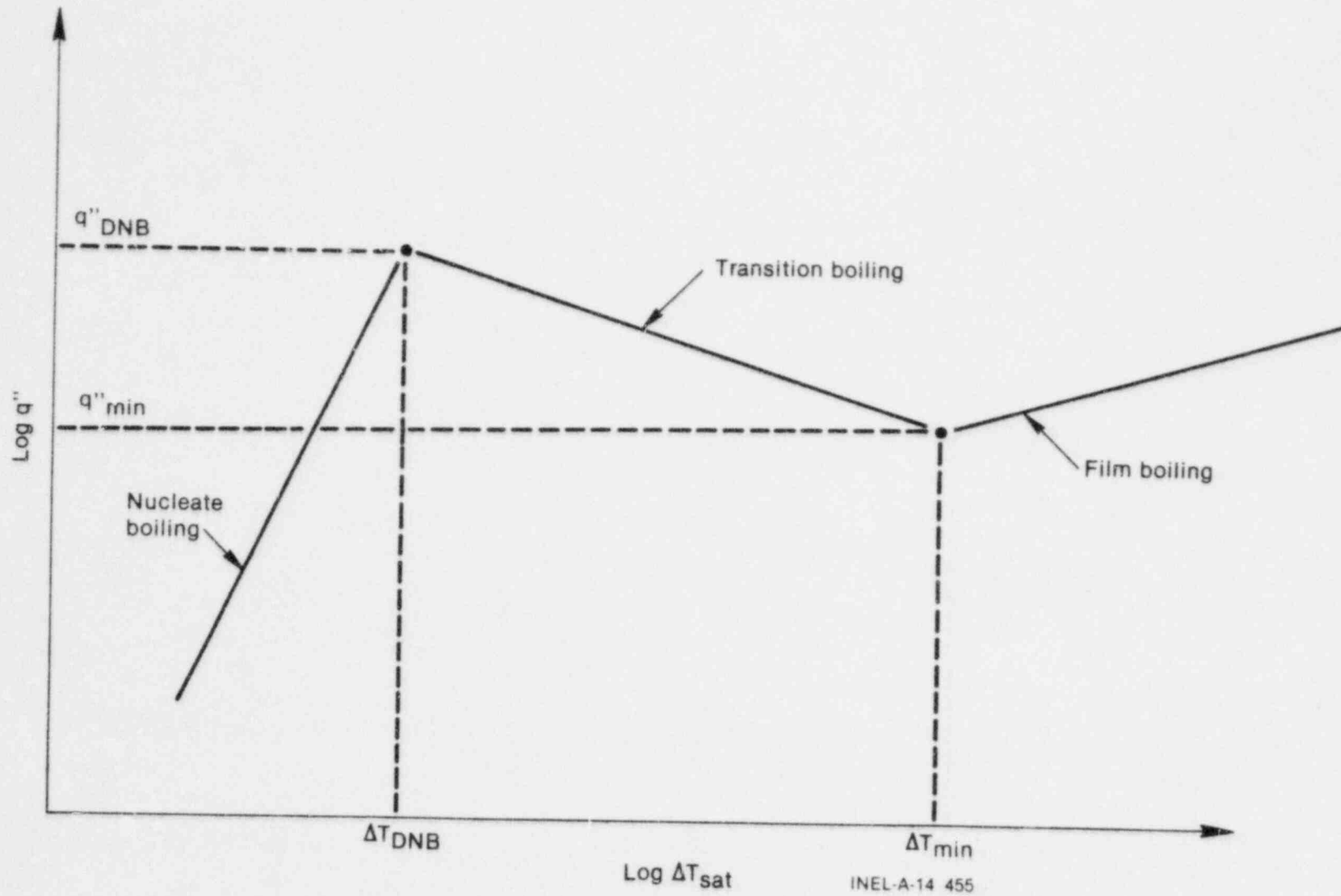


Figure B-4. TRAC-P1A boiling curve.

REFERENCES

- B-1. Los Alamos Scientific Laboratory, TRAC-P1A: An Advanced Best Estimate Computing Program for PWR LOCA Analysis, Vol. I, NUREG/CR-0665, LA-7777-MS, April 1979.
- B-2. R. E. Henry, "A Correlation for the Minimum Film Boiling Temperature," AICHE Symposium Series 138, 1974, pp. 81-90.